

**QUANTIZED VORTEX STATES
AND DYNAMICS IN
BOSE-EINSTEIN CONDENSATES**

HANQUAN WANG

*(B. Sc., Central China Normal University,
M. Sc., Beijing Institute of Technology)*

**A THESIS SUBMITTED
FOR THE DEGREE OF DOCTOR OF PHILOSOPHY
DEPARTMENT OF MATHEMATICS
NATIONAL UNIVERSITY OF SINGAPORE
2006**

Acknowledgments

I would like to thank my supervisor, Associate Professor Weizhu Bao, who gave me the opportunity to work on such an interesting research project, paid patient guidance to me, and provided me so much invaluable help and constructive suggestion on this thesis.

I am gratefully for the financial support from the National University of Singapore. Without the scholarship provided for me, I would not be able to start and finish the Ph.D study in Singapore.

It is also my pleasure to express my appreciation to Dr. Qiang Zhang, Dr. Xianguai Li, and Professor Qiang Du for their inspiring ideas.

My sincere thanks also go to my department staff, department classmates and friends in Singapore for their friendship and so much kind help.

I would also like to dedicate this work to my wife, my mother, my brother and my wife's parents, for their unconditional love and support for my work.

Hanquan Wang

March 2006

Notation

\mathbb{R}^d	real space in d-dimensions (d=1,2,3)
\mathbf{x}	Cartesian coordinate in \mathbb{R}^d
$\psi(\mathbf{x}, t)$	complex-valued wave function
\hbar	Planck constant
$\ \psi(\mathbf{x}, t)\ $	L^2 norm of the wave function $\psi(\mathbf{x}, t)$
$L_z = i\hbar(y\partial_x - x\partial_y)$	z-component of the angular momentum
Ω	angular velocity
μ	chemical potential
\bar{f}	conjugate of a complex function f
$V_d(\mathbf{x})$	trapping potential in d-dimensions
$N(\psi) = \int_{\mathbb{R}^d} \psi(\mathbf{x}, t) ^2 d\mathbf{x}$	normalization of the wave function $\psi(\mathbf{x}, t)$
$E(\psi)$	energy functional
$\delta_\alpha(t) = \int_{\mathbb{R}^d} \alpha^2 \psi(\mathbf{x}, t) ^2 d\mathbf{x}$	condensate width in the α -direction
∇	gradient operator

Contents

Acknowledgments	ii
Notation	iii
Summary	viii
1 Introduction	1
1.1 Brief history of Bose-Einstein condensation	1
1.2 Quantized vortex states in BEC	3
1.3 Review on numerical methods for stationary states	5
1.4 Review on numerical methods for the time-dependent GPE	6
1.5 Scope of this thesis	8
2 Stationary states for rotating Bose-Einstein condensate	10
2.1 GPE in a rotational frame	11
2.1.1 Dimensionless GPE	12
2.1.2 Reduction to two dimensions	13
2.2 Stationary states	14
2.2.1 Semiclassical scaling and geometrical optics	15
2.2.2 Ground state	16

2.2.3	Approximate ground state	20
2.2.4	Excited states	21
2.2.5	Critical angular velocity in symmetric trap	25
2.3	Numerical methods for stationary states	26
2.3.1	Gradient flow with discrete normalization(GFDN)	26
2.3.2	Energy diminishing	27
2.3.3	Continuous normalized gradient flow (CNGF)	29
2.3.4	Fully numerical discretization	31
2.4	Numerical results	32
2.4.1	Initial data for computing ground state	33
2.4.2	Results in 2D	35
2.4.3	Results in 3D	37
2.4.4	Critical angular velocity	38
2.4.5	Numerical verification for dimension reduction	38
2.4.6	Errors of the TF approximation	39
2.4.7	Spurious numerical ground states when $ \Omega \geq \gamma^{xy} = 1$	41
2.5	Conclusion	42
3	Dynamics of rotating Bose-Einstein condensate	54
3.1	Some properties of the GPE	55
3.2	A TSSP method for the GPE	56
3.2.1	Time-splitting	57
3.2.2	Discretization in 2D	58
3.2.3	Discretization in 3D	60
3.2.4	Stability	62
3.3	Numerical results	63
3.3.1	Accuracy test	63
3.3.2	Dynamics of a vortex lattice in rotating BEC	66
3.3.3	Generation of giant vortex in rotating BEC	70
3.4	Conclusion	71

4	Applications to rotating two-component BEC	73
4.1	The time-dependent coupled GPEs	75
4.1.1	Dimensionless coupled GPEs	76
4.1.2	Reduction to two dimensions	76
4.1.3	Semiclassical scaling	77
4.2	Stationary states	78
4.2.1	Ground state	78
4.2.2	Symmetric and central vortex states	79
4.2.3	Numerical methods for stationary states	80
4.2.4	Numerical results for the stationary states	81
4.3	Dynamics of rotating two-component BEC	88
4.3.1	Some properties of the coupled GPEs	88
4.3.2	A TSSP method for the coupled GPEs	89
4.3.3	Numerical results for the dynamics	92
4.4	Conclusion	99
5	Applications to dynamics of spinor $F=1$ BEC	102
5.1	The generalized Gross-Pitaevskii equations	104
5.1.1	Dimensionless formulation	105
5.1.2	Reduction to lower dimensions	105
5.2	Some properties of the generalized GPEs	106
5.3	A TSSP method for the generalized GPEs	107
5.3.1	Time-splitting	108
5.3.2	Discretization in 2D	110
5.3.3	Stability	111
5.4	Numerical results	111
5.4.1	Accuracy tests	111
5.4.2	Generation of vortices	114
5.4.3	Dynamics of a vortex lattice	116
5.5	Conclusion	118

6 Concluding remarks and future work	124
Bibliography	128
Publications	143

Summary

Quantized vortex states have been recently observed in a rotating Bose-Einstein condensate (BEC), in a rotating two-component BEC and in a spinor $F=1$ BEC at an extremely low temperature by several experimental groups. Stationary quantized vortex states and their dynamical behavior have become the focuses of both experimental and theoretical BEC research.

Theoretical studies of quantized vortex states in the BEC experiments have been made in the framework of the mean field approach. Based on the mean field theory, the rotating one-component BEC is described by a single Gross-Pitaevskii equation (GPE) in a rotating frame. The rotating two-component BEC and the rotating spinor $F=1$ BEC are described by a coupled Gross-Pitaevskii equations (GPEs) and a generalized GPEs respectively.

In this thesis, by means of efficient and accurate numerical methods to obtain both stationary solutions and time-dependent solutions of the single GPE, coupled GPEs and generalized GPEs, we numerically study the stationary quantized vortex states, as well as their dynamics in the rotating one-component BEC, two-component BECs and spinor BEC at zero temperature.

We first study stationary states such as ground, symmetric and central vortex

states as well as their energy diagrams, in the rotating BEC analytically and numerically. We start from the three-dimensional GPE with an angular momentum rotation term, scale it to obtain a four-parameter model, reduce it to a two-dimensional GPE in the limiting regime of strong anisotropic confinement and present its semiclassical scaling and geometrical optics. We discuss existence/nonexistence problems for ground states (depending on the angular velocity). We perform extensive numerical experiments to calculate these states using a gradient flow with discrete normalization (GFDN) with a backward Euler finite difference discretization. A mathematical proof of the effectiveness of the method is also given.

We next propose a new time-splitting spectral (TSSP) method for the GPE in a rotating frame and study the dynamics of rotating one-component BEC at a very low temperature. This new numerical method is explicit, unconditionally stable, time reversible, time transverse invariant, and of spectral accuracy in space and second-order accuracy in time. Moreover, it conserves the position density in the discretized level. Numerical applications on studying the vortex lattice dynamics and the generation of giant vortex for the rotating one-component BEC are presented.

We then extend the GFDN method to search numerically ground state, symmetric state and central vortex state as well as their energy diagrams, aiming to investigate various equilibrium properties of vortex states in the rotating two-component BEC with a relevant experimental setup. Moreover, we propose a new TSSP method to solve the time-dependent coupled GPEs with a coupling term which describe the dynamics of rotating two-component BEC. Some analytical results for the coupled GPEs are presented and they are confirmed numerically by directly solving the coupled GPEs with our TSSP method. We apply the TSSP method to study the generation of topological modes such as single vortex, double vortices, dipoles and quadrpoles. The vortex lattice dynamics in the rotating two-component BEC are also studied numerically.

Finally, we propose a new TSSP method for the generalized GPEs and for computing the dynamics of spinor $F=1$ BEC at a very low temperature. We show that

numerical results agree with those of the analytical properties of the generalized GPEs. We apply the method to study the dynamic generation of vortices in the spinor $F=1$ BEC within the Ioffe-Pritchard magnetic field, and to investigate the effect of this magnetic field on the vortex lattice dynamics.

Introduction

1.1 Brief history of Bose-Einstein condensation

The basic idea of Bose-Einstein condensation was introduced in 1925 when Albert Einstein, on the basis of a paper by the Indian physicist Satyendra Nath Bose (1924), devoted to the statistical description of the quanta of light, predicted that a phase transition in a gas of noninteracting atoms could occur as a result of quantum statistical effects. In that phase transition period, a macroscopic number of noninteracting bosons will spontaneously occupy the single quantum state of the lowest energy, forming a BEC [62].

For a long time these predictions had no practical impact. Immediately after the discovery of superfluidity in liquid helium in 1938, F. London explained that the superfluidity could be a manifestation of Bose-Einstein condensation. However later experimental studies on superfluid helium in 1955 measured only a fraction of condensate inside. The experimental studies on the dilute atomic gases were developed much later, starting from 1970s. The first studies were focused on spin-polarized hydrogen, that was considered, because of its light mass, as the most natural candidate for realizing Bose-Einstein condensation. In a series of experiments, it came very close to forming a BEC, but it did not form a pure BEC [104].

Thanks to the development of laser-based cooling techniques and magneto-optical

trapping in 1980s, Einstein's predictions were finally proved in 1995 when the experimental teams of Cornell and Wieman at Boulder of JILA and of Ketterle at MIT succeeded in reaching the ultra low temperature and the densities required to observe BEC in vapours of ^{87}Rb [7] and ^{23}Na [40]. In the same year, first signatures of occurrence of Bose-Einstein condensation in vapors of ^7Li were also reported [23]. It was considered as such an important development that the centennial Nobel Prize for Physics has been awarded to the first three researchers who created this so-called fifth state of matter in the laboratory. Since its realization in the dilute bosonic atomic gases, Bose-Einstein condensation was later achieved in other atomic species, including the spin-polarized hydrogen, metastable ^4He and ^{41}K .

BEC has afforded an intriguing glimpse into the macroscopic quantum world and has stimulated intense theoretical activity. A rather massive amount of work has been done in the last couple of years, both to interpret the initial observations and to predict new phenomena. One of the fundamental questions asked of BEC in both theoretical and experimental work was whether it was also superfluid. A particularly interesting signature of superfluids are their ability to support quantized vortex states.

The first experimental creation of a vortex was made in 1999 at JILA by using a nearly spherical ^{87}Rb condensate containing two different hyperfine components [91]. Later, *École Normale Supérieure* group in Paris [32, 37, 87, 88] studied vortex creation in elongated rotating cigar-shaped condensate with one component. They observed small vortex arrays of up to 11 vortices (arranged in two concentric rings). Recently, an MIT group [1] has prepared considerably larger rotating condensates in less elongated trap, they have observed triangular vortex lattices with up to 130 vortices. More recently Leanhardt et al. [82] used "topological phase imprinting" to create a coreless vortex in a spinor $F=1$ BEC.

To understand the above various observations of quantized vortex states in BEC, as well as to study their significance as a fundamental type of coherent nonlinear excitations and as a crucial role in understanding superfluidity in BEC, the theoretical

investigation of quantized vortex states in BEC is of great importance [50, 77].

1.2 Quantized vortex states in BEC

The natural starting point for studying the behavior of BEC is the theory of weakly interacting bosons which takes the form of the Gross-Pitaevskii theory. This theory is a mean field approach for the order parameter associated with the condensate. It provides closed and relatively simple equations for describing the relevant phenomena associated with BEC, because it is assumed that the N particles of the gas are condensed in the same state. The theory is well suited to describing most of the effects of two-body interactions in the dilute gas at almost zero temperature and can be naturally generalized to explore thermal effects on the BEC [39, 41].

Quantized vortex states are topological defects of complex-valued order parameters in the Bose-Einstein condensation. Theoretical studies of quantized vortex states in the BEC have also been made in the framework of the mean field approach, which has provided a very good description on vortices in BEC (see a review for vortices in one-component BEC in [50], a recent review for vortices in multi-component BEC in [77]).

Since all the particles occupy the same state in the BEC, the condensate is characterized by one complex-valued wave function $\psi(\mathbf{x}, t)$. Writing $\psi(\mathbf{x}, t) = \sqrt{\rho(\mathbf{x}, t)} \exp(i\theta(\mathbf{x}, t))$, the square of the magnitude of the wave function, i.e., $\rho(\mathbf{x}, t) = |\psi(\mathbf{x}, t)|^2$ describes the particle density. The gradient of the phase $\theta(\mathbf{x}, t)$ gives the superfluidity velocity $\vec{v}(\mathbf{x}, t) = (\hbar/m)\nabla\theta(\mathbf{x}, t)$, where m is the mass of a particle and \hbar is the planck constant. A vortex is a singular point (in two dimensions) or line (in three dimensions) where the density of the wave function vanishes. Along a contour C encircling a vortex, if the circulation of the velocity is quantized in units of \hbar/m as $\int_C \vec{v} ds = \hbar/m \int_C \nabla\theta ds = n\hbar/m$ ($n = 0, \pm 1, \pm 2, \dots$), then it is called a “quantized vortex”.

As mentioned before, quantized vortex states appear in the experiments of rotating one-component BEC, rotating two-component BEC and spinor F=1 BEC. We are going to present a numerical study on these stationary vortex states and their dynamical behavior after formation based on the mean field theory. According to the theory, the rotating one-component condensate can be described by a complex wave function $\psi(\mathbf{x}, t)$, which is governed by a single GPE in a rotating frame [4, 13, 25, 50, 54, 55]; the rotating two-component condensates are described by two wave functions $\psi_1(\mathbf{x}, t)$ and $\psi_2(\mathbf{x}, t)$, which are governed by the coupled GPEs with a coupling constant [58, 59, 77, 98, 117]; and the rotating spinor F=1 BEC can be described by wave functions $\psi_1(\mathbf{x}, t), \psi_0(\mathbf{x}, t), \psi_{-1}(\mathbf{x}, t)$ with refer to the F=1 hyperfine spin states $m_F = 1, 0, -1$. These wave functions, $\psi_1(\mathbf{x}, t), \psi_0(\mathbf{x}, t), \psi_{-1}(\mathbf{x}, t)$, are governed by the generalized GPEs [65, 66, 79, 89, 94, 101, 136, 137]. The equilibrium properties or the stationary vortex states of the rotating one-component BEC, two-component BEC and spinor BEC can be described by the stationary solutions of the single GPE in a rotating frame, the coupled GPEs and the generalized GPEs respectively. The dynamics of rotating one-component BEC, two-component BEC and spinor BEC are governed by the single GPE, coupled GPEs and the generalized GPEs respectively. Since these GPEs are nonlinear partial differential equations and their analytical solutions are not available, we are interested in seeking efficient and accurate numerical methods to obtain both stationary solutions and time-dependent solutions for the single GPE, couple GPEs and generalized GPEs.

There are a number of articles devoted to finding stationary solutions and time-dependent solutions of the single GPE. However, very few articles have studied numerical methods for finding stationary solutions and time-dependent solutions of the coupled GPEs or the generalized GPEs. This is perhaps due to the fact that coupled or generalized GPEs are relatively new equations in the BEC. Although these GPEs are more complicated than the single GPE, numerical methods for the single GPE can be extended to these GPEs if we design them in a proper way. In the next two sections, we mainly review numerical methods for stationary solutions

and time-dependent solutions of GPE.

1.3 Review on numerical methods for stationary states

There are several ways that can be used to find stationary states, or stationary solutions of the single GPE. The first way to find a stationary solution is to directly solve the time-independent GPE [34]. Although the method is straightforward and easy to implement, it has three main disadvantages: (i) it is too difficult and expensive to solve because the discretized equation is highly nonlinear, (ii) this equation is satisfied not only by ground state but also many excited states, and (iii) there is no mathematical justification yet for the existence of solutions of this problem. The second way to characterize a stationary solution is by studying the energy functional $E(\psi)$ and using the fact that each stationary solution is a critical point of $E(\psi)$ with constraints. Then one can use a minimization procedure to find the minimizer of $E(\psi)$ with constraints. There are mainly three approaches to directly minimize $E(\psi)$ with constraints in the literature.

1. One approach is to find the minimizer of $E(\psi)$ using a discrete basis such as Fourier basis or eigenfunctions of the harmonic oscillator [48, 49, 116] or finite element method [10]. This approach expands the unknown solutions using a discrete basis and defines a new functional over the finite dimensional space, which is then minimized in the finite dimensional domain. However, there is a problem on how to satisfy the constraints.
2. Another approach is to define a new free energy functional $F(\psi)$ that removes the constraints from $E(\psi)$. Several ways such as the method of Lagrange multiplier [4, 56, 57] or the method of Rayleigh functional [120] can define $F(\psi)$. The practical advantage of $F(\psi)$ is that we can perform a continuous descent over the whole domain without the constraints. However, this approach has a

problem on how to calculate the Lagrange multiplier correctly.

3. Still the other approach is to search the minimum of $E(\psi)$ by using a descent technique modified to account for the constraints, which is known as imaginary time evolution method in physics literature [25, 33, 51, 135]. This method is easy to understand and to implement since we need only integrate the time dependent equation in imaginary time followed by the normalized step.

We will use the imaginary time method to find the stationary solutions of the GPE. We first let $t \rightarrow it$ in the GPE (or coupled GPEs) and get a gradient flow. The gradient flow is integrated in time and followed by the normalized step to satisfy the constraints, the whole procedure is named as the gradient flow with discrete normalization (GFDN) [10]. We will also mathematically justify that the GFDN is a correct way to find stationary solutions of the single GPE and coupled GPEs.

1.4 Review on numerical methods for the time-dependent GPE

For the single GPE without a rotational term, most of previous authors solved the equation by using a low-order method, such as the finite difference method [28, 29, 102] or the finite element method [22] for the discretization of the spatial variables combined with conservative schemes for the discretization of the time variable. However, these low-order methods are difficult to implement in higher dimensions. Dion et al. [43] proposed a Galerkin spectral method for the GPE, which is a high-order method but difficult to apply for higher dimensional problems as well. Bao et al. [8, 9, 11, 14, 16, 17] have developed several time-splitting spectral methods for the single GPE without a rotating term, which were demonstrated that they are much better than the low-order finite difference methods [53, 73, 80, 93, 100]. These time-splitting spectral methods are very efficient and highly accurate since they are explicit, unconditionally stable, time reversible, time transverse invariant,

and of spectral accuracy in space.

For the time-dependent solutions of the single GPE in a rotating frame, due to the appearance of the angular momentum rotation term in the GPE, new numerical difficulties are introduced. Currently, the numerical methods used in the physics literature for studying dynamics of rotating BEC remain limited [74, 132], and they usually are low-order finite difference methods. For example, Adhikari et al. [2] proposed a time-splitting finite difference method for the equation in two dimensions. Wang [132] studied the method's numerical accuracy. Tsubota et al. [130] used the Alternating Direction Implicit finite difference method to solve the equation by adding a damped term in order to study the dynamic formation of vortex lattice in rotating BEC. Tian et al. [128] presented an explicit symplectic finite difference scheme for the equation and used it to study the vortex evolution.

Recently, some efficient and accurate numerical methods were designed for computing dynamics of rotating BEC. For example, Bao, Du and Zhang [19] proposed a numerical method for computing dynamics of rotating BEC by applying a time-splitting technique for decoupling the nonlinearity in the GPE and adopting the polar coordinates or cylindrical coordinates so as to make the coefficient of the angular momentum rotation term constant. The method is time reversible, unconditionally stable, implicit but can be solved very efficiently, and conserves the total density. It is of spectral accuracy in transverse direction, but usually of second- or fourth-order accuracy in radial direction. Another numerical method is the leap-frog spectral method used for studying vortex lattice dynamics in rotating BEC [140]. This method is explicit, time reversible, of spectral accuracy in space and second order accuracy in time. But it has a stability constraint for each time step.

We will design a time-splitting spectral method based on Fourier expansions, which enjoys advantages of the two numerical methods mentioned above, to solve the single GPE in a rotational frame. Our key idea is: by applying a time-splitting technique for decoupling the nonlinearity and properly using the alternating direction implicit technique for the angular momentum rotation term in the GPE, at

every time step, the GPE in the rotational frame is then decoupled into a nonlinear ordinary differential equation (ODE) and two partial differential equations with constant coefficients. This allows us to develop a new time-splitting spectral (TSSP) method for the single GPE in a rotational frame. We will also extend the TSSP method to solve both the coupled GPEs and the generalized GPEs.

1.5 Scope of this thesis

The first aim of our study is to apply the imaginary time method and present a GFDN for computing the stationary states of rotating BEC, i.e., the stationary solutions of the GPE. We prove its energy diminishing property and propose numerical methods to discretize the GFDN. Our proof gives a mathematical justification of the imaginary time method, which is widely used in the physics literature to compute the stationary states for the rotating BEC. Next we extend the GFDN and its discretization to find stationary solutions of the coupled GPEs, and show that it is numerically efficient and mathematically accurate. After obtaining stationary solutions of the single GPE and the coupled GPEs numerically, we numerically and theoretically obtain results for the stationary quantized vortex states of rotating one-component BEC and rotating two-component BEC.

The second aim of our study is to design a new high-order numerical scheme—TSSP method (based on Fourier expansion) to solve the time-dependent GPE. Through detailed numerical results, we show that (i) it is of spectral accuracy in space and second order accuracy in time, (ii) it keeps the conservation laws of the GPE in the discretized level, (iii) it is explicit and unconditional stable, and (iv) finally it can be extended to solve the time-dependent coupled GPEs and generalized GPEs and it can keep the conservation laws in these coupled and generalized GPEs numerically. After obtaining time-dependent solutions of the single GPE and the coupled or generalized GPEs numerically, we simulate the dynamics of quantized vortices in rotating BEC.

What we are mainly concerned with here are stationary vortex states and their dynamics in the rotating BEC at extremely low temperature, which can be modelled by the single GPE (or coupled or generalized GPEs). From the practical point of view, our numerical and theoretical results can shed light on some aspects of their equilibrium states and dynamics of the rotating BEC, which might not be available in the experiments because of high experiment cost. From the theoretical point of view, we can justify in some aspects the mean field theory for the correct description of BEC.

Stationary states for rotating Bose-Einstein condensate

We analytically and numerically study ground, symmetric and central vortex states, as well as their energy diagrams in BEC under a rotational frame representing a laser beam rotating with a given angular velocity in the magnetic trap. We extend the efficient and stable numerical method of GFDN with its backward Euler finite difference (BEFD) discretization, proposed in [8] for computing the ground state of a non-rotating BEC, to rotating BEC, and then apply it to study the ground state, symmetric state, central vortex states, central vortex ground state, as well as their energy diagrams, in rotating BEC numerically. Vortices and energy bifurcation are observed in the ground state when the angular rotation speed is bigger than a critical frequency. We also present some new analytical and numerical results for the ground, symmetric and central vortex states, as well as their energy diagrams in rotating BEC. These results include: (i) provide asymptotics of the energy and chemical potential of the ground state in the semiclassical regime; (ii) show that the ground state is a global minimizer of the energy functional over the unit sphere and all excited states are saddle points in the linear case; (iii) provide semiclassical scaling and geometrical optics for rotating BEC; (iv) find numerically the ratio between energies of different stationary states approaches to constant in

the semiclassical regime; (v) find the asymptotics of the energy of the ground state when the angular momentum velocity is near the minimal trapping frequency in xy plane; (vi) perform a numerical verification for dimension reduction from three dimensions (3D) to two dimensions (2D) and find the convergence rate; (vii) define the central vortex ground state and find the critical rotation speed for it numerically; (viii) study the TF approximation numerically; (ix) test different choices of initial data for the numerical method in an isotropic trap and find there is only one choice which always guarantees convergence to the ground state where it exists.

This chapter is organized as follows. In section 2.1, we take the three-dimensional GPE with an angular momentum term, scale it to get a four parameter model, reduce it to a two dimensional problem in a limiting regime, and present its semiclassical scaling and geometrical optics. In section 2.2, we present the minimization problem for stationary states such as ground state, symmetric state, central vortex states and central vortex ground state. We study the energy functional and (for the sake of completeness and readability) present a simple proof of existence of the ground state when the angular speed is less than the minimal trapping frequency in the xy plane, and resp., nonexistence of the ground state when the angular speed is bigger than the maximal trapping frequency in the xy plane. In section 2.3, we extend the GFDN and its BEFD discretization, proposed for non-rotating BEC in [8], to rotating BEC for computing those stationary states. In section 2.4, we report numerical results in 2D and 3D, and finally in section 2.5 we draw some conclusions.

2.1 GPE in a rotational frame

At temperatures T much smaller than the critical temperature T_c , a BEC in a rotational frame is well described by the macroscopic wave function $\psi(\mathbf{x}, t)$, whose evolution is governed by a self-consistent, mean field nonlinear Schrödinger equation known as the GPE with an angular momentum rotation term [4, 25, 49, 55], (w.l.o.g.)

assuming the rotation being around the z-axis:

$$\begin{aligned} i\hbar \frac{\partial \psi(\mathbf{x}, t)}{\partial t} &= \frac{\delta E(\psi)}{\delta \bar{\psi}} \\ &= \left(-\frac{\hbar^2}{2m} \nabla^2 + V(\mathbf{x}) + NU_0 |\psi(\mathbf{x}, t)|^2 - \Omega L_z \right) \psi(\mathbf{x}, t), \end{aligned} \quad (2.1)$$

where $\mathbf{x} = (x, y, z)^T \in \mathbb{R}^3$ is the spatial coordinate vector, m is the atomic mass, \hbar is the Planck constant, N is the number of atoms in the condensate, Ω is an angular velocity, $V(\mathbf{x})$ is an external trapping potential. When a harmonic trap potential is considered, $V(\mathbf{x}) = \frac{m}{2} (\omega_x^2 x^2 + \omega_y^2 y^2 + \omega_z^2 z^2)$ with ω_x , ω_y and ω_z being the trap frequencies in x -, y - and z -direction respectively. For the following we assume $\omega_x \leq \omega_y$. $U_0 = \frac{4\pi\hbar^2 a_s}{m}$ describes the interaction between atoms in the condensate with the s -wave scattering length a_s (positive for repulsive interaction and negative for attractive interaction) and

$$L_z = xp_y - yp_x = -i\hbar (x\partial_y - y\partial_x) \quad (2.2)$$

is the z -component of the angular momentum $\mathbf{L} = \mathbf{x} \times \mathbf{P}$ with the momentum operator $\mathbf{P} = -i\hbar \nabla = (p_x, p_y, p_z)^T$. The energy functional or Hamiltonian per particle $E(\psi)$ is defined as

$$E(\psi) = \int_{\mathbb{R}^3} \left[\frac{\hbar^2}{2m} |\nabla \psi|^2 + V(\mathbf{x}) |\psi|^2 + \frac{NU_0}{2} |\psi|^4 - \Omega \bar{\psi} L_z \psi \right] d\mathbf{x}. \quad (2.3)$$

Here we let \bar{f} denote the conjugate of a function f . It is convenient to normalize the wave function by requiring

$$\int_{\mathbb{R}^3} |\psi(\mathbf{x}, t)|^2 d\mathbf{x} = 1. \quad (2.4)$$

2.1.1 Dimensionless GPE

By introducing the dimensionless variables: $t \rightarrow t/\omega_m$ with $\omega_m = \min\{\omega_x, \omega_y, \omega_z\}$, $\mathbf{x} \rightarrow \mathbf{x}a_0$ with $a_0 = \sqrt{\hbar/m\omega_m}$, $\psi \rightarrow \psi/a_0^{3/2}$, $\Omega \rightarrow \omega_m \Omega$, and $E(\cdot) \rightarrow \hbar\omega_m E_{\beta, \Omega}(\cdot)$, we get the dimensionless GPE

$$\begin{aligned} i \frac{\partial \psi(\mathbf{x}, t)}{\partial t} &= \frac{\delta E_{\beta, \Omega}(\psi)}{\delta \bar{\psi}} \\ &= \left(-\frac{1}{2} \nabla^2 + V(\mathbf{x}) + \beta |\psi(\mathbf{x}, t)|^2 - \Omega L_z \right) \psi(\mathbf{x}, t), \end{aligned} \quad (2.5)$$

where $\beta = \frac{U_0 N}{a_0^3 \hbar \omega_x} = \frac{4\pi a_s N}{a_0}$, $L_z = -i(x\partial_y - y\partial_x)$, $V(\mathbf{x}) = \frac{1}{2}(\gamma_x^2 x^2 + \gamma_y^2 y^2 + \gamma_z^2 z^2)$ with $\gamma_x = \frac{\omega_y}{\omega_m}$, $\gamma_y = \frac{\omega_x}{\omega_m}$ and $\gamma_z = \frac{\omega_z}{\omega_m}$, and the dimensionless energy functional or Hamiltonian per particle $E_{\beta,\Omega}(\psi)$ is defined as

$$E_{\beta,\Omega}(\psi) = \int_{\mathbb{R}^3} \left[\frac{1}{2} |\nabla\psi(\mathbf{x}, t)|^2 + V(\mathbf{x})|\psi|^2 + \frac{\beta}{2} |\psi|^4 - \Omega \bar{\psi} L_z \psi \right] d\mathbf{x}. \quad (2.6)$$

2.1.2 Reduction to two dimensions

In a disk-shaped condensation with parameters $\omega_x \approx \omega_y$ and $\omega_z \gg \omega_x$ ($\Leftrightarrow \gamma_y \approx 1$ and $\gamma_z \gg 1$ by choosing $\omega_m = \omega_x$), the three-dimensional GPE (2.5) can be reduced to a two-dimensional GPE by assuming that the time evolution does not cause excitations along the z -axis, since the excitations along the z -axis have large energy (of order $\hbar\omega_z$) compared to that along the x and y -axis with energies of order $\hbar\omega_x$. Thus we may assume that the condensation wave function along the z -axis is always well described by the ground state wave function and set

$$\psi = \psi_2(x, y, t)\phi_3(z) \quad \text{with} \quad \phi_3(z) = \left(\int_{\mathbb{R}^2} |\phi_{\beta,\Omega}^g(x, y, z)|^2 dx dy \right)^{1/2} \approx \phi_{\text{ho}}(z), \quad (2.7)$$

where $\phi_{\beta,\Omega}^g(x, y, z)$ (see detail in the section 2.2.2) is the ground state solution of the three-dimensional GPE (2.5) and $\phi_{\text{ho}}(z) = (\gamma_z/\pi)^{1/4} e^{-\gamma_z z^2/2}$. Plugging (2.7) into (2.5), then multiplying by $\bar{\psi}_3(z)$, integrating with respect to z over $(-\infty, \infty)$, we get two-dimensional GPE with $\mathbf{x} = (x, y)^T$

$$i \frac{\partial \psi_2(\mathbf{x}, t)}{\partial t} = -\frac{1}{2} \nabla^2 \psi_2 + \frac{1}{2} (\gamma_x^2 x^2 + \gamma_y^2 y^2 + C) \psi_2 + \beta_2 |\psi_2|^2 \psi_2 - \Omega L_z \psi_2, \quad (2.8)$$

where

$$C = \gamma_z^2 \int_{-\infty}^{\infty} z^2 |\phi_3(z)|^2 dz + \int_{-\infty}^{\infty} \left| \frac{d\phi_3}{dz} \right|^2 dz, \quad \beta_2 = \beta \int_{-\infty}^{\infty} |\phi_3(z)|^4 dz \approx \beta \sqrt{\gamma_z/2\pi}.$$

Since this GPE is time-transverse invariant, we can replace $\psi_2 \rightarrow \psi e^{-iCt/2}$ which drops the constant C in the trap potential and obtain:

$$i \frac{\partial \psi(\mathbf{x}, t)}{\partial t} = -\frac{1}{2} \nabla^2 \psi + V_2(\mathbf{x})\psi + \beta_2 |\psi|^2 \psi - \Omega L_z \psi, \quad (2.9)$$

where $V_2(\mathbf{x}) = \frac{1}{2}(\gamma_x^2 x^2 + \gamma_y^2 y^2)$ and $\beta_2 \approx \beta\sqrt{\gamma_z/2\pi}$ [4, 8, 10]. Thus here we consider the dimensionless GPE in a rotational frame in d -dimensions ($d = 2, 3$):

$$i \frac{\partial \psi(\mathbf{x}, t)}{\partial t} = -\frac{1}{2} \nabla^2 \psi + V_d(\mathbf{x})\psi + \beta_d |\psi|^2 \psi - \Omega L_z \psi, \quad \mathbf{x} \in \mathbb{R}^d, \quad t \geq 0, \quad (2.10)$$

where $\beta_3 = \beta$ and $V_3(\mathbf{x}) = V(\mathbf{x})$.

Two important invariants of (2.10) are the normalization of the wave function

$$N(\psi) = \int_{\mathbb{R}^d} |\psi(\mathbf{x}, t)|^2 d\mathbf{x} \equiv \int_{\mathbb{R}^d} |\psi(\mathbf{x}, 0)|^2 d\mathbf{x} = 1, \quad t \geq 0 \quad (2.11)$$

and the energy

$$E_{\beta, \Omega}(\psi) = \int_{\mathbb{R}^d} \left[\frac{1}{2} |\nabla \psi(\mathbf{x}, t)|^2 + V_d(\mathbf{x}) |\psi|^2 + \frac{\beta_d}{2} |\psi|^4 - \Omega \bar{\psi} L_z \psi \right] d\mathbf{x}. \quad (2.12)$$

2.2 Stationary states

To find a stationary state, or a stationary solution of (2.10), we write

$$\psi(\mathbf{x}, t) = e^{-i\mu t} \phi(\mathbf{x}), \quad (2.13)$$

where μ is the chemical potential of the condensate and ϕ is independent of time.

Inserting (2.13) into (2.10) gives the following equation for $\phi(\mathbf{x})$

$$\mu \phi(\mathbf{x}) = -\frac{1}{2} \Delta \phi(\mathbf{x}) + V_d(\mathbf{x}) \phi(\mathbf{x}) + \beta_d |\phi(\mathbf{x})|^2 \phi(\mathbf{x}) - \Omega L_z \phi(\mathbf{x}), \quad \mathbf{x} \in \mathbb{R}^d, \quad (2.14)$$

under the normalization condition

$$\|\phi\|^2 = \int_{\mathbb{R}^d} |\phi(\mathbf{x})|^2 d\mathbf{x} = 1. \quad (2.15)$$

This is a nonlinear eigenvalue problem with a constraint and any eigenvalue μ can be computed from its corresponding eigenfunction ϕ by

$$\begin{aligned} \mu &= \mu_{\beta, \Omega}(\phi) = \int_{\mathbb{R}^d} \left[\frac{1}{2} |\nabla \phi(\mathbf{x})|^2 + V_d(\mathbf{x}) |\phi(\mathbf{x})|^2 + \beta_d |\phi(\mathbf{x})|^4 - \Omega \bar{\phi}(\mathbf{x}) L_z \phi(\mathbf{x}) \right] d\mathbf{x} \\ &= E_{\beta, \Omega}(\phi) + \int_{\mathbb{R}^d} \frac{\beta_d}{2} |\phi(\mathbf{x})|^4 d\mathbf{x}. \end{aligned} \quad (2.16)$$

In fact, the eigenfunctions of (2.14) under the constraint (2.15) are the critical points of the energy functional $E_{\beta, \Omega}(\phi)$ over the unit sphere $S = \{\phi \in C \mid \|\phi\| = 1, E_{\beta, \Omega}(\phi) < \infty\}$. Furthermore (2.14) is the Euler-Lagrange equation of the energy functional (2.12) with $\psi = \phi$ under the constraint (2.15).

2.2.1 Semiclassical scaling and geometrical optics

When $\beta_d \gg 1$, i.e. in a strongly repulsive interacting condensation or in semiclassical regime, another scaling (under the normalization (2.11) with $\psi = \psi^\varepsilon$) for the GPE (2.10) is also very useful in practice by choosing $\mathbf{x} \rightarrow \varepsilon^{-1/2}\mathbf{x}$ and $\psi = \psi^\varepsilon \varepsilon^{d/4}$ with $\varepsilon = \beta_d^{-2/(d+2)}$:

$$\begin{aligned} i\varepsilon \frac{\partial \psi^\varepsilon(\mathbf{x}, t)}{\partial t} &= \frac{\delta E_{\varepsilon, \Omega}(\psi^\varepsilon)}{\delta \bar{\psi}^\varepsilon} := H^\varepsilon \psi^\varepsilon \\ &= -\frac{\varepsilon^2}{2} \nabla^2 \psi^\varepsilon + V_d(\mathbf{x}) \psi^\varepsilon + |\psi^\varepsilon|^2 \psi^\varepsilon - \varepsilon \Omega L_z \psi^\varepsilon, \quad \mathbf{x} \in \mathbb{R}^d, \end{aligned} \quad (2.17)$$

where the energy functional $E_{\varepsilon, \Omega}(\psi^\varepsilon)$ is defined as

$$E_{\varepsilon, \Omega}(\psi^\varepsilon) = \int_{\mathbb{R}^3} \left[\frac{\varepsilon^2}{2} |\nabla \psi^\varepsilon|^2 + V_d(\mathbf{x}) |\psi^\varepsilon|^2 + \frac{1}{2} |\psi^\varepsilon|^4 - \varepsilon \Omega \bar{\psi}^\varepsilon L_z \psi^\varepsilon \right] d\mathbf{x} = O(1),$$

assuming that ψ^ε is ε -oscillatory and “sufficiently” integrable such that all terms have $O(1)$ -integral. Similarly, the nonlinear eigenvalue problem (2.14) (under the normalization (2.15) with $\phi = \phi^\varepsilon$) reads

$$\mu^\varepsilon \phi^\varepsilon(\mathbf{x}) = -\frac{\varepsilon^2}{2} \Delta \phi^\varepsilon + V_d(\mathbf{x}) \phi^\varepsilon + |\phi^\varepsilon|^2 \phi^\varepsilon - \varepsilon \Omega L_z \phi^\varepsilon, \quad \mathbf{x} \in \mathbb{R}^d, \quad (2.18)$$

where any eigenvalue μ^ε can be computed from its corresponding eigenfunction ϕ^ε by

$$\mu^\varepsilon = \mu_{\varepsilon, \Omega}(\phi^\varepsilon) = \int_{\mathbb{R}^d} \left[\frac{\varepsilon^2}{2} |\nabla \phi^\varepsilon|^2 + V_0(\mathbf{x}) |\phi^\varepsilon|^2 + |\phi^\varepsilon|^4 - \varepsilon \Omega \bar{\psi}^\varepsilon L_z \psi^\varepsilon \right] d\mathbf{x} = O(1).$$

Furthermore it is easy to get the leading asymptotics of the energy functional $E_{\beta, \Omega}(\psi)$ in (2.12) and the chemical potential $\mu_{\beta, \Omega}(\phi)$ in (2.16) when $\beta_d \gg 1$ from this scaling:

$$E_{\beta, \Omega}(\psi) = \varepsilon^{-1} E_{\varepsilon, \Omega}(\psi^\varepsilon) = O(\varepsilon^{-1}) = O(\beta_d^{2/(d+2)}), \quad (2.19)$$

$$\mu_{\beta, \Omega}(\phi) = \varepsilon^{-1} \mu_{\varepsilon, \Omega}(\phi^\varepsilon) = O(\varepsilon^{-1}) = O(\beta_d^{2/(d+2)}), \quad \beta_d \gg 1. \quad (2.20)$$

These asymptotic results will be confirmed by our numerical results in Section 2.4.

When $0 < \varepsilon \ll 1$, i.e. $\beta_d \gg 1$, we set

$$\psi^\varepsilon(\mathbf{x}, t) = \sqrt{\rho^\varepsilon(\mathbf{x}, t)} \exp\left(\frac{i}{\varepsilon} S^\varepsilon(\mathbf{x}, t)\right), \quad (2.21)$$

where $\rho^\varepsilon = |\psi^\varepsilon|^2$ and S^ε is the phase of the wave-function. Inserting (2.21) into (2.17) and collecting real and imaginary parts, we get the transport equation for ρ^ε and the Hamilton-Jacobi equation for the phase S^ε :

$$\partial_t \rho^\varepsilon + \operatorname{div}(\rho^\varepsilon \nabla S^\varepsilon) + \Omega(x\partial_y - y\partial_x)\rho^\varepsilon = 0, \quad (2.22)$$

$$\partial_t S^\varepsilon + \frac{1}{2}|\nabla S^\varepsilon|^2 + V_d(\mathbf{x}) + \rho^\varepsilon + \Omega(x\partial_y - y\partial_x)S^\varepsilon = \frac{\varepsilon^2}{2} \frac{1}{\sqrt{\rho^\varepsilon}} \Delta \sqrt{\rho^\varepsilon}. \quad (2.23)$$

2.2.2 Ground state

The ground state wave function $\phi^g(\mathbf{x}) := \phi_{\beta,\Omega}^g(\mathbf{x})$ of a rotating BEC is found by minimizing the energy functional $E_{\beta,\Omega}(\phi)$ over the unit sphere S :

Find $(\mu_{\beta,\Omega}^g, \phi_{\beta,\Omega}^g \in S)$ such that

$$E^g := E_{\beta,\Omega}^g = E_{\beta,\Omega}(\phi_{\beta,\Omega}^g) = \min_{\phi \in S} E_{\beta,\Omega}(\phi), \quad \mu^g := \mu_{\beta,\Omega}^g = \mu_{\beta,\Omega}(\phi_{\beta,\Omega}^g). \quad (2.24)$$

Any eigenfunction $\phi(\mathbf{x})$ of (2.14) under the constraint (2.15) whose energy $E_{\beta,\Omega}(\phi) > E_{\beta,\Omega}(\phi_{\beta,\Omega}^g)$ is usually called an excited state in the physics literature [104]

Existence/nonexistence results for ground states, depending on the magnitude $|\Omega|$ of the angular velocity relative to the trapping frequencies are known and can be found in [83, 118, 119]. For the sake of readability we include the sketch of the proof here.

Existence of the ground state when $|\Omega| < \gamma_{xy} := \min\{\gamma_x, \gamma_y\}$

To study the existence of the ground state in rotating BEC, we first present some properties of the energy functional.

Lemma 2.2.1 *i) In 2D, we have*

$$E_{\beta,-\Omega}(\phi(x, -y)) = E_{\beta,\Omega}(\phi(x, y)), \quad E_{\beta,-\Omega}(\phi(-x, y)) = E_{\beta,\Omega}(\phi(x, y)), \quad \phi \in S. \quad (2.25)$$

ii) In 3D, we have

$$E_{\beta,-\Omega}(\phi(x, -y, z)) = E_{\beta,\Omega}(\phi(x, y, z)), \quad E_{\beta,-\Omega}(\phi(-x, y, z)) = E_{\beta,\Omega}(\phi(x, y, z)), \quad \phi \in S. \quad (2.26)$$

iii) In 2D and 3D, we have

$$\begin{aligned} & \int_{\mathbb{R}^d} \left[\frac{1-|\Omega|}{2} |\nabla\phi(\mathbf{x})|^2 + \left(V_d(\mathbf{x}) - \frac{|\Omega|}{2}(x^2+y^2) \right) |\phi|^2 + \frac{\beta_d}{2} |\phi|^4 \right] d\mathbf{x} \leq E_{\beta,\Omega}(\phi) \\ & \leq \int_{\mathbb{R}^d} \left[\frac{1+|\Omega|}{2} |\nabla\phi(\mathbf{x})|^2 + \left(V_d(\mathbf{x}) + \frac{|\Omega|}{2}(x^2+y^2) \right) |\phi|^2 + \frac{\beta_d}{2} |\phi|^4 \right] d\mathbf{x}. \end{aligned} \quad (2.27)$$

Proof: i) From (2.12) with $\psi = \phi$ and $d = 2$, observing (2.2), with a change of variables, we have

$$\begin{aligned} E_{\beta,-\Omega}(\phi(x,-y)) &= \int_{\mathbb{R}^2} \left[\frac{1}{2} |\nabla\phi(x,-y)|^2 + V_d(\mathbf{x}) |\phi(x,-y)|^2 \right. \\ &\quad \left. + \frac{\beta_d}{2} |\phi(x,-y)|^4 + \Omega \bar{\phi}(x,-y) L_z \phi(x,-y) \right] dx dy \\ &\stackrel{y \rightarrow -y}{=} \int_{\mathbb{R}^2} \left[\frac{1}{2} |\nabla\phi(x,y)|^2 + V_d(\mathbf{x}) |\phi(x,y)|^2 \right. \\ &\quad \left. + \frac{\beta_d}{2} |\phi(x,y)|^4 - \Omega \bar{\phi}(x,y) L_z \phi(x,y) \right] dx dy \\ &= E_{\beta,\Omega}(\phi(x,y)), \quad \phi \in S. \end{aligned} \quad (2.28)$$

Similarly, we obtain the second equality in (2.25).

ii) From (2.12) with $\psi = \phi$ and $d = 3$, with a change of variables, we have

$$\begin{aligned} E_{\beta,-\Omega}(\phi(x,-y,z)) &= \int_{\mathbb{R}^3} \left[\frac{1}{2} |\nabla\phi(x,-y,z)|^2 + V_d(\mathbf{x}) |\phi(x,-y,z)|^2 \right. \\ &\quad \left. + \frac{\beta_d}{2} |\phi(x,-y,z)|^4 + \Omega \bar{\phi}(x,-y,z) L_z \phi(x,-y,z) \right] dx dy \\ &\stackrel{y \rightarrow -y}{=} \int_{\mathbb{R}^3} \left[\frac{1}{2} |\nabla\phi(x,y,z)|^2 + V_d(\mathbf{x}) |\phi(x,y,z)|^2 \right. \\ &\quad \left. + \frac{\beta_d}{2} |\phi(x,y,z)|^4 - \Omega \bar{\phi}(x,y,z) L_z \phi(x,y,z) \right] dx dy \\ &= E_{\beta,\Omega}(\phi(x,y,z)), \quad \phi \in S. \end{aligned} \quad (2.29)$$

Similarly, we can obtain the second equality in (2.26).

iii) From (2.2), the Hölder inequality, we have

$$\begin{aligned} & \left| \int_{\mathbb{R}^d} -\Omega \bar{\phi}(\mathbf{x}) L_z \phi(\mathbf{x}) d\mathbf{x} \right| \leq |\Omega| \int_{\mathbb{R}^d} |\bar{\phi}(\mathbf{x}) L_z \phi(\mathbf{x})| d\mathbf{x} \\ &= |\Omega| \int_{\mathbb{R}^d} |\bar{\phi}(\mathbf{x}) (x \partial_y \phi - y \partial_x \phi)| d\mathbf{x} \leq |\Omega| \int_{\mathbb{R}^d} [|x \bar{\phi}| |\partial_y \phi| + |y \bar{\phi}| |\partial_x \phi|] d\mathbf{x} \\ &\leq \frac{|\Omega|}{2} \int_{\mathbb{R}^d} [(|\partial_x \phi|^2 + |\partial_y \phi|^2) + (x^2 + y^2) |\phi|^2] d\mathbf{x}. \end{aligned} \quad (2.30)$$

Thus the inequality (2.27) is a combination of (2.30) and (2.12) with $\psi = \phi$.

From this lemma, since $\gamma_y \geq \gamma_x$ and $\gamma_z > 0$, when $\beta_d \geq 0$ and $|\Omega| < \gamma_{xy}$, we know that the energy functional $E_{\beta,\Omega}(\phi)$ is positive, coercive and weakly lower semicontinuous on S . Thus the existence of a minimum follows from the standard theory [121] and we have

Theorem 2.2.1 *i) In 2D, if $\phi_{\beta,\Omega}(x, y) \in S$ is a ground state of the energy functional $E_{\beta,\Omega}(\phi)$, then $\phi_{\beta,\Omega}(x, -y) \in S$ and $\phi_{\beta,\Omega}(-x, y) \in S$ are ground states of the energy functional $E_{\beta,-\Omega}(\phi)$. Furthermore*

$$E_{\beta,\Omega}^g = E_{\beta,-\Omega}^g, \quad \mu_{\beta,\Omega}^g = \mu_{\beta,-\Omega}^g. \quad (2.31)$$

ii) In 3D, if $\phi_{\beta,\Omega}(x, y, z) \in S$ is a ground state of the energy functional $E_{\beta,\Omega}(\phi)$, then $\phi_{\beta,\Omega}(x, -y, z) \in S$ and $\phi_{\beta,\Omega}(-x, y, z) \in S$ are ground states of the energy functional $E_{\beta,-\Omega}(\phi)$, and (2.31) is also valid.

iii). When $\beta_d \geq 0$ and $|\Omega| < \gamma_{xy}$, there exists a minimizer for the minimization problem (2.24), i.e. there exist ground states.

For understanding the uniqueness question note that $E_{\beta,\Omega}(\alpha\phi_{\beta,\Omega}^g) = E_{\beta,\Omega}(\phi_{\beta,\Omega}^g)$ for all $\alpha \in C$ with $|\alpha| = 1$. Thus an additional constraint has to be introduced to show uniqueness. For non-rotating BEC, i.e. $\Omega = 0$, the unique positive minimizer is usually taken as the ground state. In fact, the ground state is unique up to a constant α with $|\alpha| = 1$, i.e. density of the ground state is unique, in this case. For rotating BEC under $|\Omega| < \gamma_{xy}$, in section 2.3, we present a GFDN and its BEFD discretization for computing a minimizer of the minimization problem (2.24) with appropriately chosen initial data. From our numerical results, the density of the ground state is no longer unique when $|\Omega| > \Omega^c$ with Ω^c a critical angular rotation speed.

Nonexistence of ground states when $|\Omega| > \gamma^{xy} := \max\{\gamma_x, \gamma_y\}$

Denoting $\gamma_r = \gamma^{xy}$ and noticing $\frac{1}{2}(\gamma_x^2 x^2 + \gamma_y^2 y^2) \leq \frac{1}{2}\gamma_r^2 r^2$ with $r = \sqrt{x^2 + y^2}$, we have

$$E_{\beta,\Omega}(\phi) \leq \frac{1}{2} \int_0^{2\pi} \int_0^\infty \left[|\partial_r \phi|^2 + \frac{1}{r^2} |\partial_\theta \phi|^2 + \gamma_r^2 r^2 |\phi|^2 + \beta_2 |\phi|^4 + 2i\Omega \bar{\phi} \partial_\theta \phi \right] r \, dr d\theta, \quad d = 2, \quad (2.32)$$

$$E_{\beta,\Omega}(\phi) \leq \frac{1}{2} \int_{-\infty}^\infty \int_0^{2\pi} \int_0^\infty \left[|\partial_r \phi|^2 + \frac{1}{r^2} |\partial_\theta \phi|^2 + |\partial_z \phi|^2 + (\gamma_r^2 r^2 + \gamma_z^2 z^2) |\phi|^2 + \beta_2 |\phi|^4 + 2i\Omega \bar{\phi} \partial_\theta \phi \right] r \, dr d\theta dz, \quad d = 3, \quad (2.33)$$

where (r, θ) and (r, θ, z) are polar (in 2D), and resp., cylindrical coordinates (in 3D).

In 2D, let

$$\phi_m(\mathbf{x}) = \phi_m(r, \theta) = \phi_m(r) e^{im\theta}, \quad \text{with} \quad \phi_m(r) = \frac{\gamma_r^{(|m|+1)/2}}{\sqrt{\pi|m|!}} r^{|m|} e^{-\frac{\gamma_r r^2}{2}}, \quad (2.34)$$

where m is an integer. In fact, $\phi_m(\mathbf{x})$ is the central vortex state with winding number m of the GPE (2.10) with $d = 2$, $\beta_d = 0$ and $\Omega = 0$. It is very easy to check that ϕ_m satisfies

$$\|\phi_m\| = 2\pi \int_0^\infty |\phi_m(r)|^2 r \, dr = 1, \quad m \in \mathbb{Z}, \quad (2.35)$$

$$\frac{1}{2} \left[-\frac{1}{r} \frac{d}{dr} \left(r \frac{d}{dr} \right) + \gamma_r^2 r^2 + \frac{m^2}{r^2} \right] \phi_m(r) = \gamma_r (|m| + 1) \phi_m(r), \quad 0 < r < \infty. \quad (2.36)$$

Thus $\phi_m(\mathbf{x}) \in S$ and we compute

$$\begin{aligned} E_{\beta,\Omega}(\phi_m(\mathbf{x})) &\leq (|m| + 1)\gamma_r - \Omega m + \beta_2 \pi \int_0^\infty |\phi_m(r)|^4 r \, dr \\ &= (|m| + 1)\gamma_r - \Omega m + \frac{\beta_2 (2|m|)!}{4\pi (2^{|m|} (|m|!))^2}. \end{aligned} \quad (2.37)$$

Thus when $|\Omega| > \gamma_r$, we have

$$\begin{aligned} \inf_{\phi \in S} E_{\beta,\Omega}(\phi) &\leq \begin{cases} \lim_{m \rightarrow \infty} E_{\beta,\Omega}(\phi_m) & \Omega > 0 \\ \lim_{m \rightarrow \infty} E_{\beta,\Omega}(\phi_{-m}) & \Omega < 0 \end{cases} \\ &= \lim_{m \rightarrow \infty} (\gamma_r - |\Omega|)|m| + 1 + \frac{\beta_2 (2|m|)!}{4\pi (2^{|m|} (|m|!))^2} \\ &= -\infty. \end{aligned} \quad (2.38)$$

This implies that there is no minimizer of the minimization problem (2.24) when $|\Omega| > \gamma^{xy}$ in 2D.

Similarly, in 3D, the argument proceeds with the central vortex line state with winding number m

$$\phi_m(\mathbf{x}) = \phi_m(r, \theta, z) = \phi_m(r, z) e^{im\theta}, \quad \text{with } \phi_m(r, z) = \frac{\gamma_r^{(|m|+1)/2} \gamma_z^{1/4}}{\pi^{3/4} \sqrt{|m|!}} r^{|m|} e^{-\frac{\gamma r^2 + \gamma z^2}{2}}, \quad (2.39)$$

and we conclude that there is no minimizer of the minimization problem (2.24) when $|\Omega| > \gamma^{xy}$ in 3D.

Remark 2.2.1 *When $\gamma_{xy} < |\Omega| < \gamma^{xy}$ in an anisotropic trap, although there is no rigorous mathematical justification, our numerical results in the subsection 2.4 show that there is no ground state of the energy functional $E_{\beta, \Omega}(\phi)$.*

Remark 2.2.2 *Suppose $\beta_d = 0$, $|\Omega| < \gamma_{xy}$ and $V_d(\mathbf{x}) \geq 0$ for $\mathbf{x} \in \mathbb{R}^d$, we have:*

- (i). *The ground state ϕ^g is a global minimizer of $E_{\beta, \Omega}$ over S .*
- (ii). *Any excited state ϕ^e is a saddle point of $E_{\beta, \Omega}$ over S .*

2.2.3 Approximate ground state

When $\beta_d = 0$ and $\Omega = 0$, the ground state solution is given explicitly [8]

$$\mu_{0,0}^g = \frac{1}{2} \begin{cases} 1 + \gamma_y, \\ 1 + \gamma_y + \gamma_z, \end{cases} \quad \phi_{0,0}^g(\mathbf{x}) = \frac{1}{\pi^{d/4}} \begin{cases} (\gamma_y)^{1/4} e^{-(x^2 + \gamma_y y^2)/2}, & d = 2, \\ (\gamma_y \gamma_z)^{1/4} e^{-(x^2 + \gamma_y y^2 + \gamma_z z^2)/2}, & d = 3. \end{cases} \quad (2.40)$$

In fact, this solution can be viewed as an approximation of the ground state for a weakly interacting slowly rotating condensate, i.e., $|\beta_d| \ll 1$ and $|\Omega| \approx 0$.

For a condensate with strong repulsive interaction, i.e. $\beta_d \gg 1$, $|\Omega| \approx 0$ and $\gamma_\alpha = O(1)$ ($\alpha = y, z$), the ground state can be approximated by the Thomas-Fermi (TF) approximation in this regime [4, 10]:

$$\phi_\beta^{\text{TF}}(\mathbf{x}) = \begin{cases} \sqrt{(\mu_\beta^{\text{TF}} - V_d(\mathbf{x}))/\beta_d}, & V_d(\mathbf{x}) < \mu_\beta^{\text{TF}}, \\ 0, & \text{otherwise,} \end{cases} \quad (2.41)$$

$$\mu_\beta^{\text{TF}} = \frac{1}{2} \begin{cases} (4\beta_2 \gamma_y / \pi)^{1/2}, & d = 2, \\ (15\beta_3 \gamma_y \gamma_z / 4\pi)^{2/5}, & d = 3. \end{cases} \quad (2.42)$$

Due to ϕ_β^{TF} is not differentiable at $V_d(\mathbf{x}) = \mu_\beta^{\text{TF}}$, thus $E_{\beta,\Omega}(\phi_\beta^{\text{TF}}) = \infty$ and $\mu_{\beta,\Omega}(\phi_\beta^{\text{TF}}) = \infty$ [9, 10]. This shows that we can't use (2.12) to define the energy of the TF approximation (2.41). How to define the energy of the Thomas-Fermi approximation is not clear in the literatures. Using (2.16), (2.42) and (2.41), here we present a way to define the energy of the TF approximation (2.41) [9, 10]:

$$E_{\beta,\Omega}^{\text{TF}} = \mu_{\beta,\Omega}^{\text{TF}} - \int_{\mathbb{R}^d} \frac{\beta_d}{2} |\phi_\beta^{\text{TF}}(\mathbf{x})|^4 d\mathbf{x} = \frac{d+2}{d+4} \mu_\beta^{\text{TF}}, \quad d = 2, 3. \quad (2.43)$$

Our numerical results in Section 2.4 show that the TF approximation is very accurate in the regime $\beta_d \gg 1$ and $|\Omega| \approx 0$, but diverges in the regime $\beta_d \gg 1$ and $|\Omega| \approx 1$.

2.2.4 Excited states

In this subsection, we present central vortex ground state, symmetric, central vortex states and their energies of rotating BEC in 2D with radial symmetry and 3D with cylindrical symmetry, i.e., $\gamma_x = \gamma_y = 1$ in (2.10). These states as well as their stability and interaction were widely studied in non-rotating BEC [8, 10, 11, 26, 27, 70, 71]. They are also very interesting in rotating BEC [25, 48, 91, 108, 54]. In fact, they will be used as initial data for studying quantized vortex stability [87, 55, 49], and dynamics [96, 123].

Central vortex ground state

One interesting excited state is a vortex state whose energy minimizes the energy functional among all $\phi \in S$ which is locally a central vortex near the origin in 2D and a central vortex line near the z -axis in 3D. To be specific, in 2D, let

$$S_v = \{\phi(\mathbf{x}) \in C \mid \|\phi\| = 1, E_{\beta,\Omega}(\phi) < \infty, \phi(0,0) = 0, (0,0) \text{ is a vortex center of } \phi\}$$

and in 3D

$$S_v = \left\{ \phi(\mathbf{x}) \in C \mid \|\phi\| = 1, E_{\beta,\Omega}(\phi) < \infty, \phi(0,0,z) = 0, (0,0,z) (z \in \mathbb{R}) \right. \\ \left. \text{is a vortex line of } \phi \right\}.$$

It is easy to see that S_v is a subset of the unit sphere S , i.e. $S_v \subset S$. Then the central vortex ground state $\phi^v(\mathbf{x}) := \phi_{\beta,\Omega}^v(\mathbf{x})$ is found by minimizing the energy functional $E_{\beta,\Omega}(\phi)$ over the set $S_v \subset S$:

Find $(\mu_{\beta,\Omega}^v, \phi_{\beta,\Omega}^v \in S_v)$ such that

$$E^v := E_{\beta,\Omega}^v = E_{\beta,\Omega}(\phi_{\beta,\Omega}^v) = \min_{\phi \in S_v} E_{\beta,\Omega}(\phi), \quad \mu^v := \mu_{\beta,\Omega}^v = \mu_{\beta,\Omega}(\phi_{\beta,\Omega}^v). \quad (2.44)$$

Similarly as the proof for ground state, we have the following theorem for central vortex ground state:

Theorem 2.2.2 *i) In 2D, if $\phi_{\beta,\Omega}(x, y) \in S_v$ is a central vortex ground state of the energy functional $E_{\beta,\Omega}(\phi)$, then $\phi_{\beta,\Omega}(x, -y) \in S_v$ and $\phi_{\beta,\Omega}(-x, y) \in S_v$ are central vortex ground states of the energy functional $E_{\beta,-\Omega}(\phi)$. Furthermore*

$$E_{\beta,\Omega}^v = E_{\beta,-\Omega}^v, \quad \mu_{\beta,\Omega}^v = \mu_{\beta,-\Omega}^v. \quad (2.45)$$

ii) In 3D, if $\phi_{\beta,\Omega}(x, y, z) \in S_v$ is a central vortex ground state of the energy functional $E_{\beta,\Omega}(\phi)$, then $\phi_{\beta,\Omega}(x, -y, z) \in S_v$ and $\phi_{\beta,\Omega}(-x, y, z) \in S_v$ are central vortex ground states of the energy functional $E_{\beta,-\Omega}(\phi)$, and (2.45) is also valid.

iii). When $\beta_d \geq 0$ and $|\Omega| < \gamma_{xy}$, there exists a minimizer for the minimization problem (2.44), i.e. there exists central vortex ground state.

iv). When $\beta_d \geq 0$ and $|\Omega| > \gamma^{xy}$, there exists no central vortex ground state.

Symmetric and central vortex states

In 2D with radially symmetric trap, i.e. $d = 2$ and $\gamma_x = \gamma_y = 1$ in (2.10), we set

$$\psi(\mathbf{x}, t) = e^{-i\mu_m t} \phi_m(x, y) = e^{-i\mu_m t} \phi_m(r) e^{im\theta}, \quad (2.46)$$

where m is an integer which corresponds to a symmetric state when $m = 0$ and to central vortex states when $m \neq 0$ (m is usually called index or winding number in this case), μ_m is the chemical potential, and $\phi_m(r)$ is a real function independent of time t and angle θ . Inserting (2.46) into (2.10) gives the following equation for

$\phi_m(r)$ with $0 < r < \infty$

$$\mu_m \phi_m(r) = \frac{1}{2} \left[-\frac{1}{r} \frac{d}{dr} \left(r \frac{d}{dr} \right) + r^2 + \frac{m^2}{r^2} + 2\beta_2 |\phi_m|^2 - 2m\Omega \right] \phi_m, \quad (2.47)$$

$$\phi'_m(0) = 0 \quad (m = 0), \quad \text{and resp.} \quad \phi_m(0) = 0 \quad (m \neq 0), \quad (2.48)$$

$$\lim_{r \rightarrow \infty} \phi_m(r) = 0. \quad (2.49)$$

under the normalization condition

$$2\pi \int_0^\infty |\phi_m(r)|^2 r dr = 1. \quad (2.50)$$

In order to find the radially symmetric state ($m = 0$), and resp., central vortex states with index m ($m \neq 0$), $\phi_{\beta,\Omega}^m(x, y) = \phi_{\beta,\Omega}^m(r) e^{im\theta}$, we find a real nonnegative function $\phi^m(r) := \phi_{\beta,\Omega}^m(r)$ which minimizes the energy functional

$$\begin{aligned} E_{\beta,\Omega}^m(\phi(r)) &= E_{\beta,\Omega}(\phi(r) e^{im\theta}) \\ &= \pi \int_0^\infty \left[|\phi'(r)|^2 + \left(r^2 + \frac{m^2}{r^2} \right) |\phi(r)|^2 + \beta_2 |\phi(r)|^4 - 2m\Omega |\phi(r)|^2 \right] r dr \\ &= E_{\beta,0}^m(\phi(r)) - m\Omega, \quad \Omega \in \mathbb{R}, \end{aligned} \quad (2.51)$$

over the set $S_0 = \{\phi(r) \in \mathbb{R} \mid 2\pi \int_0^\infty |\phi(r)|^2 r dr = 1, E_{\beta,0}^m(\phi) < \infty, \phi'(0) = 0 \text{ (} m = 0 \text{), and resp. } \phi(0) = 0 \text{ (} m \neq 0 \text{)}\}$. The existence and uniqueness of nonnegative minimizer for this minimization problem can be obtained similarly as for the ground state. Note that the set $S_m = \{\phi(r) e^{im\theta} \mid \phi \in S_0\} \subset S$ is a subset of the unit sphere, so $\phi_{\beta,\Omega}^m(r) e^{im\theta}$ is a minimizer of the energy functional $E_{\beta,\Omega}(\phi)$ over the set $S_m \subset S$. When $\beta_2 = 0$ and $\Omega = 0$ in (2.10), $\phi_{0,0}^m(r) = \frac{1}{\sqrt{\pi|m|!}} r^{|m|} e^{-r^2/2}$ [8].

Similarly, in order to find the cylindrically symmetric state ($m = 0$), and resp. central vortex line states ($m \neq 0$), in 3D with cylindrical symmetry, i.e. $d = 3$ and $\gamma_x = \gamma_y = 1$ in (2.10), we write

$$\psi(\mathbf{x}, t) = e^{-i\mu_m t} \phi_m(x, y, z) = e^{-i\mu_m t} \phi_m(r, z) e^{im\theta}, \quad (2.52)$$

where m is an integer and called as index when $m \neq 0$, μ_m is the chemical potential, and $\phi_m(r, z)$ is a real function independent of time and angle. Inserting (2.52) into

(2.10) with $d = 3$ gives the following equation for $\phi_m(r, z)$

$$\begin{aligned} \mu_m \phi_m &= \frac{1}{2} \left[-\frac{1}{r} \frac{\partial}{\partial r} \left(r \frac{\partial}{\partial r} \right) - \frac{\partial^2}{\partial z^2} + r^2 + \frac{m^2}{r^2} + \gamma_z^2 z^2 + 2\beta_3 |\phi_m|^2 - 2m\Omega \right] \phi_m, \\ \partial_r \phi_m(0, z) &= 0 \quad (m = 0), \text{ and resp. } \phi_m(0, z) = 0 \quad (m \neq 0), \quad z \in \mathbb{R}, \\ \lim_{r \rightarrow \infty} \phi_m(r, z) &= 0, \quad -\infty < z < \infty, \quad \lim_{|z| \rightarrow \infty} \phi(r, z) = 0, \quad 0 \leq r < \infty, \end{aligned}$$

under the normalization condition

$$2\pi \int_0^\infty \int_{-\infty}^\infty |\phi_m(r, z)|^2 r \, dr dz = 1. \quad (2.53)$$

In order to find the cylindrically symmetric state ($m = 0$), and resp. central vortex line states ($m \neq 0$) $\phi_{\beta, \Omega}^m(x, y, z) = \phi_{\beta, \Omega}^m(r, z)e^{im\theta}$, we compute a real nonnegative function $\phi^m(r, z) := \phi_{\beta, \Omega}^m(r, z)$ which minimizes the energy functional

$$\begin{aligned} E_{\beta, \Omega}^m(\phi(r, z)) &= E_{\beta, \Omega}(\phi(r, z)e^{im\theta}) \\ &= \pi \int_0^\infty \int_{-\infty}^\infty \left[|\partial_r \phi|^2 + |\partial_z \phi|^2 + \left(r^2 + \gamma_z^2 z^2 + \frac{m^2}{r^2} - 2m\Omega \right) |\phi|^2 + \beta_3 |\phi|^4 \right] r \, dr dz \\ &= E_{\beta, 0}^m(\phi(r, z)) - m\Omega, \quad \Omega \in \mathbb{R}, \end{aligned} \quad (2.54)$$

over the set $S_0 = \{\phi(r, z) \in \mathbb{R} \mid 2\pi \int_0^\infty \int_{-\infty}^\infty |\phi(r, z)|^2 r \, dr dz = 1, E_{\beta, 0}^m(\phi) < \infty, \partial_r \phi(0, r) = 0 \quad (m=0), \text{ and resp. } \phi(0, z) = 0 \quad (m \neq 0), -\infty < z < \infty\}$. The existence and uniqueness of a nonnegative minimizer for this minimization problem can be obtained similarly as for the ground state. Note that the set $S_m = \{\phi(r, z)e^{im\theta} \mid \phi \in S_0\} \subset S$ is a subset of the unit sphere, so $\phi_{\beta, \Omega}^m(r, z)e^{im\theta}$ is a minimizer of the energy functional $E_{\beta, \Omega}(\phi)$ over the set $S_m \subset S$. When $\beta_3 = 0$ and $\Omega = 0$ in (2.10), $\phi_{0, 0}^m(r, z) = \frac{\gamma_z^{1/4}}{\pi^{3/4} \sqrt{|m|!}} r^{|m|} e^{-(r^2 + \gamma_z z^2)/2}$ [8].

When $\beta_d > 0$, the continuous normalized gradient flow and its backward Euler finite difference discretization proposed in [8] for $\Omega = 0$ can be applied directly to compute the central vortex states for $\Omega \neq 0$.

From the above discussions, for symmetric states and central vortex states in rotating BEC, we have

Lemma 2.2.2 *i) The radially (in 2D) and cylindrically (in 3D) symmetric states, and central vortex states are independent of the angular momentum term, i.e.*

$$\phi_{\beta,\Omega}^m = \phi_{\beta,0}^m, \quad \beta_d \geq 0, \quad \Omega \in \mathbb{R}, \quad m \in \mathbb{Z}.$$

ii) The energy and chemical potential are independent of Ω for the symmetric states, and resp. are changing linearly with respect to Ω for the central vortex states, i.e.

$$\begin{aligned} E^m &: = E_{\beta,\Omega}^m(\phi_{\beta,\Omega}^m) = E_{\beta,0}^m(\phi_{\beta,0}^m) - m\Omega, \\ \mu^m &: = \mu_{\beta,\Omega}^m(\phi_{\beta,\Omega}^m) = \mu_{\beta,0}^m(\phi_{\beta,0}^m) - m\Omega, \quad \beta_d \geq 0, \quad \Omega \in \mathbb{R}, \quad m \in \mathbb{Z}. \end{aligned}$$

iii) When $\Omega = 0$ & $\beta_d \geq 0$, the symmetric state is the same as the ground state, i.e. $\phi_{\beta,\Omega}^0 = \phi_{\beta,\Omega}^g$, and the central vortex state with index $m = 1$ is the same as the central vortex ground state, i.e. $\phi_{\beta,\Omega}^1 = \phi_{\beta,\Omega}^v$.

2.2.5 Critical angular velocity in symmetric trap

In 2D with radial symmetry and in 3D with cylindrical symmetry, for any $\beta_d \geq 0$, when $\Omega = 0$, the ground state satisfies $\phi_{\beta,0}^g(\mathbf{x}) = \phi_{\beta,0}^0(r)$ in 2D and $\phi_{\beta,0}^g(\mathbf{x}) = \phi_{\beta,0}^0(r, z)$ in 3D, i.e. the ground state is symmetric. When Ω increases to a critical angular velocity, Ω_β^c , defined as

$$\Omega^c := \Omega_\beta^c = \max \left\{ \Omega \mid E_{\beta,\Omega}(\phi_{\beta,\Omega}^g) = E_{\beta,\Omega}(\phi_{\beta,\Omega}^0) = E_{\beta,0}(\phi_{\beta,0}^0) \right\},$$

the energy of the ground state will be less than that of the symmetric state, i.e. symmetry breaking occurs in the ground state [118, 119]. Ω_β^c is also called as critical angular velocity for symmetry breaking in the ground state.

Similarly, for any $\beta_d \geq 0$, when $\Omega = 0$, the central vortex ground state satisfies $\phi_{\beta,\Omega}^v(\mathbf{x}) = \phi_{\beta,0}^1(r)e^{i\theta}$ in 2D and $\phi_{\beta,\Omega}^v(\mathbf{x}) = \phi_{\beta,0}^1(r, z)e^{i\theta}$ in 3D. When Ω increases to a critical angular velocity, Ω_β^v , defined as

$$\Omega^v := \Omega_\beta^v = \max \left\{ \Omega \mid E_{\beta,\Omega}(\phi_{\beta,\Omega}^v) = E_{\beta,\Omega}^1(\phi_{\beta,0}^1) - \Omega \right\},$$

the energy of $\phi_{\beta,\Omega}^v$ will be less than that of the index 1 central vortex state. We call Ω_β^v as critical angular velocity for symmetry breaking in the central vortex ground state.

From the above discussions and our numerical computations presented later, we find

$$\Omega_0^c = \Omega_0^v = 1, \quad 0 \leq \Omega_\beta^c < \Omega_\beta^v \leq 1, \quad \text{for } \beta_d > 0.$$

2.3 Numerical methods for stationary states

In this section, we extend the GFDN and its BEFD discretization, proposed in [8] for computing ground states of non-rotating BEC, to compute ground state and central vortex ground states of rotating BEC, i.e. minimizers of (2.24) and (2.44).

2.3.1 Gradient flow with discrete normalization(GFDN)

Various algorithms e.g. imaginary time method [4, 5], Sobolev gradient method [54, 56], finite element approximation [10, 141], iterative method [30] etc., for finding the minimizer of the minimization problem (2.24) have been studied in the literature. Perhaps one of the more popular technique for dealing with the normalization constraint (2.15) is through the splitting (or projection) scheme: (i). Apply the steepest descent method to an unconstrained minimization problem; (ii) project the solution back to the unit sphere S . This suggests us to consider GFDN:

$$\phi_t = -\frac{\delta E_{\beta,\Omega}(\phi)}{\delta \bar{\phi}} = \frac{1}{2}\Delta\phi - V_d(\mathbf{x})\phi - \beta_d |\phi|^2\phi + \Omega L_z\phi, \quad t_n < t < t_{n+1}, \quad (2.55)$$

$$\phi(\mathbf{x}, t_{n+1}) \triangleq \phi(\mathbf{x}, t_{n+1}^+) = \frac{\phi(\mathbf{x}, t_{n+1}^-)}{\|\phi(\cdot, t_{n+1}^-)\|}, \quad \mathbf{x} \in \mathbb{R}^d, \quad n \geq 0, \quad (2.56)$$

$$\phi(\mathbf{x}, 0) = \phi_0(\mathbf{x}), \quad \mathbf{x} \in \mathbb{R}^d \quad \text{with} \quad \|\phi_0\| = 1; \quad (2.57)$$

where $0 = t_0 < t_1 < t_2 < \dots < t_n < \dots$ with $\Delta t_n = t_{n+1} - t_n > 0$ and $k = \max_{n \geq 0} \Delta t_n$, and $\phi(\mathbf{x}, t_n^\pm) = \lim_{t \rightarrow t_n^\pm} \phi(\mathbf{x}, t)$. In fact, the gradient flow (2.55) can be viewed as applying the steepest descent method to the energy functional $E_{\beta,\Omega}(\phi)$

without constraint and (2.56) then projects the solution back to the unit sphere in order to satisfy the constraint (2.15). From the numerical point of view, the gradient flow (2.55) can be solved via traditional techniques and the normalization of the gradient flow is simply achieved by a projection at the end of each time step.

2.3.2 Energy diminishing

Let

$$\tilde{\phi}(\cdot, t) = \frac{\phi(\cdot, t)}{\|\phi(\cdot, t)\|}, \quad t_n \leq t \leq t_{n+1}, \quad n \geq 0. \quad (2.58)$$

For the gradient flow (2.55), it is easy to establish the following basic facts:

Lemma 2.3.1 *Suppose $V_d(\mathbf{x}) \geq 0$ for all $\mathbf{x} \in \mathbb{R}^d$, $\beta_d \geq 0$ and $\|\phi_0\| = 1$, then*

(i). $\|\phi(\cdot, t)\| \leq \|\phi(\cdot, t_n)\|$ for $t_n \leq t \leq t_{n+1}$, $n \geq 0$.

(ii). For any $\beta_d \geq 0$, and all t', t with $t_n \leq t' < t \leq t_{n+1}$:

$$E_{\beta, \Omega}(\phi(\cdot, t)) \leq E_{\beta, \Omega}(\phi(\cdot, t')). \quad (2.59)$$

(iii). For $\beta_d = 0$,

$$E_{0, \Omega}(\tilde{\phi}(\cdot, t)) \leq E_{0, \Omega}(\tilde{\phi}(\cdot, t_n)), \quad t_n \leq t \leq t_{n+1}, \quad n \geq 0. \quad (2.60)$$

Proof: (i)

$$\begin{aligned} \frac{d}{dt} \|\phi(\cdot, t)\|^2 &= \int_{\mathbb{R}^d} (\phi_t \bar{\phi} + \bar{\phi}_t) \, d\mathbf{x} \\ &= \int_{\mathbb{R}^d} \left[\left(\frac{1}{2} \Delta \phi - V_d \phi - \beta_d |\phi|^2 \phi + \Omega L_z \phi \right) \bar{\phi} \right. \\ &\quad \left. + \frac{1}{2} \Delta \bar{\phi} - V_d \bar{\phi} - \beta_d |\phi|^2 \bar{\phi} - \Omega L_z \bar{\phi} \right) \phi \Big] \, d\mathbf{x} \\ &= -2 \left(E_{\beta, \Omega} + \frac{\beta_d}{2} \int_{\mathbb{R}^d} |\phi|^4 \, d\mathbf{x} \right) = -2\mu_{\beta, \Omega} < 0. \end{aligned}$$

(ii)

$$\begin{aligned} \frac{d}{dt} E_{\beta, \Omega} &= \int_{\mathbb{R}^d} \left[\left(\frac{1}{2} \nabla \phi_t \nabla \bar{\phi} + \frac{1}{2} \nabla \bar{\phi}_t \nabla \phi \right) + V_d (\phi_t \bar{\phi} + \bar{\phi}_t \phi) \right. \\ &\quad \left. + \beta_d |\phi|^2 (\bar{\phi}_t \phi + \phi \bar{\phi}_t) - \Omega L_z \phi_t \bar{\phi} - \bar{\phi}_t \Omega L_z \phi \right] \, d\mathbf{x} \end{aligned}$$

$$\begin{aligned}
&= \int_{\mathbb{R}^d} \left[\left(-\frac{1}{2} \Delta \phi + V_d \phi + \beta_d |\phi|^2 \phi - \Omega L_z \phi \right) \bar{\phi}_t \right. \\
&\quad \left. + \left(-\frac{1}{2} \Delta \bar{\phi} + V_d \bar{\phi} + \beta_d |\phi|^2 \bar{\phi} + \Omega L_z \bar{\phi} \right) \phi_t \right] d\mathbf{x} \\
&= - \int_{\mathbb{R}^d} (\bar{\phi}_t \phi_t + \phi_t \bar{\phi}_t) d\mathbf{x} = -2 \int_{\mathbb{R}^d} |\phi_t|^2 d\mathbf{x} < 0.
\end{aligned}$$

(iii) From (2.12) with $\psi = \tilde{\phi}$ and $\beta_d = 0$, (2.55), (2.57) and (2.58), integration by parts and the Schwartz inequality, we obtain

$$\begin{aligned}
\frac{d}{dt} E_{0,\Omega}(\tilde{\phi}) &= \frac{d}{dt} \int_{\mathbb{R}^d} \left[\frac{|\nabla \phi|^2}{2\|\phi\|^2} + \frac{V_d(\mathbf{x})|\phi|^2}{\|\phi\|^2} - \Omega \frac{\bar{\phi} L_z \phi}{\|\phi\|^2} \right] d\mathbf{x} \\
&= \int_{\mathbb{R}^d} \left[\frac{\nabla \bar{\phi} \cdot \nabla \phi_t + \nabla \phi \cdot \nabla \bar{\phi}_t}{2\|\phi\|^2} + \frac{V_d(\mathbf{x})(\bar{\phi} \phi_t + \phi \bar{\phi}_t)}{\|\phi\|^2} - \Omega \frac{\bar{\phi}_t L_z \phi + \bar{\phi} L_z \phi_t}{\|\phi\|^2} \right] d\mathbf{x} \\
&\quad - \left(\frac{d}{dt} \|\phi\|^2 \right) \int_{\mathbb{R}^d} \left[\frac{|\nabla \phi|^2}{2\|\phi\|^4} + \frac{V_d(\mathbf{x})|\phi|^2}{\|\phi\|^4} - \Omega \frac{\bar{\phi} L_z \phi}{\|\phi\|^4} \right] d\mathbf{x} \\
&= \int_{\mathbb{R}^d} \frac{\left[-\frac{1}{2} \Delta \phi + V_d(\mathbf{x})\phi - \Omega L_z \phi \right] \bar{\phi}_t + \left[-\frac{1}{2} \Delta \bar{\phi} + V_d(\mathbf{x})\bar{\phi} - \Omega L_z^* \bar{\phi} \right] \phi_t}{\|\phi\|^2} d\mathbf{x} \\
&\quad - \left(\frac{d}{dt} \|\phi\|^2 \right) \int_{\mathbb{R}^d} \frac{\frac{1}{2} |\nabla \phi|^2 + V_d(\mathbf{x})|\phi|^2 - \Omega \bar{\phi} L_z \phi}{\|\phi\|^4} d\mathbf{x} \\
&= -2 \frac{\|\phi_t\|^2}{\|\phi\|^2} + \frac{1}{2\|\phi\|^4} \left(\frac{d}{dt} \|\phi\|^2 \right)^2 \\
&= \frac{1}{2\|\phi\|^4} \left[\left(\int_{\mathbb{R}^d} (\bar{\phi} \phi_t + \phi \bar{\phi}_t) d\mathbf{x} \right)^2 - 4\|\phi\|^2 \|\phi_t\|^2 \right] \\
&\leq 0, \quad t_n \leq t \leq t_{n+1}. \tag{2.61}
\end{aligned}$$

This implies (2.60).

From Lemma 2.3.1, we get immediately

Theorem 2.3.1 *Suppose $V_d(\mathbf{x}) \geq 0$ for all $\mathbf{x} \in \mathbb{R}^d$ and $\|\phi_0\| = 1$. For $\beta_d = 0$, GFDN (2.55)-(2.57) is energy diminishing for any time step k and initial data ϕ_0 , i.e.*

$$E_{0,\Omega}(\phi(\cdot, t_{n+1})) \leq E_{0,\Omega}(\phi(\cdot, t_n)) \leq \cdots \leq E_{0,\Omega}(\phi(\cdot, 0)) = E_{0,\Omega}(\phi_0), \quad n = 0, 1, 2, \dots \tag{2.62}$$

2.3.3 Continuous normalized gradient flow (CNGF)

In fact, the normalized step (2.56) is equivalent to solve the following ODE *exactly*

$$\phi_t(\mathbf{x}, t) = \mu_\phi(t, k)\phi(\mathbf{x}, t), \quad \mathbf{x} \in \mathbb{R}^d, \quad t_n < t < t_{n+1}, \quad n \geq 0, \quad (2.63)$$

$$\phi(\mathbf{x}, t_n^+) = \phi(\mathbf{x}, t_{n+1}^-), \quad \mathbf{x} \in \mathbb{R}^d; \quad (2.64)$$

where

$$\mu_\phi(t, k) \equiv \mu_\phi(t_{n+1}, \Delta t_n) = -\frac{1}{2 \Delta t_n} \ln \|\phi(\cdot, t_{n+1}^-)\|^2, \quad t_n \leq t \leq t_{n+1}. \quad (2.65)$$

Thus the GFDN (2.55)-(2.57) can be viewed as a first-order splitting method for the gradient flow with discontinuous coefficients:

$$\phi_t = \frac{1}{2} \Delta \phi - V_d(\mathbf{x})\phi - \beta_d |\phi|^2 \phi + \Omega L_z \phi + \mu_\phi(t, k)\phi, \quad \mathbf{x} \in \mathbb{R}^d, \quad t \geq 0, \quad (2.66)$$

$$\phi(\mathbf{x}, 0) = \phi_0(\mathbf{x}), \quad \mathbf{x} \in \mathbb{R}^d \quad \text{with} \quad \|\phi_0\| = 1. \quad (2.67)$$

Letting $k \rightarrow 0$ and noticing that $\phi(\mathbf{x}, t_{n+1})$ on the right hand side of (2.64) is the solution of (2.55) at $t_{n+1} = t + \Delta t_n$, we obtain

$$\begin{aligned} \mu_\phi(t) &:= \lim_{k \rightarrow 0^+} \mu_\phi(t, k) = \lim_{\Delta t_n \rightarrow 0^+} \frac{1}{-2 \Delta t_n} \ln \|\phi(\cdot, t_{n+1}^-)\|^2 \\ &= \lim_{\Delta t_n \rightarrow 0^+} \frac{1}{-2 \Delta t_n} \ln \|\phi(\cdot, (t + \Delta t_n)^-)\|^2 = \lim_{\Delta t_n \rightarrow 0^+} \frac{\frac{d}{d\tau} \|\phi(\cdot, t + \tau)\|^2 \Big|_{\tau=\Delta t_n}}{-2 \|\phi(\cdot, t + \Delta t_n)\|^2} \\ &= \lim_{\Delta t_n \rightarrow 0^+} \frac{\mu_{\beta, \Omega}(\phi(\cdot, t + \Delta t_n))}{\|\phi(\cdot, t + \Delta t_n)\|^2} = \frac{\mu_{\beta, \Omega}(\phi(\cdot, t))}{\|\phi(\cdot, t)\|^2}. \end{aligned} \quad (2.68)$$

This suggests us to consider the following continuous normalized gradient flow:

$$\phi_t = \frac{1}{2} \Delta \phi - V_d(\mathbf{x})\phi - \beta_d |\phi|^2 \phi + \Omega L_z \phi + \mu_\phi(t)\phi, \quad \mathbf{x} \in \mathbb{R}^d, \quad t \geq 0, \quad (2.69)$$

$$\phi(\mathbf{x}, 0) = \phi_0(\mathbf{x}), \quad \mathbf{x} \in \mathbb{R}^d \quad \text{with} \quad \|\phi_0\| = 1. \quad (2.70)$$

In fact, the right hand side of (2.69) is the same as (2.14) if we view $\mu_\phi(t)$ as a Lagrange multiplier for the constraint (2.15). Furthermore for the above CNGF, as observed in [8] for non-rotating BEC, the solution of (2.69) also satisfies the following theorem:

Theorem 2.3.2 *Suppose $V_d(\mathbf{x}) \geq 0$ for all $\mathbf{x} \in \mathbb{R}^d$, $\beta_d \geq 0$ and $\|\phi_0\| = 1$. Then the CNGF (2.69)-(2.70) is normalization conserving and energy diminishing, i.e.*

$$\|\phi(\cdot, t)\|^2 = \int_{\mathbb{R}^d} |\phi(\mathbf{x}, t)|^2 d\mathbf{x} = \|\phi_0\|^2 = 1, \quad t \geq 0, \quad (2.71)$$

$$\frac{d}{dt} E_{\beta, \Omega}(\phi) = -2 \|\phi_t(\cdot, t)\|^2 \leq 0, \quad t \geq 0, \quad (2.72)$$

which in turn implies

$$E_{\beta, \Omega}(\phi(\cdot, t_1)) \geq E_{\beta, \Omega}(\phi(\cdot, t_2)), \quad 0 \leq t_1 \leq t_2 < \infty.$$

Proof

(i)

$$\begin{aligned} \frac{d}{dt} \|\phi\|^2 &= \frac{d}{dt} \int_{\mathbb{R}^d} \phi \bar{\phi} d\mathbf{x} = \int_{\mathbb{R}^d} \phi \bar{\phi}_t + \bar{\phi} \frac{\partial \phi}{\partial t} d\mathbf{x} \\ &= \int_{\mathbb{R}^d} \bar{\phi} \left[\frac{1}{2} \Delta \phi - V_d(\mathbf{x}) \phi - \beta_d |\phi|^2 \phi + \Omega L_z \phi + \mu_\phi(t) \phi \right] d\mathbf{x} \\ &\quad + \int_{\mathbb{R}^d} \phi \left[\frac{1}{2} \Delta \bar{\phi} - V_d(\mathbf{x}) \bar{\phi} - \beta_d |\phi|^2 \bar{\phi} + \Omega L_z \bar{\phi} + \mu_\phi(t) \bar{\phi} \right] d\mathbf{x} \\ &= -2 \int_{\mathbb{R}^d} \left[\frac{1}{2} |\nabla \phi|^2 + V_d(\mathbf{x}) |\phi|^2 + \beta_d |\phi|^4 - \Omega \bar{\phi} L_z \phi \right] d\mathbf{x} \\ &\quad + 2\mu_\phi(t) \cdot \|\phi(\cdot, t)\|^2 \\ &= 0, \end{aligned}$$

where $0 \leq t < \infty$. This implies the result in (2.71).

(ii)

$$\begin{aligned} \frac{d}{dt} E_{\beta, \Omega}(\phi) &= \int_{\mathbb{R}^d} \frac{1}{2} \left[\nabla \phi \nabla \bar{\phi}_t + \nabla \bar{\phi} \nabla \phi_t \right] d\mathbf{x} + \\ &\quad \int_{\mathbb{R}^d} \left[(\bar{\phi}_t \phi + \phi_t \bar{\phi}) (V_d(\mathbf{x}) + 2\beta_d |\phi|^2 + \mu_\phi(t)) - \Omega (\bar{\phi}_t L_z \phi + \bar{\phi} L_z \frac{\partial \phi}{\partial t}) \right] d\mathbf{x} \\ &= - \int_{\mathbb{R}^d} \phi_t \left[\frac{1}{2} \Delta \bar{\phi} - V_d(\mathbf{x}) \bar{\phi} - \beta_d |\phi|^2 \bar{\phi} - \Omega L_z \bar{\phi} + \mu_\phi(t) \bar{\phi} \right] d\mathbf{x} \\ &\quad - \int_{\mathbb{R}^d} \bar{\phi}_t \left[\frac{1}{2} \Delta \phi - V_d(\mathbf{x}) \phi - \beta_d |\phi|^2 \phi - \Omega L_z \phi + \mu_\phi(t) \phi \right] d\mathbf{x} \\ &= -2 \int_{\mathbb{R}^d} \left[\left| \frac{\partial \phi}{\partial t} \right|^2 \right] d\mathbf{x} \leq 0, \quad 0 \leq t < \infty. \end{aligned}$$

This implies the result in (2.72).

From this theorem and the inequality (2.27), we may also get as $t \rightarrow \infty$, when $|\Omega| < \gamma_{xy}$, ϕ approaches to a steady state solution which is a critical point of the energy functional $E_{\beta,\Omega}(\phi)$ [8, 121]. In non-rotating BEC, i.e. $\Omega = 0$, the unique real valued nonnegative ground state solution $\phi_g(\mathbf{x}) \geq 0$ for all $\mathbf{x} \in \mathbb{R}^d$ [83] is obtained by choosing a positive initial datum $\phi_0(\mathbf{x}) \geq 0$ for $\mathbf{x} \in \mathbb{R}^d$, e.g. the ground state solution of linear Schrödinger equation with a harmonic oscillator potential [8]. For rotating BEC, e.g. $|\Omega| < \gamma_{xy}$, our numerical results in section 2.4 suggest that the initial data can be chosen as a linear combination of the ground state and central vortex ground state of (2.10) when $\beta_d = 0$ and $\Omega = 0$, which are given explicitly in sections 2.2.2&2.2.4.

With this kind of initial data, the ground state solution $\phi_{\beta,\Omega}^g$ and its corresponding chemical potential $\mu_{\beta,\Omega}^g$ can be obtained from the steady state solution of the CNGF (2.69)-(2.70), i.e.

$$\phi^g(\mathbf{x}) := \phi_{\beta,\Omega}^g(\mathbf{x}) = \lim_{t \rightarrow \infty} \phi(\mathbf{x}, t), \quad \mathbf{x} \in \mathbb{R}^d, \quad \mu^g := \mu_{\beta,\Omega}^g = \mu_{\beta,\Omega}(\phi_{\beta,\Omega}^g). \quad (2.73)$$

Furthermore, when $\gamma_x = \gamma_y = 1$ in (2.10), our numerical results also suggest that when the initial data is chosen as the central vortex ground state of (2.10) with $\beta_d = 0$ and $\Omega = 0$, the steady state solution of the CNGF (2.69)-(2.70) converges to the central vortex ground state solution $\phi_{\beta,\Omega}^v$ as $t \rightarrow \infty$, i.e.

$$\phi^v(\mathbf{x}) := \phi_{\beta,\Omega}^v(\mathbf{x}) = \lim_{t \rightarrow \infty} \phi(\mathbf{x}, t), \quad \mathbf{x} \in \mathbb{R}^d, \quad \mu^v := \mu_{\beta,\Omega}^v = \mu_{\beta,\Omega}(\phi_{\beta,\Omega}^v) \quad (2.74)$$

Rigorous mathematical justification for these observations is under further study.

2.3.4 Fully numerical discretization

We now present a numerical method to discretize the GFDN (2.55)-(2.57). For simplicity of notation we introduce the method for the case of 2D over a rectangle $\Omega_{\mathbf{x}} = [a, b] \times [c, d]$ with homogeneous Dirichlet boundary conditions. Generalizations to 3D are straightforward for tensor product grids and the results remain valid without modifications.

We choose the spatial mesh sizes $h_x = \Delta x > 0$, $h_y = \Delta y > 0$ with $h_x = (b-a)/M$, $h_y = (d-c)/N$ and M, N even positive integers, the time step is given by $k = \Delta t > 0$ and define grid points and time steps by

$$\begin{aligned} x_j &:= a + j h_x, & j &= 0, 1, \dots, M, & y_l &= c + l h_y, & l &= 0, 1, \dots, N, \\ t_n &:= n k, & n &= 0, 1, 2, \dots \end{aligned}$$

Let $\phi_{j,l}^n$ be the numerical approximation of $\phi(x_j, y_l, t_n)$ and ϕ^n the solution vector at time $t = t_n = nk$ with components $\phi_{j,l}^n$.

We use backward Euler for time discretization and second-order centered finite difference for spatial derivatives. The detail scheme is:

$$\begin{aligned} \frac{\tilde{\phi}_{j,l} - \phi_{j,l}^n}{k} &= \frac{1}{2h_x^2} [\tilde{\phi}_{j+1,l} - 2\tilde{\phi}_{j,l} + \tilde{\phi}_{j-1,l}] + \frac{1}{2h_y^2} [\tilde{\phi}_{j,l+1} - 2\tilde{\phi}_{j,l} + \tilde{\phi}_{j,l-1}] \\ &\quad - V_2(x_j, y_l) \tilde{\phi}_{j,l} - \beta_2 |\phi_{j,l}^n|^2 \tilde{\phi}_{j,l} + i\Omega y_l \frac{\tilde{\phi}_{j+1,l} - \tilde{\phi}_{j-1,l}}{2h_x} - i\Omega x_j \frac{\tilde{\phi}_{j,l+1} - \tilde{\phi}_{j,l-1}}{2h_y}, \\ &\quad j = 1, \dots, M-1, \quad l = 1, \dots, N-1, \\ \tilde{\phi}_{0,l} &= \tilde{\phi}_{M,l} = \tilde{\phi}_{j,0} = \tilde{\phi}_{j,N} = 0, \quad j = 0, \dots, M, \quad l = 0, \dots, N, \\ \phi_{j,l}^{n+1} &= \frac{\tilde{\phi}_{j,l}}{\|\tilde{\phi}\|}, \quad j = 0, 1, \dots, M, \quad l = 0, \dots, N, \quad n = 0, 1, \dots, \\ \phi_{j,l}^0 &= \phi_0(x_j, y_l), \quad j = 0, 1, \dots, M; \quad l = 0, \dots, N, \end{aligned} \tag{2.75}$$

where the norm is defined as $\|\tilde{\phi}\|^2 = h_x h_y \sum_{j=1}^{M-1} \sum_{l=1}^{N-1} |\tilde{\phi}_{j,l}|^2$.

2.4 Numerical results

In this section, we will show how to choose initial data for computing the ground state of a rotating BEC, and present numerical results for ground states, symmetric states, central vortex states and central vortex ground states, as well as their energy diagrams in 2D and 3D. Furthermore, we also study numerically dimension reduction from 3D to 2D, errors between ground state and its Thomas-Fermi approximation and critical angular speed. Due to lemma 2.2.1, theorem 2.2.1, we only present results for $0 \leq \Omega < \gamma_{xy}$. In all computations, $\gamma_x = 1$, the bounded computational

domain $\Omega_{\mathbf{x}}$ is chosen as a rectangle in 2D and a box in 3D, which is centered at the origin.

2.4.1 Initial data for computing ground state

For computing ground state of rotating BEC, as discussed in section 2.3, the GFDN and its BEFD discretization guarantees energy diminishing. For $|\Omega| \ll 1$, i.e. slowly rotating BEC, the initial data can be chosen as the ground state of (2.10) with $\beta_d = 0$ and $\Omega = 0$ (2.40), which is given explicitly by (2.40). When Ω increases, the ground state may break symmetry. From our primary numerical study, when Ω is near γ_{xy} , the above choice no longer gives the ground state. Here we present a two-dimensional example to evolve the GFDN (2.55) with its BEFD discretization for four different initial data.

Example 2.1 Different choices of initial data for GFDN in 2D, i.e. we choose $d = 2$, $\gamma_y = 1$ and $\beta_2 = 100$ in (2.55). We compute numerically the steady state solution of (2.55) under the BEFD discretization with a bounded computational domain $\Omega_{\mathbf{x}} = [-6, 6] \times [-6, 6]$ and four different initial data:

- I. $\phi_0(x, y) = \phi_{\text{ho}}^v(x, y) = \frac{x+iy}{\sqrt{\pi}} e^{-(x^2+y^2)/2}$, $(x, y) \in \Omega_{\mathbf{x}}$,
- II. $\phi_0(x, y) = \phi_{\text{ho}}(x, y) = \frac{1}{\sqrt{\pi}} e^{-(x^2+y^2)/2}$, $(x, y) \in \Omega_{\mathbf{x}}$,
- III. $\phi_0(x, y) = \frac{[\phi_{\text{ho}}(x, y) + \phi_{\text{ho}}^v(x, y)]/2}{\|[\phi_{\text{ho}}(x, y) + \phi_{\text{ho}}^v(x, y)]/2\|}$, $(x, y) \in \Omega_{\mathbf{x}}$,
- IV. $\phi_0(x, y) = \frac{(1 - \Omega)\phi_{\text{ho}}(x, y) + \Omega\phi_{\text{ho}}^v(x, y)}{\|(1 - \Omega)\phi_{\text{ho}}(x, y) + \Omega\phi_{\text{ho}}^v(x, y)\|}$, $(x, y) \in \Omega_{\mathbf{x}}$.

The steady state solution is obtained numerically when $\max_{j,l} |\phi_{j,l}^{n+1} - \phi_{j,l}^n| < \epsilon = 10^{-7}$. Table 2.1 shows the energy of the steady state solutions with the four different initial data for $0 \leq \Omega < 1$ and $\beta_2 = 10, 100$ and 400 .

From Table 2.1 and our additional numerical experiments, we have the following observation: (i) Type IV initial data gives the ground state for all $|\Omega| < \gamma_{xy} = 1$, (ii) Types II& III initial data only give the ground state when $|\Omega|$ is near 0, (iii) Type I initial data only gives the ground state when $|\Omega|$ is less than but very near $\gamma_{xy} = 1$.

	Ω	case I	case II	case III	case IV
$\beta_2 = 10$	0.0	2.3563	1.5914	1.5914	1.59141
	0.25	2.1068	1.5914	1.5914	1.5914
	0.50	1.8572	1.5914	1.5914	1.5914
	0.75	1.6077	1.5914	1.6078	1.5914
	0.80	1.5578	1.5914	1.5578	1.5578
	0.90	1.4580	1.4716	1.4580	1.4580
$\beta_2 = 100$	0.00	4.3585	3.945	3.945	3.945
	0.25	4.1096	3.9456	3.945	3.945
	0.50	3.8608	3.9456	3.8608	3.8608
	0.75	3.3713	3.3750	3.3802	3.3750
	0.80	3.2032	3.1980	3.1817	3.1817
	0.90	2.6535	2.6573	2.6483	2.6420
$\beta_2 = 400$	0.0	7.8995	7.6328	7.6496	7.6328
	0.25	7.6496	7.6328	7.6328	7.6328
	0.50	7.3998	7.6328	7.2426	7.2426
	0.75	5.9993	5.9678	5.9604	5.9603
	0.80	5.5697	5.6026	5.5481	5.5479
	0.90	4.5447	4.4651	4.4563	4.4563

Table 2.1: Energy of the steady state solutions of the GFDN (2.55) under the BEFD discretization with four different initial data.

From this numerical study for computing ground state, when $\gamma_y = 1$, we suggest choosing the following initial data in (2.56) for the GFDN (2.55) with its BEFD discretization:

$$\phi_0(\mathbf{x}) = \frac{(1 - \Omega)\phi_{\text{ho}}(\mathbf{x}) + \Omega\phi_{\text{ho}}^v(\mathbf{x})}{\|(1 - \Omega)\phi_{\text{ho}}(\mathbf{x}) + \Omega\phi_{\text{ho}}^v(\mathbf{x})\|}, \quad \mathbf{x} \in \mathbb{R}^d, \quad (2.76)$$

where

$$\phi_{\text{ho}}(\mathbf{x}) = \begin{cases} \frac{1}{\sqrt{\pi}} e^{-(x^2+y^2)/2}, \\ \frac{\gamma_z^{1/4}}{\pi^{3/4}} e^{-(x^2+y^2+\gamma_z z^2)/2}, \end{cases} \quad \phi_{\text{ho}}^v(\mathbf{x}) = \begin{cases} \frac{1}{\sqrt{\pi}} (x+iy) e^{-(x^2+y^2)/2} & d=2, \\ \frac{\gamma_z^{1/4}}{\pi^{3/4}} (x+iy) e^{-(x^2+y^2+\gamma_z z^2)/2} & d=3. \end{cases}$$

Under this choice of initial data, the continuation technique is no longer required for computing the ground state. Furthermore, from our numerical study, the initial data for computing the central vortex ground state can be chosen as

$$\phi_0(\mathbf{x}) = \phi_{\text{ho}}^v(\mathbf{x}), \quad \mathbf{x} \in \mathbb{R}^d.$$

2.4.2 Results in 2D

Example 2.2 For ground state, symmetric state and central vortex states, as well as their energy configurations, in 2D, i.e., we take $d = 2$ and $\gamma_y = 1$ in (2.55). Figure 2.1 plots surface and contour of the ground state $\phi^g(x, y) := \phi_{\beta, \Omega}^g(x, y)$ with $\beta_2 = 100$ for different Ω and Figure 2.2 for central vortex ground state $\phi^v(x, y) := \phi_{\beta, \Omega}^v(x, y)$. Figure 2.3 plots the symmetric state $\phi^0(r) := \phi_{\beta, 0}^0(r)$ and first three central vortex states $\phi^m(r) := \phi_{\beta, 0}^m(r)$ ($m = 1, 2, 3$) for different interaction rate β_2 . Table 2.2 and Figure 2.4 show the energy configurations of these states for different β_2 and Ω .

Furthermore, Figure 2.5 shows ratios between the energy of these states, and Figure 2.6 plots the energy of the ground state when $\beta_2 \gg 1$ and $\Omega \approx \gamma_{xy} = 1$. Similar study for the ground state and its energy diagram has been done in [4].

From Figures 2.1-2.4 and Table 2.2, we reach the following conjectures for rotating BEC under an isotropic trap in 2D, i.e. $\gamma_y = 1$: (a) For any fixed $\beta_2 > 0$, there exists a critical angular frequency $0 < \Omega^c < \gamma_{xy} = 1$ such that:

- (i) when $0 \leq \Omega < \Omega^c$, the ground state $\phi_{\beta, \Omega}^g = \phi_{\beta, 0}^g = \phi_{\beta, 0}^0$, $E_{\beta, \Omega}^g = E_{\beta, 0}^g = E_{\beta, 0}^0$ and $\mu_{\beta, \Omega}^g = \mu_{\beta, 0}^g = \mu_{\beta, 0}^0$;
- (ii) when $\Omega = \Omega^c$, the ground state is not unique, e.g. both $\phi_{\beta, 0}^0$ and $\phi_{\beta, 0}^1$ are ground states, i.e. $E_{\beta, \Omega^c}^g = E_{\beta, 0}^0 = E_{\beta, \Omega^c}^1$ and $\mu_{\beta, \Omega^c}^g = \mu_{\beta, 0}^0 = \mu_{\beta, \Omega^c}^1$;
- (iii) when $\Omega^c < \Omega < \gamma_{xy} = 1$, quantized vortices appear in the ground states,

	β	$E_{\beta,\Omega}^g$	$E_{\beta,\Omega}^0$	$E_{\beta,\Omega}^v$	$E_{\beta,\Omega}^1$	$E_{\beta,\Omega}^2$	$E_{\beta,\Omega}^3$
$\Omega = 0.0$	0	0.997	0.999	1.993	1.999	2.999	3.999
	10.0	1.591	1.592	2.356	2.361	3.280	4.237
	100.0	3.945	3.945	4.358	4.368	5.040	5.821
	1000.0	11.970	11.971	12.151	12.166	12.544	13.039
$\Omega = 0.50$	0.0	0.997	0.999	1.494	1.499	1.999	2.499
	10.0	1.591	1.592	1.857	1.861	2.280	2.737
	100.0	3.860	3.945	3.860	3.868	4.040	4.321
	1000.0	11.026	11.971	11.021	11.366	11.544	11.539
$\Omega = 0.75$	0	0.997	0.999	1.245	1.249	1.499	1.749
	10.0	1.591	1.592	1.608	1.611	1.780	1.987
	100.0	3.375	3.945	3.371	3.618	3.540	3.571
	1000.0	9.098	11.971	9.114	11.416	11.044	10.789
$\Omega = 0.90$	0	0.991	0.999	1.095	1.099	1.199	1.299
	10.0	1.449	1.592	1.458	1.461	1.480	1.537
	100.0	2.648	3.945	2.653	3.468	3.240	3.121
	1000.0	7.163	11.971	7.176	11.266	10.744	10.339

Table 2.2: Energy of the ground state $E_{\beta,\Omega}^g$, symmetric state $E_{\beta,\Omega}^0$, central vortex ground state $E_{\beta,\Omega}^v$ and the first three central vortex states $E_{\beta,\Omega}^j$ ($j = 1, 2, 3$) for different β_2 and Ω in 2D.

and the larger Ω is the more vortices appear in the ground state. Similar conclusion was observed in the literatures [4].

(b) Similar patterns for the central vortex ground state are observed as in (a) for the ground state.

(c) For any fixed $\beta_2 \geq 0$, when Ω increases from 0 to $\gamma_{xy} = 1$, the energy $E_{\beta,\Omega}^s$ and chemical potential $\mu_{\beta,\Omega}^s$ ($s = g, v, 0, 1, \dots$) of any stationary states decrease. Furthermore, the energy of the ground state has the following asymptotics when Ω

is near $\gamma_{xy} = 1$ (cf. Fig. 6.6b):

$$E_{\beta,\Omega}^g = E_{\beta,\pm\gamma_{xy}^\mp}^g + O(\gamma_{xy} \mp \Omega), \quad \Omega \rightarrow \pm\gamma_{xy}^\mp.$$

(d) For any fixed $|\Omega| < \gamma_{xy} = 1$, when β_2 increases, the energy $E_{\beta,\Omega}^s$ and chemical potential $\mu_{\beta,\Omega}^s$ ($s = g, v, 0, 1, \dots$) of any stationary states increase too, and satisfy

$$\lim_{\beta_2 \rightarrow \infty} \frac{E_{\beta,\Omega}^v}{E_{\beta,\Omega}^g} = \lim_{\beta_2 \rightarrow \infty} \frac{\mu_{\beta,\Omega}^v}{\mu_{\beta,\Omega}^g} = 1, \quad \lim_{\beta_2 \rightarrow \infty} \frac{E_{\beta,\Omega}^s}{E_{\beta,\Omega}^g} = \text{const}, \quad \lim_{\beta_2 \rightarrow \infty} \frac{\mu_{\beta,\Omega}^s}{\mu_{\beta,\Omega}^g} = \text{const}, \quad s \geq 0,$$

$$E_{\beta,\Omega}^s = O(\beta_2^{1/2}), \quad \mu_{\beta,\Omega}^s = O(\beta_2^{1/2}), \quad \text{when } \beta_2 \rightarrow \infty, \quad s = g, v, 0, 1, \dots .$$

Example 2.3 Ground state in 2D with a nonsymmetric trap, i.e., we take $d = 2$ and $\gamma_y = 1.5$ in (2.55). Figure 2.7 plots surface and contour of the ground state $\phi^g(x, y)$ with $\beta_2 = 100$ for different Ω .

From Figure 2.7, the conjecture (a) for ground states in Example 2.2 is still valid for an anisotropic trap, i.e. $\gamma_y > 1$, in 2D.

Example 2.4 Ground state in 2D with a symmetric trap plus quadratic trap, i.e., we take $d = 2$ and $V_2(x, y) = \frac{1}{2}(x^2 + y^2) + \frac{\tau}{2}(x^2 + y^2)^2$ in (2.55). Figure 2.8 plots the image of the ground state $\phi^g(x, y)$ with $\beta_2 = 100$ for different Ω . From Figure 2.8, we find that we may generate the giant vortex in the ground state, these numerical results also agree well with those presented in [51].

2.4.3 Results in 3D

Example 2.5 Ground state, symmetric state and central vortex states, as well as their energy configurations, in 3D, i.e. we take $d = 3$, $\gamma_y = 1$ and $\gamma_z = 1$ in (2.55). Figure 2.9 plots isosurface of the ground state $\phi^g(x, y, z) := \phi_{\beta,\Omega}^g(x, y, z)$ with $\beta = 100$ for different Ω . Figure 2.10 plots symmetric state $\phi^0(r, z = 0)$, $\phi^0(r = 0, z)$, and the first central vortex state $\phi^1(r, z = 0)$, $\phi^1(r = 0, z)$ for different interaction rate β . Figure 2.11 shows the energy configurations of these states for different β and Ω in 3D.

β_2	0	10	100	1000
$\Omega^c (\approx E_{\beta,0}^1 - E_{\beta,0}^0)$	1.0 (1.0)	0.775 (0.769)	0.406 (0.423)	0.188 (0.195)
$\Omega^v (\approx E_{\beta,0}^2 - E_{\beta,0}^1)$	1.0 (1.006)	0.87 (0.924)	0.625 (0.682)	0.375 (0.393)

Table 2.3: Critical angular velocities in 2D.

From Figures 2.9-2.11, all the conjectures at Example 2 are still valid in 3D except that (2.77) should be modified to

$$E_{\beta,\Omega}^s = O(\beta^{2/5}), \quad \mu_{\beta,\Omega}^s = O(\beta^{2/5}), \quad \text{when } \beta \rightarrow \infty, \quad s = g, v, 0, 1, \dots \quad (2.77)$$

For obtaining bending vortex, e.g. S-shaped vortex and U-shaped vortex, in 3D with a prolate trap, we refer to [4, 6, 54, 96].

2.4.4 Critical angular velocity

Example 2.6 Critical angular velocities in 2D, i.e. we take $d = 2$ and $\gamma_y = 1$ in (2.55). Table 2.3 displays the critical angular velocity $\Omega^c := \Omega_\beta^c$ and $\Omega^v := \Omega_\beta^v$ for different β_2 .

From Table 2.3, we get: (a) $\Omega^c = \Omega^v = 1.0$ when $\beta_2 = 0$ and $0 < \Omega^c < \Omega^v < 1$ when $\beta_2 > 0$; (b) Ω^c and Ω^v decrease when β_2 increases; (c) $\Omega^c \approx E_{\beta,0}^1 - E_{\beta,0}^0$ and $\Omega^v = E_{\beta,0}^2 - E_{\beta,0}^1$ for $\beta_2 \geq 0$. All these results agree very well with the numerical results [55] and analytically estimate [118, 119] in the literature. Similar observations are still valid in 3D.

2.4.5 Numerical verification for dimension reduction

As we know, when $\gamma_y = O(1)$ and $\gamma_z \gg 1$, the three-dimensional GPE can be reduced to a two-dimensional GPE. Here we present a numerical verification of this procedure. In order to do so, we find the ground state $\phi_g^{3D}(x, y, z)$ of the three-dimensional GPE, i.e. we take $d = 3$, $\gamma_y = 1$ and $\beta = 100$ in (2.55), numerically for

$1/\gamma_z$	1/4	1/8	1/16
$\beta_2^{\text{ex}} - \beta_2$	-10.762	-9.803	-8.830
$\max \phi^3 - \phi_{\text{ho}}^3 $	0.084	0.0637	0.048
$\ \phi^3 - \phi_{\text{ho}}^3\ _{l^2}$	0.097	0.0603	0.038
$\max \phi_g^{3\text{D}} - \phi_g^{2\text{D}} \phi_{\text{ho}}^3 $	0.083	0.4606	0.015
$\ \phi_g^{3\text{D}} - \phi_g^{2\text{D}} \phi_{\text{ho}}^3\ _{l^2}$	0.260	1.3836	0.047

Table 2.4: Numerical verification of dimension reduction from 3D to 2D.

different γ_z . Then we compute

$$\phi^3(z) = \sqrt{\int_{\mathbb{R}^2} |\phi_g^{3\text{D}}(x, y, z)|^2 dx dy} \approx \phi_{\text{ho}}^3(z) = \frac{\gamma_z^{1/4}}{\pi^{1/4}} e^{-\gamma_z z^2/2},$$

$$\beta_2^{\text{ex}} = \beta \int_{-\infty}^{\infty} |\phi^3(z)|^4 dz \approx \beta_2 = \beta \sqrt{\gamma_z/2\pi}.$$

We also find the ground state $\phi_g^{2\text{D}}(x, y)$ of the two-dimensional GPE, i.e. we take $d = 2$, $\gamma_y = 1$ and $\beta_2 = 100\sqrt{\gamma_z/2\pi}$ in (2.55), numerically for different γ_z . Table 2.4 lists the errors of $\beta_2^{\text{ex}} - \beta_2$, $\max |\phi^3 - \phi_{\text{ho}}^3|$, $\|\phi^3 - \phi_{\text{ho}}^3\|_{l^2}$, $\max |\phi_g^{3\text{D}} - \phi_g^{2\text{D}} \phi_{\text{ho}}^3|$ and $\|\phi_g^{3\text{D}} - \phi_g^{2\text{D}} \phi_{\text{ho}}^3\|_{l^2}$ for different γ_z .

From Table 2.4, the dimension reduction of GPE from 3D to 2D when $\gamma_z \gg 1$ is verified numerically. Furthermore, for fixed $\beta > 0$, when $\gamma_z \rightarrow \infty$, we have the following convergence rate:

$$\frac{\beta_2 - \beta_2^a}{\beta_2} = O\left(\frac{\ln \gamma_z}{\gamma_z^{3/4}}\right), \quad \beta_2 = \beta \sqrt{\frac{\gamma_z}{2\pi}} \left(1 + O\left(\frac{\ln \gamma_z}{\gamma_z^{3/4}}\right)\right),$$

$$\|\phi_3 - \phi_{\text{ho}}\|_{L^\infty} = O\left(\frac{\ln \gamma_z}{\gamma_z^{1/2}}\right), \quad \|\phi_3 - \phi_{\text{ho}}\|_{L^2} = O\left(\frac{\ln \gamma_z}{\gamma_z^{3/4}}\right),$$

$$\|\phi_g^{3\text{D}} - \phi_g^{2\text{D}} \phi_{\text{ho}}\|_{L^\infty} = O\left(\frac{\ln \gamma_z}{\gamma_z^{5/8}}\right), \quad \|\phi_g^{3\text{D}} - \phi_g^{2\text{D}} \phi_{\text{ho}}\|_{L^2} = O\left(\frac{\ln \gamma_z}{\gamma_z^{3/4}}\right).$$

2.4.6 Errors of the TF approximation

As we know, when $\beta_d \gg 1$ and $|\Omega| \approx 0$, the ground state is very well approximated by the TF approximation [4, 5, 8, 10]. Here we study numerically how effective the

	β_2	$\Omega = 0$	$\Omega = 0.1$	$\Omega = 0.5$	$\Omega = 0.75$
$\max \left \phi_{\beta,\Omega}^g ^2 - \phi_{\beta}^{\text{TF}} ^2 \right $	100	3.827E-3	3.832E-3	5.641E-2	4.516E-2
	200	2.177E-3	2.181E-3	3.989E-2	3.966E-2
	400	1.2849E-3	1.288E-3	2.820E-2	2.657E-2
	800	7.125E-4	7.407E-4	1.358E-2	1.659E-2
	1000	6.157E-4	6.172E-4	1.161E-2	1.321E-2
$E_{\beta,\Omega}^g - E_{\beta,\Omega}^{\text{TF}}$	100	0.1167	0.117	9.879E-2	0.932
	200	8.950E-2	8.919E-2	0.190	1.652
	400	6.846E-2	6.811E-2	0.262	2.620
	800	7.858E-2	5.079E-2	1.325	3.748
	1000	4.684E-2	4.640E-2	1.586	4.243
$\mu_{\beta,\Omega}^g - \mu_{\beta,\Omega}^{\text{TF}}$	100	0.183	0.183	9.954E-2	0.402
	200	0.142	0.1423	2.520E-2	0.890
	400	0.110	0.109	0.128	1.568
	800	8.643E-2	8.342E-2	0.719	2.441
	1000	7.649E-2	7.650E-2	0.870	2.796

Table 2.5: Errors of the TF approximation in 2D.

TF approximation when $|\Omega|$ is large, especially when $|\Omega|$ is near 1. In order to do so, we compare the ground state and its TF approximation in 2D, i.e. we take $d = 2$ and $\gamma_y = 1$ in (2.55). Table 2.5 lists the errors $\max \left| |\phi_{\beta,\Omega}^g|^2 - |\phi_{\beta}^{\text{TF}}|^2 \right|$, $E_{\beta,\Omega}^g - E_{\beta,\Omega}^{\text{TF}}$ and $\mu_{\beta,\Omega}^g - \mu_{\beta,\Omega}^{\text{TF}}$ for different $\beta_2 \gg 1$ and Ω .

From Table 2.5, we can see that the density of the ground state converges to the TF approximation for any $|\Omega| < \gamma_{xy} = 1$ when $\beta_2 \rightarrow \infty$. However, when β_2 increases, the energy and chemical potential of the ground state converge to those of the TF approximation only when $|\Omega| \approx 0$, but diverge when $|\Omega|$ is near $\gamma_{xy} = 1$. This is due to the fact that more and more vortices appear in the ground state when $|\Omega|$ is near 1 and $\beta_2 \gg 1$. A similar conclusion is also valid in 3D based on our

additional numerical experiments.

2.4.7 Spurious numerical ground states when $|\Omega| \geq \gamma^{xy} = 1$

As discussed in section 2.2.2, for a rotating BEC, there exists a ground state when $|\Omega| < \gamma_{xy} = 1$ and no ground state when $|\Omega| > \gamma^{xy} = 1$. But when we evolve the discretization (2.75) with the initial data (2.76) numerically, for any given $\beta_2 \geq 0$ and $\Omega \in \mathbb{R}$, we always obtain a steady state $\phi_{\beta,\Omega}^h$ for a fixed mesh size $h \ll 1$. In fact, this steady state is the minimizer of the following finite-dimensional minimization problem:

$$E^h := \min_{\phi^h \in S^h} E_{\beta,\Omega}^h(\phi^h), \quad (2.78)$$

where $S^h = \{\phi^h \in C^{(M+1) \times (N+1)} \mid \|\phi^h\| = 1, \phi_{0,l}^h = \phi_{M,l}^h = \phi_{j,0}^h = \phi_{j,N}^h = 0, j = 0, \dots, M, l = 0, \dots, N\}$ and

$$\begin{aligned} E_{\beta,\Omega}^h(\phi^h) &:= \sum_{j=1}^{M-1} \sum_{l=1}^{N-1} \left[\frac{|\phi_{j+1,l}^h - \phi_{j-1,l}^h|^2}{(2h_x)^2} + \frac{|\phi_{j,l+1}^h - \phi_{j,l-1}^h|^2}{(2h_y)^2} + V_2(x_j, y_l) |\phi_{j,l}^h|^2 \right. \\ &\quad \left. + \frac{\beta_2}{2} |\phi_{j,l}^h|^4 + i\Omega(\phi^h)_{j,l}^* \left(y_l \frac{\phi_{j+1,l}^h - \phi_{j-1,l}^h}{2h_x} - x_j \frac{\phi_{j,l+1}^h - \phi_{j,l-1}^h}{2h_y} \right) \right] \\ &\approx E_{\beta,\Omega}(\phi). \end{aligned}$$

Table 2.6 lists the numerical energies E^h with $\beta_2 = 100$ for $\gamma_y = 1$ and $\gamma_x = 1.5$, under different rotation speeds Ω and mesh sizes h .

From Table 2.6, we can observe that for $\gamma_y \geq 1$: (i) When $|\Omega| < \gamma_{xy} = 1$, $E^g := \lim_{h \rightarrow 0} E^h$ which implies that $\phi_{\beta,\Omega}^h$ is a good approximation of the ground state $\phi_{\beta,\Omega}^g(\mathbf{x})$; (ii) when $|\Omega| > \gamma^{xy}$, $\lim_{h \rightarrow 0} E^h = -\infty$ which suggests that there is no ground state when $|\Omega| > \gamma^{xy}$ and the steady state solution ϕ^h is a spurious numerical ground state; (iii) when $\gamma_{xy} < |\Omega| \leq \gamma^{xy}$ in an anisotropic trap, our numerical results suggest that there is no ground state. Similar results can be obtained in 3D from our additional numerical experiments.

$\gamma_y = 1$	Ω	$h = 1/2$	$h = 1/4$	$h = 1/8$	$h = 1/16$
	0.0	3.937	3.944	3.945	3.945
	0.8	3.164	3.185	3.186	3.186
	1.0	2.402	1.952	1.598	1.388
	1.5	-1.744	-13.550	-37.952	-52.941
$\gamma_y = 1.5$	0.0	4.831	4.843	4.846	4.846
	0.8	4.294	4.289	4.285	4.285
	1.0	3.592	3.298	2.911	2.716
	1.5	-1.010	-5.130	-18.840	-27.461

Table 2.6: Energy E^h in 2D with $\beta_2 = 100$.

2.5 Conclusion

We have studied the ground state, symmetric state and central vortex states in rotating BEC analytically and numerically based on the Gross-Pitaevskii mean field theory. Existence and nonexistence of the ground state when the dimensionless angular velocity $|\Omega| < \gamma_{xy}$ and $|\Omega| > \gamma^{xy}$, respectively, is proven. Furthermore, based on our asymptotic and extensive numerical studies, we can draw the following conjectures for rotating BEC:

(i) The nonlinear eigenvalue problem (2.14) admits infinitely many eigenfunctions which are linearly independent. When $\beta_d \geq 0$ and $|\Omega| < \gamma_{xy}$, if the eigenfunctions of (2.14) are ranked according to their energies, ϕ^g, ϕ^1, \dots , then the corresponding eigenvalues (or chemical potentials) are in the same order, i.e.

$$E_{\beta,\Omega}(\phi^g) \leq E_{\beta,\Omega}(\phi^1) \leq E_{\beta,\Omega}(\phi^2) \leq \dots \implies \mu_{\beta,\Omega}(\phi^g) \leq \mu_{\beta,\Omega}(\phi^1) \leq \mu_{\beta,\Omega}(\phi^2) \leq \dots$$

(ii) For any fixed $\beta_d \geq 0$, there exists a critical angular frequency $0 < \Omega^c \leq \gamma_{xy}$ such that when $\Omega > \Omega^c$ the ground state breaks symmetry, i.e. quantized vortices appear in the ground state. When β_d increases, Ω^c increases too. Similar conclusions

are valid for central vortex ground states. Furthermore, we have

$$\Omega^c \approx E_{\beta,0}^1 - E_{\beta,0}^0, \quad \Omega^v \approx E_{\beta,0}^2 - E_{\beta,0}^1.$$

(iii) For any fixed $|\Omega| < \gamma_{xy}$, the energy and chemical potential of any stationary state increase when β_d increases. Furthermore, when $\beta_d \rightarrow \infty$, they have the following asymptotics:

$$E_{\beta,\Omega}^s = O(\beta^{2/(2+d)}), \quad \mu_{\beta,\Omega}^s = O(\beta^{2/(2+d)}), \quad \text{when } \beta \rightarrow \infty, \quad s = g, v, 0, 1, \dots,$$

and the ratios between them are constants, i.e.

$$\lim_{\beta_d \rightarrow \infty} \frac{E_{\beta,\Omega}^v}{E_{\beta,\Omega}^g} = \lim_{\beta_d \rightarrow \infty} \frac{\mu_{\beta,\Omega}^v}{\mu_{\beta,\Omega}^g} = 1, \quad \lim_{\beta_d \rightarrow \infty} \frac{E_{\beta,\Omega}^s}{E_{\beta,\Omega}^g} = \text{const}, \quad \lim_{\beta_d \rightarrow \infty} \frac{\mu_{\beta,\Omega}^s}{\mu_{\beta,\Omega}^g} = \text{const}, \quad s \geq 0.$$

(iv) For any fixed $\beta_d \geq 0$, the energy and chemical potential of any stationary state decrease when Ω increases from 0 to γ_{xy} or decreases from 0 to $-\gamma_{xy}$. Furthermore, the energy of the ground state has the following asymptotics when Ω is near $\pm\gamma_{xy}$:

$$E_{\beta,\Omega}^g = E_{\beta,\pm\gamma_{xy}^\mp}^g + O(\gamma_{xy} \mp \Omega), \quad \Omega \rightarrow \pm\gamma_{xy}^\mp.$$

(v) In disk-shaped condensation, i.e. $\gamma_x = O(1)$, $\gamma_y = O(1)$ and $\gamma_z \gg 1$, the ground state and its energy and chemical potential in 3D with interaction β can be well approximated by those of its two-dimensional reduction with interaction $\beta_2 = \beta\sqrt{\gamma_z/2\pi}$.

(vi) In the semiclassical regime, the TF approximation is very accurate for the density of the ground state except at the vortex core; where the TF approximate energy and chemical potential converge to the ground state energy and chemical potential respectively only when $|\Omega| \approx 0$, but diverge when $|\Omega|$ is near γ_{xy} .

In the next chapter, Chapter 3, we will use the obtained the ground state as the initial condition to investigate the dynamics of vortex lattice in the rotating BEC at extremely low temperature. In Chapter 4, we will extend the numerical method-GFDN to study the stationary states for rotating two-component BEC.

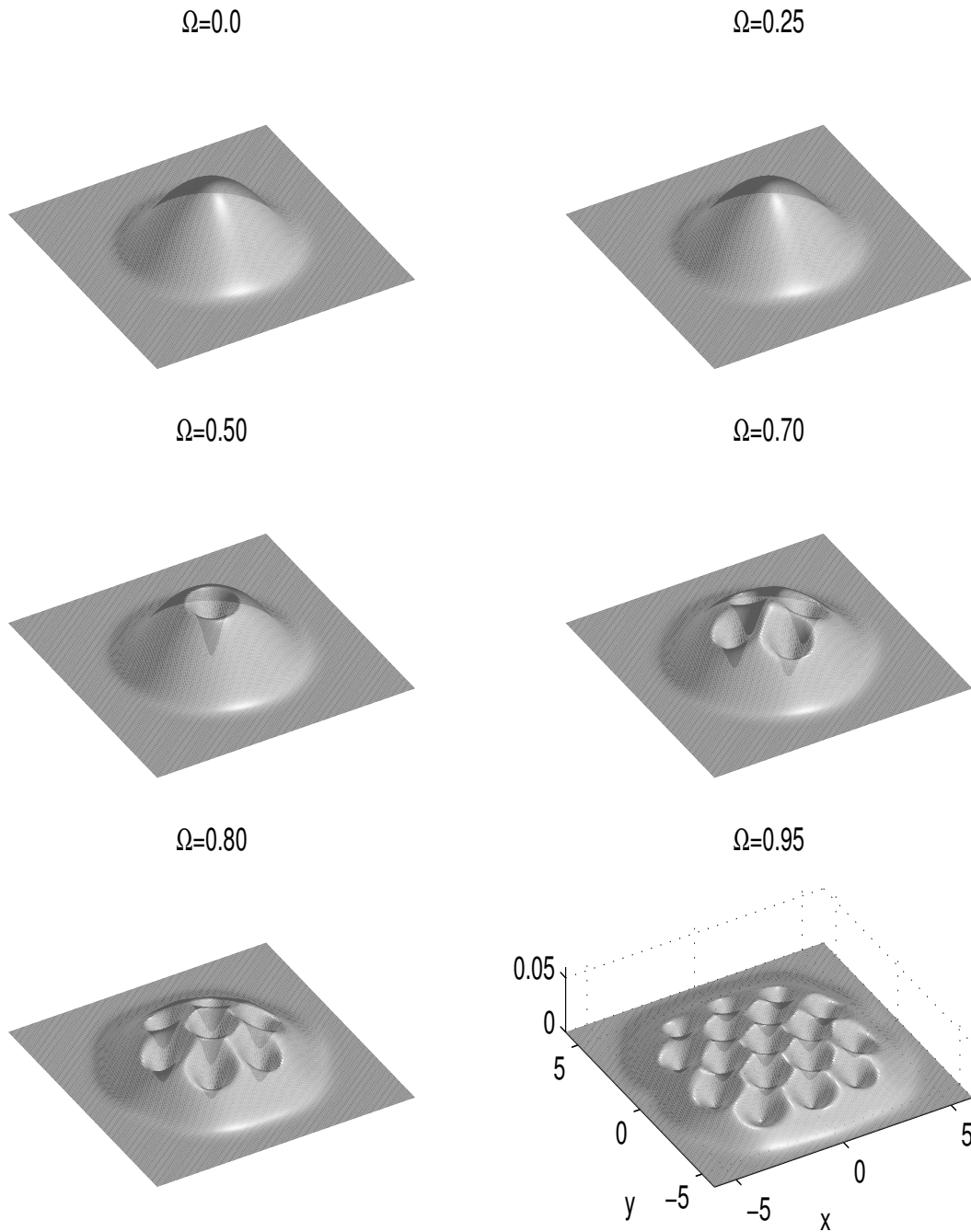


Figure 2.1: Surface plots of ground state density function $|\phi^g(x, y)|^2$ in 2D with $\gamma_y = 1$ and $\beta_2 = 100$ for different Ω in Example 2.2.

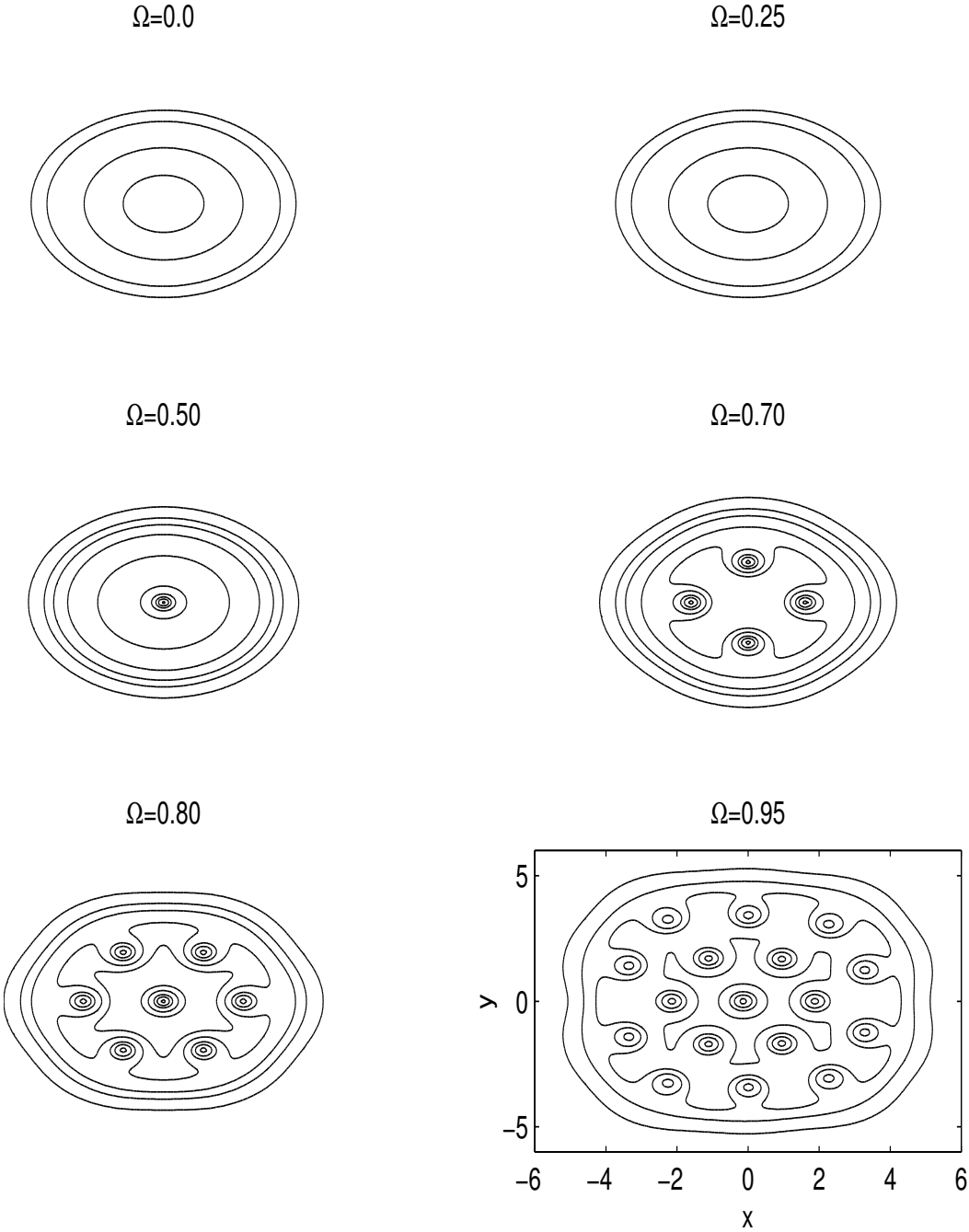


Figure 2.1 (cont'd): Contour plots.

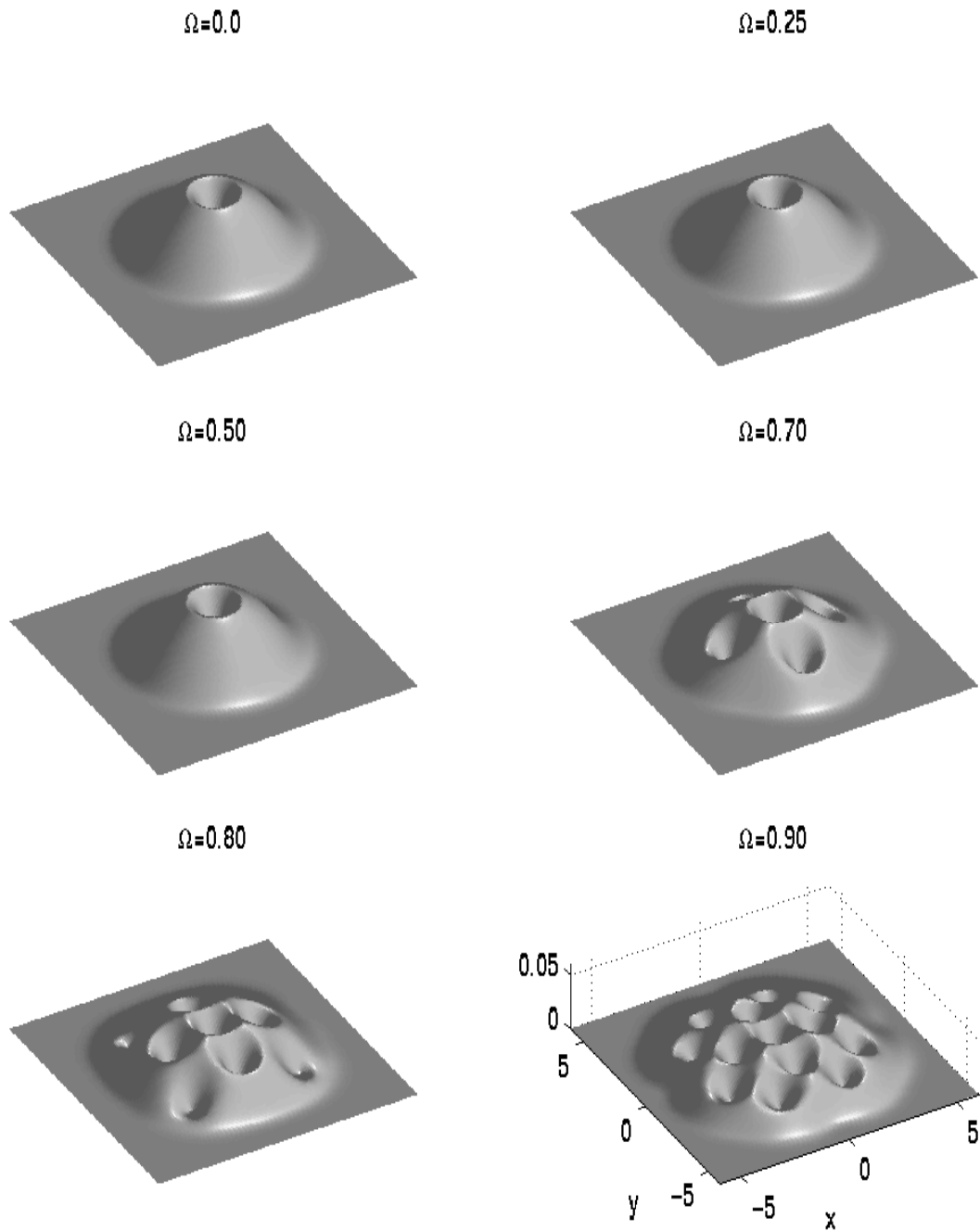


Figure 2.2: Surface plots of central vortex ground state density function $|\phi^v(x, y)|^2$ in 2D with $\gamma_y = 1$ and $\beta_2 = 100$ for different Ω in Example 2.2.

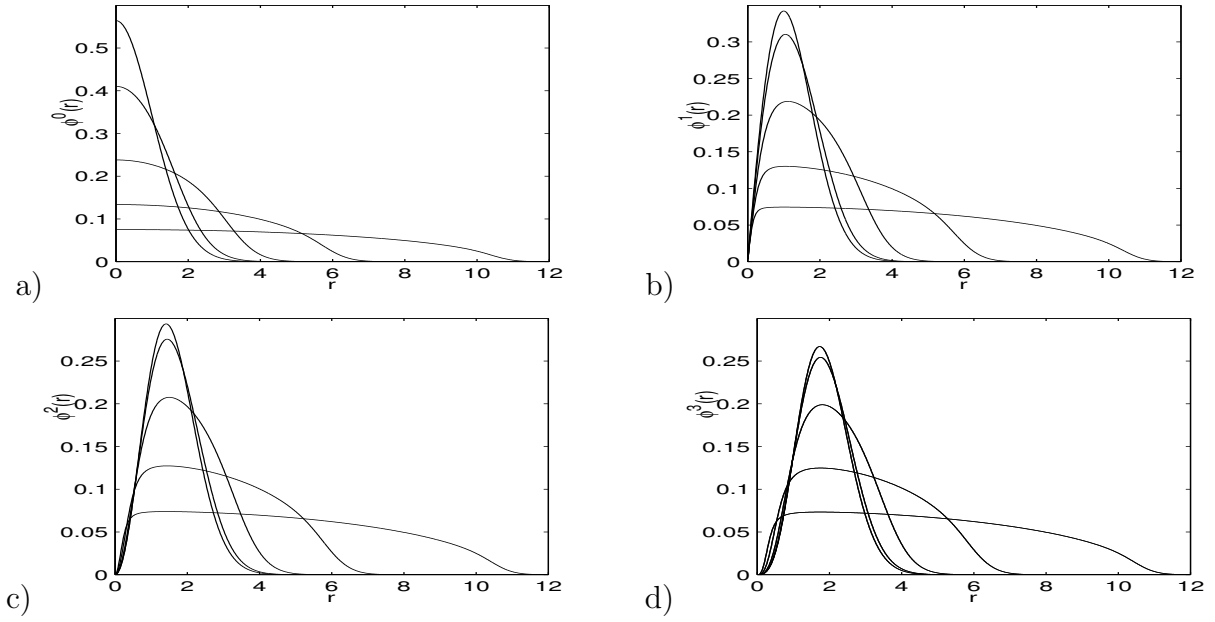


Figure 2.3: Symmetric and central vortex states in 2D with $\gamma_y = 1$ for $\beta_2 = 0, 10, 100, 1000, 10000$ (in the order of decreasing of peak). a). Symmetric state $\phi^0(r)$ Central vortex states $\phi^m(r)$: b). $m = 1$, c). $m = 2$ and d). $m = 3$.

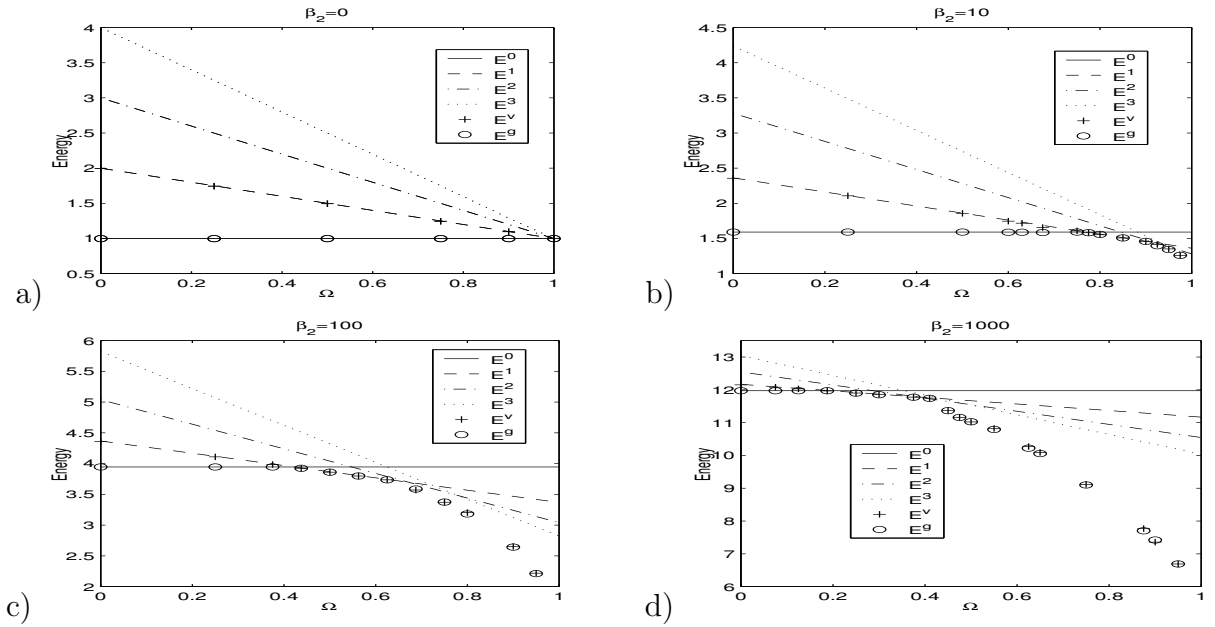


Figure 2.4: Energy diagrams for ground state, i.e. $E^g := E_{\beta,\Omega}^g$, symmetric state, i.e. $E^0 := E_{\beta,\Omega}^0$, central vortex states, i.e. $E^m := E_{\beta,\Omega}^m$, and central vortex ground state, i.e. $E^v := E_{\beta,\Omega}^v$, in 2d with $\gamma_y = 1$ for different β_2 and Ω in Example 2.2.

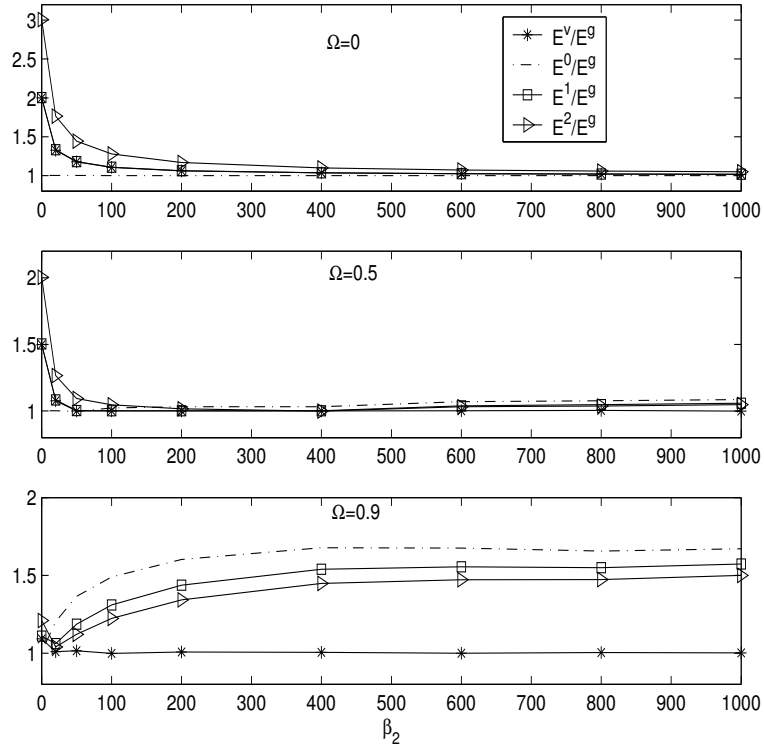


Figure 2.5: Ratios between the energy of different states in Example 2.2.

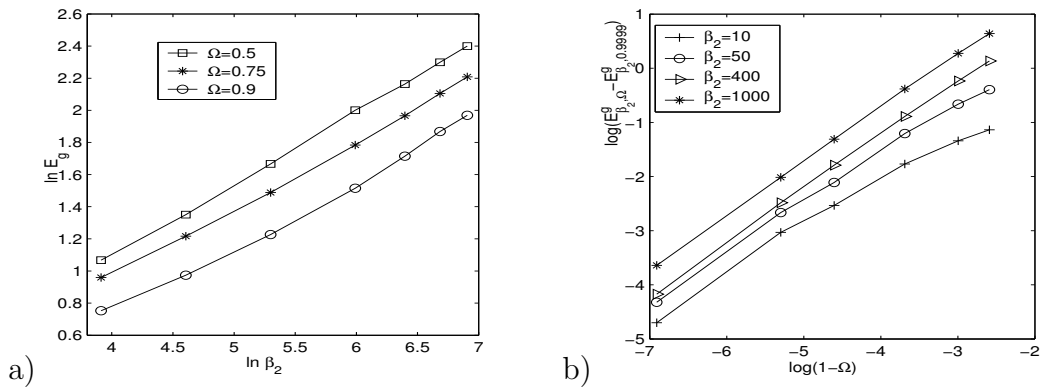


Figure 2.6: Asymptotics of the energy for the ground state in Example 2.2 a). When $\beta_2 \gg 1$, b). When $\Omega \approx \gamma_{xy} = 1$.

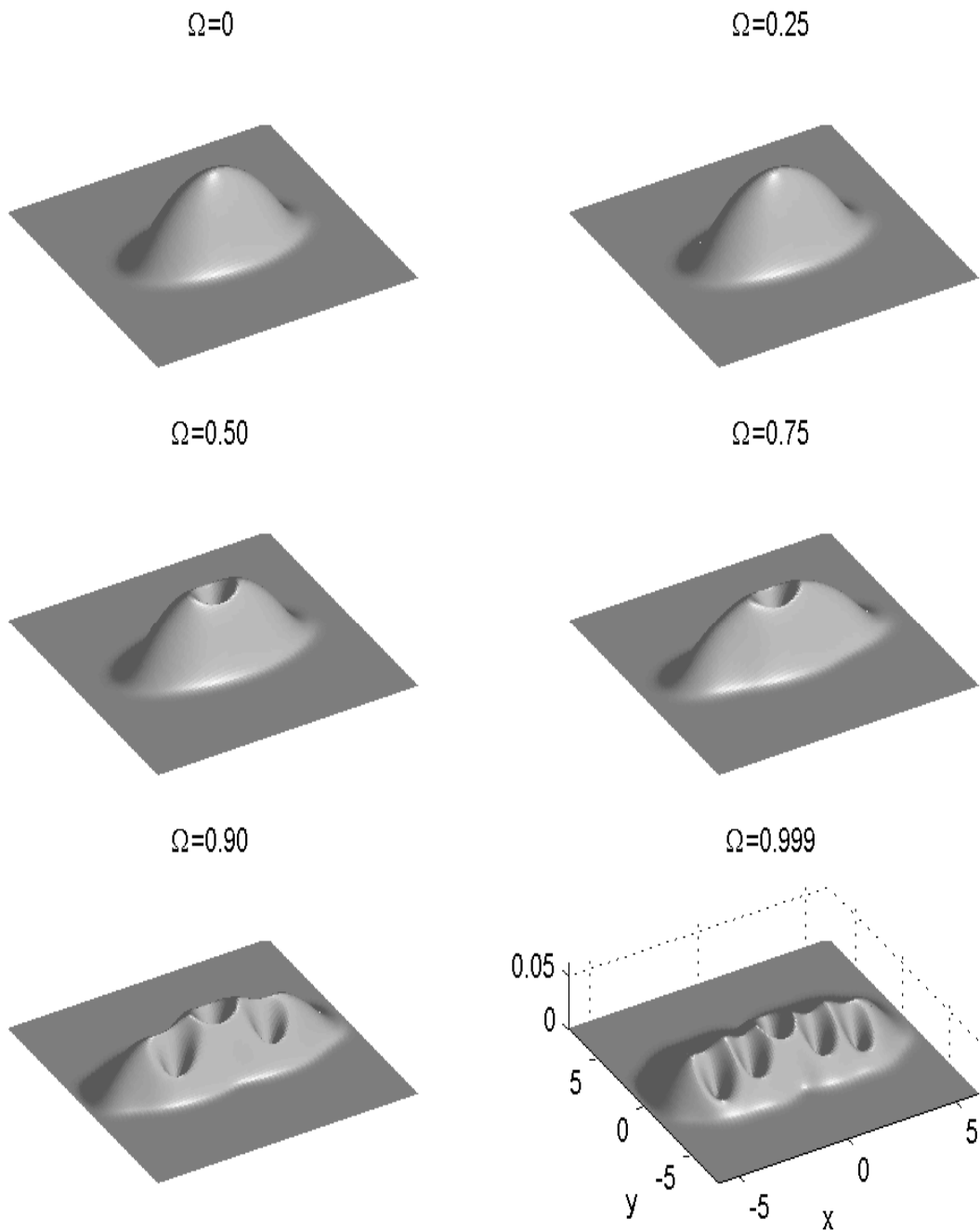


Figure 2.7: Surface plots of ground state density function $|\phi^g(x, y)|^2$ in 2D with $\beta_2 = 100$ in a nonsymmetric trap, i.e. $\gamma_y = 1.5$ for different Ω in Example 2.3.

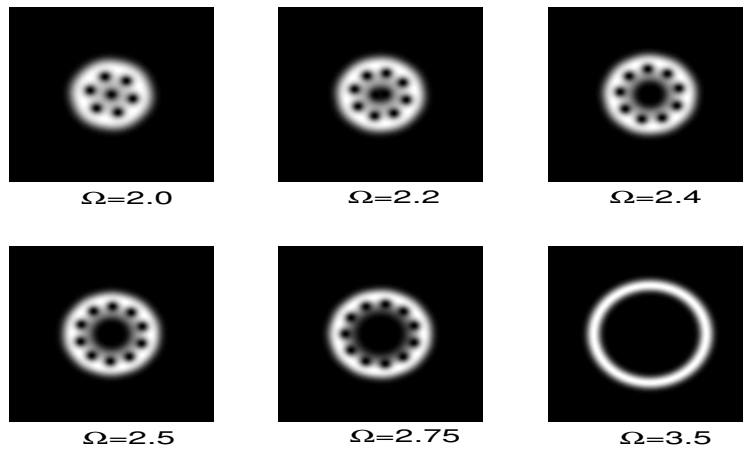


Figure 2.8: Image plots of ground state density function $|\phi^g(x, y)|^2$ in a trap $\frac{1}{2}(x^2 + y^2 + \tau(x^2 + y^2)^2)$ with $\tau = 0.5$ for different Ω in Example 2.4. The size of each figure is on $[-6, 6] \times [-6, 6]$.

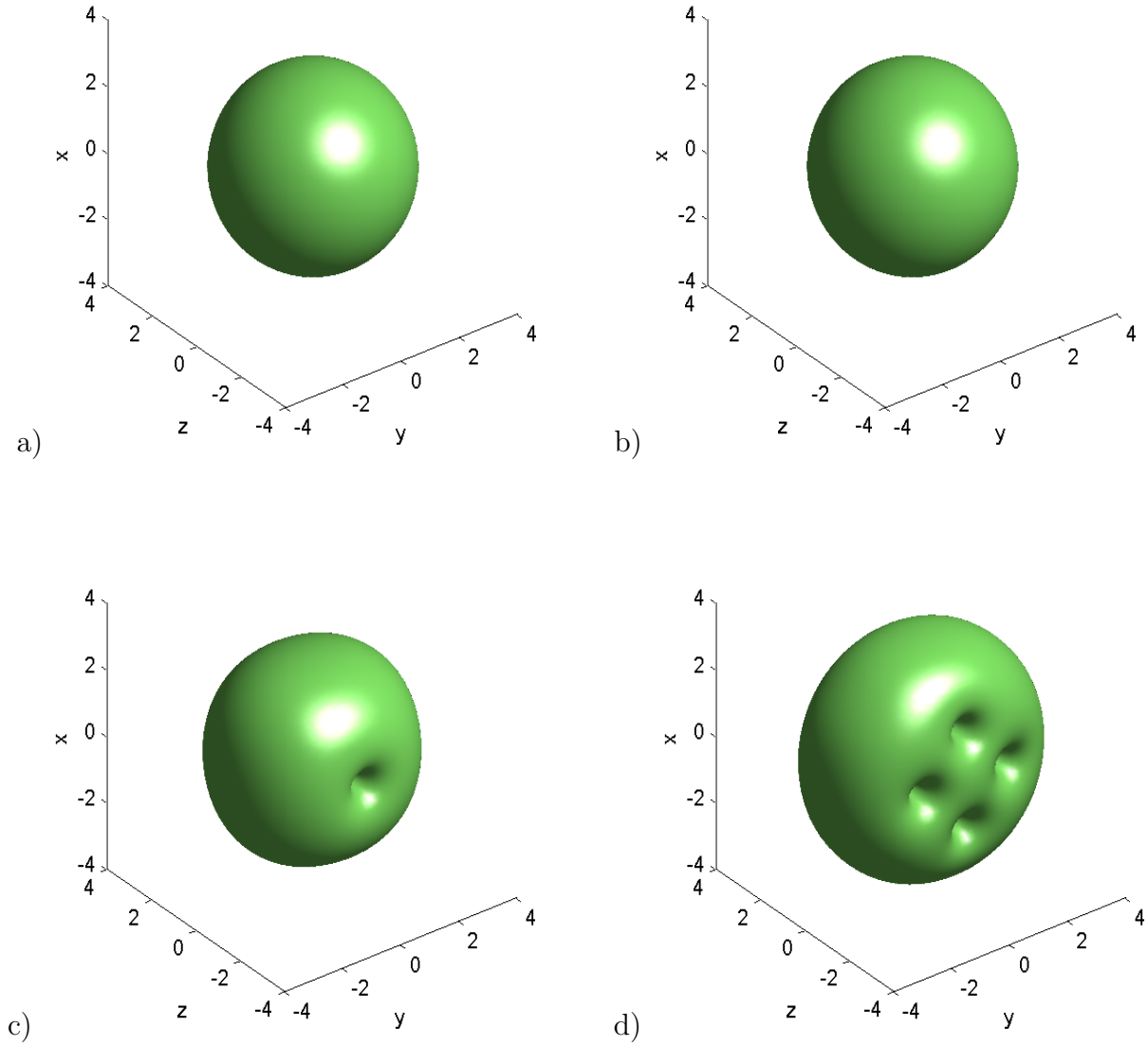


Figure 2.9: Ground states and central vortex ground states in 3D with $\gamma_y = \gamma_z = 1$ and $\beta_3 = 100$ for different Ω in Example 2.5: (a) $\Omega = 0$, (b) $\Omega = 0.5$, (c) $\Omega = 0.8$ and (d) $\Omega = 0.9$. (i) Isosurface plots of ground states $|\phi^g(x, y, z)|^2 = 0.001$.

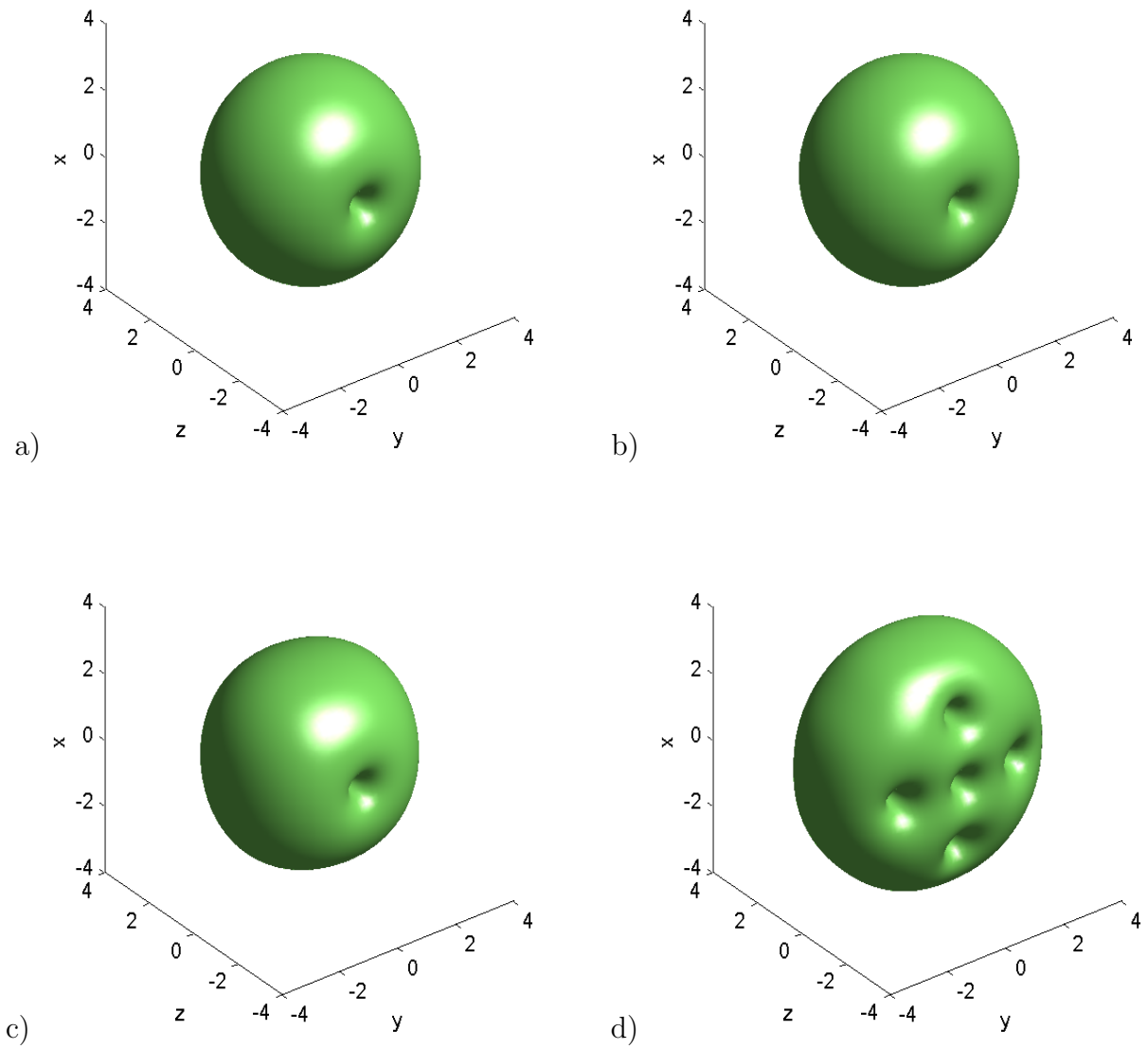


Figure 2.9 (cont'd): (iv) Isosurface plots of central vortex ground states $|\phi^v(x, y, z)|^2 = 0.001$.

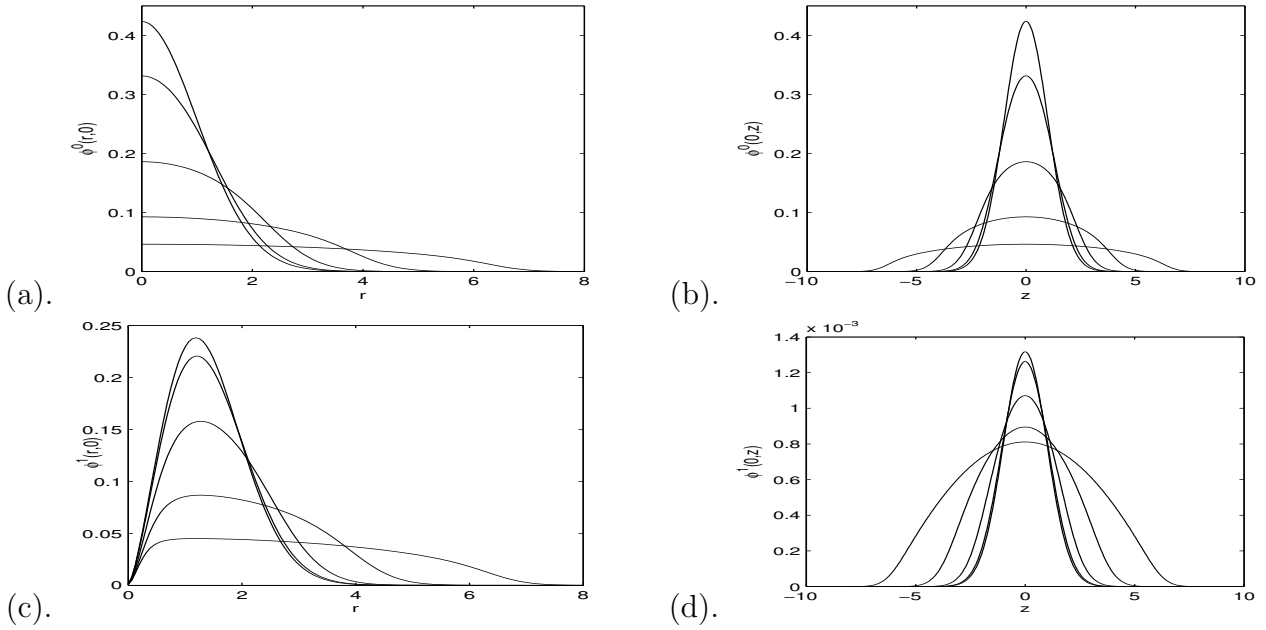


Figure 2.10: Cylindrically symmetric (upper row) and central vortex (lower row) states in 3D for $\beta_3 = 0.0, 10.0, 100.0, 1000.0, 10000.0$ (in the order of decreasing of peak). a). $\phi^0(r, 0)$; b). $\phi^0(0, z)$; c). $\phi^1(r, 0)$; d). $\phi^1(0, z)$.

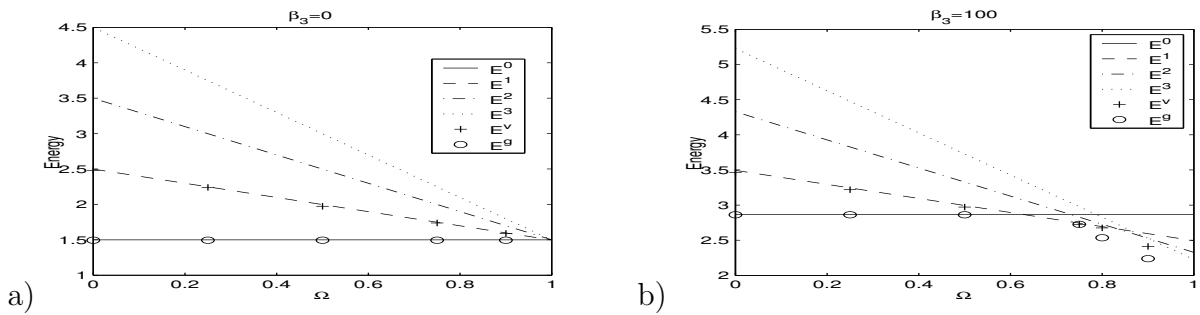


Figure 2.11: Energy diagrams for ground state, Cylindrically symmetric state, central vortex states in 3D with $\gamma_y = 1$ and $\gamma_z = 1.0$ in Example 2.5 for different β_2 and Ω .

Dynamics of rotating Bose-Einstein condensate

The properties of a BEC in a rotational frame at temperatures T much smaller than the critical condensation temperature T_c are modelled by the well-known time-dependent GPE (2.10) [4, 25, 38, 39, 44, 70].

In order to study effectively the dynamics of BEC, especially in the strong repulsive interaction regime, i.e. $\beta_d \gg 1$ in (2.10), an efficient and accurate numerical method is one of the key issues. Our aim of this chapter is to develop an efficient, unconditionally stable and accurate numerical method for discretizing the GPE in a rotational frame by applying a time-splitting technique and an ADI technique, and constructing appropriately spectral basis functions.

This chapter is organized as follows. In section 3.1, we review some properties of GPE in a rotational frame (2.10) including conservation laws and analytical solutions of condensate widths. In section 3.2, we present a new time-splitting Fourier pseudospectral method for efficient and accurate simulation of GPE (2.10) in 2D & 3D. In section 3.3, extensive numerical results are reported to demonstrate the efficiency and spectral resolution in space of our new numerical method. The method is applied to study the vortex lattice dynamics by changing the trap frequency, and to study the generation of a giant vortex numerically. Finally some conclusions are

drawn in section 3.4.

3.1 Some properties of the GPE

In this section, we will review some properties of the GPE with an angular momentum rotation term (2.10), which will be used to test our new numerical method proposed in the next section. First of all, the GPE (2.10) is time reversible and time transverse invariant. Secondly, it has at least two important invariants which are the *normalization of the wave function* (2.11) and the *energy* (2.12). Thirdly, it was proven that at least for radial symmetric trap in 2D or cylindrical symmetric trap in 3D, i.e. $\gamma_x = \gamma_y$ in (2.10), the angular momentum expectation and energy for non-rotating part are conserved [19], that is, for any given initial data $\psi_0(\mathbf{x})$ for (2.10),

$$\langle L_z \rangle(t) \equiv \langle L_z \rangle(0), \quad E_{\beta,0}(\psi) \equiv E_{\beta,0}(\psi_0), \quad t \geq 0, \quad (3.1)$$

where the angular momentum expectation, a measure of the vortex flux, is defined as

$$\langle L_z \rangle(t) := \int_{\mathbb{R}^d} \bar{\psi}(\mathbf{x}, t) L_z \psi(\mathbf{x}, t) d\mathbf{x} = i \int_{\mathbb{R}^d} \bar{\psi}(\mathbf{x}, t) (y \partial_x - x \partial_y) \psi(\mathbf{x}, t) d\mathbf{x}, \quad t \geq 0. \quad (3.2)$$

Other very useful quantities characterizing the dynamics of rotating BEC in 2D are the condensate width defined as

$$\delta_x(t) = \int_{\mathbb{R}^d} x^2 |\psi(\mathbf{x}, t)|^2 d\mathbf{x}, \quad \delta_y(t) = \int_{\mathbb{R}^d} y^2 |\psi(\mathbf{x}, t)|^2 d\mathbf{x}, \quad \delta_r(t) = \delta_x(t) + \delta_y(t). \quad (3.3)$$

As proven in [10], in 2D with a radial symmetric trap, i.e. $d = 2$ and $\gamma_x = \gamma_y := \gamma_r$ in (2.10), for any initial data $\psi_0(x, y)$ for (2.10), we have for any $t \geq 0$

$$\delta_r(t) = \frac{E_{\beta,\Omega}(\psi_0) + \Omega \langle L_z \rangle(0)}{\gamma_r^2} [1 - \cos(2\gamma_r t)] + \delta_r^{(0)} \cos(2\gamma_r t) + \frac{\delta_r^{(1)}}{2\gamma_r} \sin(2\gamma_r t), \quad (3.4)$$

where $\delta_r^{(0)} := \delta_r(0) = \delta_x(0) + \delta_y(0)$ and $\delta_r^{(1)} := \dot{\delta}_r(0) = \dot{\delta}_x(0) + \dot{\delta}_y(0)$ with for $\alpha = x$ or y

$$\delta_\alpha(0) = \delta_\alpha^{(0)} = \int_{\mathbb{R}^2} \alpha^2 |\psi_0(\mathbf{x})|^2 d\mathbf{x},$$

$$\dot{\delta}_\alpha(0) = \delta_\alpha^{(1)} = 2 \int_{\mathbb{R}^2} \alpha \left[-\Omega |\psi_0|^2 (x\partial_y - y\partial_x) \alpha + \text{Im} \left(\bar{\psi}_0 \partial_\alpha \psi_0 \right) \right] d\mathbf{x}.$$

Furthermore, when the initial data $\psi_0(x, y)$ satisfies

$$\psi_0(x, y) = f(r)e^{im\theta} \quad \text{with } m \in Z \quad \text{and } f(0) = 0 \quad \text{when } m \neq 0, \quad (3.5)$$

with (r, θ) being the polar coordinates in 2D, we have, for any $t \geq 0$,

$$\begin{aligned} \delta_x(t) &= \delta_y(t) = \frac{1}{2} \delta_r(t) \\ &= \frac{E_{\beta, \Omega}(\psi_0) + m\Omega}{2\gamma_x^2} [1 - \cos(2\gamma_x t)] + \delta_x^{(0)} \cos(2\gamma_x t) + \frac{\delta_x^{(1)}}{2\gamma_x} \sin(2\gamma_x t). \end{aligned} \quad (3.6)$$

These immediately imply that $\delta_r(t)$ is a periodic function with angular frequency doubling the trapping frequency in 2D with a radial symmetric trap, and also $\delta_x(t)$ and $\delta_y(t)$ are periodic functions with frequency doubling the trapping frequency provided that the initial data satisfies (3.5).

3.2 A TSSP method for the GPE

In this section, we will present an explicit, unconditionally stable and spectrally accurate numerical method to solve the GPE (2.10) for dynamics of rotating BEC.

Due to the external trapping potential $V_d(\mathbf{x})$, the solution $\psi(\mathbf{x}, t)$ of (2.10) decays to zero exponentially fast when $|\mathbf{x}| \rightarrow \infty$. Thus in practical computation, we always truncate the problem (2.10) into a bounded computational domain with homogeneous Dirichlet boundary condition:

$$i \partial_t \psi(\mathbf{x}, t) = -\frac{1}{2} \nabla^2 \psi + (V_d(\mathbf{x}) - iW(\mathbf{x}))\psi + \beta_d |\psi|^2 \psi - \Omega L_z \psi, \quad (3.7)$$

$$\psi(\mathbf{x}, t) = 0, \quad \mathbf{x} \in \Gamma = \partial\Omega_{\mathbf{x}}, \quad t \geq 0, \quad (3.8)$$

$$\psi(\mathbf{x}, 0) = \psi_0(\mathbf{x}), \quad \mathbf{x} \in \Omega_{\mathbf{x}}, \quad (3.9)$$

where $W(\mathbf{x}) \geq 0$ corresponds to a localized loss term [122]. Here we choose $\Omega_{\mathbf{x}} = [a, b] \times [c, d]$ in 2D, and resp., $\Omega_{\mathbf{x}} = [a, b] \times [c, d] \times [e, f]$ in 3D, with $|a|, b, |c|, d, |e|$ and f sufficiently large. The use of more sophisticated radiation boundary conditions is an interesting topic that remains to be examined in the future.

3.2.1 Time-splitting

We choose a time step size $\Delta t > 0$. For $n = 0, 1, 2, \dots$, from time $t = t_n = n\Delta t$ to $t = t_{n+1} = t_n + \Delta t$, the GPE (3.7) is first solved in two splitting steps. One solves first

$$i \partial_t \psi(\mathbf{x}, t) = -\frac{1}{2} \nabla^2 \psi(\mathbf{x}, t) - \Omega L_z \psi(\mathbf{x}, t) \quad (3.10)$$

for the time step of length Δt , followed by solving

$$i \partial_t \psi(\mathbf{x}, t) = (V_d(\mathbf{x}) - iW(\mathbf{x}))\psi(\mathbf{x}, t) + \beta_d |\psi(\mathbf{x}, t)|^2 \psi(\mathbf{x}, t) \quad (3.11)$$

for the same time step. For $t \in [t_n, t_{n+1}]$, multiplying (3.11) by $\bar{\psi}$, the conjugate of ψ , we get

$$i \bar{\psi} \partial_t \psi(\mathbf{x}, t) = (V_d(\mathbf{x}) - iW(\mathbf{x}))|\psi(\mathbf{x}, t)|^2 + \beta_d |\psi(\mathbf{x}, t)|^4. \quad (3.12)$$

Subtracting the conjugate of (3.12) from (3.12) and multiplying by -i, one obtains

$$\frac{d}{dt} |\psi(\mathbf{x}, t)|^2 = -2W(\mathbf{x})|\psi(\mathbf{x}, t)|^2. \quad (3.13)$$

Solving (3.13), we get

$$|\psi(\mathbf{x}, t)|^2 = e^{-2W(\mathbf{x})(t-t_n)} |\psi(\mathbf{x}, t_n)|^2, \quad t_n \leq t \leq t_{n+1}. \quad (3.14)$$

Substituting (3.14) into (3.11), we obtain

$$i \partial_t \psi(\mathbf{x}, t) = (V_d(\mathbf{x}) - iW(\mathbf{x}))\psi(\mathbf{x}, t) + \beta_d e^{-2W(\mathbf{x})(t-t_n)} |\psi(\mathbf{x}, t_n)|^2 \psi(\mathbf{x}, t), \quad (3.15)$$

Integrating the equation (3.15) from t_n to t , we find for $\mathbf{x} \in \Omega_x$ and $t_n \leq t \leq t_{n+1}$

$$\psi(\mathbf{x}, t) = \begin{cases} e^{-i(V_d(\mathbf{x}) + \beta_d |\psi(\mathbf{x}, t_n)|^2)(t-t_n)} \psi(\mathbf{x}, t_n), & W(\mathbf{x}) = 0, \\ \frac{\psi(\mathbf{x}, t_n)}{e^{W(\mathbf{x})(t-t_n)}} e^{-i[V_d(\mathbf{x})(t-t_n) + \beta_d |\psi(\mathbf{x}, t_n)|^2(1 - e^{-2W(\mathbf{x})(t-t_n)})/2W(\mathbf{x})]} & W(\mathbf{x}) \neq 0. \end{cases} \quad (3.16)$$

To discretize (3.10) in space, compared with nonrotating BEC [9], i.e. $\Omega = 0$ in (2.10), the main difficulty is that the coefficients in L_z are *not* constants which cause big trouble in applying sine or Fourier pseudospectral discretization. Due to the special structure in the angular momentum rotation term L_z , we will apply

the ADI technique and decouple the operator $-\frac{1}{2}\nabla^2 - \Omega L_z$ into two one dimension operators such that each operator becomes a summation of terms with constant coefficients in that dimension. Therefore, they can be discretized in space by Fourier pseudospectral method and integrated the ODEs in phase space analytically. The details for discretizing (3.10) in 2D & 3D will be presented in the next two subsections respectively.

3.2.2 Discretization in 2D

When $d = 2$ in (3.10), we choose mesh sizes $\Delta x > 0$ and $\Delta y > 0$ with $\Delta x = (b-a)/M$ and $\Delta y = (d-c)/N$ for M and N even positive integers, and let the grid points be

$$x_j = a + j\Delta x, \quad j = 0, 1, 2, \dots, M; \quad y_k = c + k\Delta y, \quad k = 0, 1, 2, \dots, N. \quad (3.17)$$

Let ψ_{jk}^n be the approximation of $\psi(x_j, y_k, t_n)$ and ψ^n be the solution vector with component ψ_{jk}^n .

From time $t = t_n$ to $t = t_{n+1}$, we solve (3.10) first

$$i \partial_t \psi(\mathbf{x}, t) = -\frac{1}{2} \partial_{xx} \psi(\mathbf{x}, t) - i\Omega y \partial_x \psi(\mathbf{x}, t) \quad (3.18)$$

for the time step of length Δt , followed by solving

$$i \partial_t \psi(\mathbf{x}, t) = -\frac{1}{2} \partial_{yy} \psi(\mathbf{x}, t) + i\Omega x \partial_y \psi(\mathbf{x}, t) \quad (3.19)$$

for the same time step. For each fixed y , the operator in the equation (3.18) is in x -direction with constant coefficients and thus we can discretize it in x -direction by a Fourier pseudospectral method. Assume

$$\psi(x, y, t) = \sum_{p=-M/2}^{M/2-1} \hat{\psi}_p(y, t) \exp[i\mu_p(x-a)], \quad (3.20)$$

where $\mu_p = \frac{2p\pi}{b-a}$ and $\hat{\psi}_p(y, t)$ is the Fourier coefficient for the p -th mode in x -direction. Plugging (3.20) into (3.18), noticing the orthogonality of the Fourier functions, we obtain for $-\frac{M}{2} \leq p \leq \frac{M}{2} - 1$ and $c \leq y \leq d$:

$$i \partial_t \hat{\psi}_p(y, t) = \left(\frac{1}{2} \mu_p^2 + \Omega y \mu_p \right) \hat{\psi}_p(y, t), \quad t_n \leq t \leq t_{n+1}. \quad (3.21)$$

The above linear ODE can be integrated in time *exactly* and we obtain

$$\widehat{\psi}_p(y, t) = \exp \left[-i \left(\frac{1}{2} \mu_p^2 + \Omega y \mu_p \right) (t - t_n) \right] \widehat{\psi}_p(y, t_n), \quad t_n \leq t \leq t_{n+1}. \quad (3.22)$$

Similarly, for each fixed x , the operator in the equation (3.19) is in the y -direction with constant coefficients and thus we can discretize it in the y -direction by a Fourier pseudospectral method. Assume

$$\psi(x, y, t) = \sum_{q=-N/2}^{N/2-1} \widehat{\psi}_q(x, t) \exp[i\lambda_q(y - c)], \quad (3.23)$$

where $\lambda_q = \frac{2q\pi}{a-c}$ and $\widehat{\psi}_q(x, t)$ is the Fourier coefficient for the q -th mode in the y -direction. Plugging (3.23) into (3.19), noticing the orthogonality of the Fourier functions, we obtain for $-\frac{N}{2} \leq q \leq \frac{N}{2} - 1$ and $a \leq x \leq b$:

$$i \partial_t \widehat{\psi}_q(x, t) = \left(\frac{1}{2} \lambda_q^2 - \Omega x \lambda_q \right) \widehat{\psi}_q(x, t), \quad t_n \leq t \leq t_{n+1}. \quad (3.24)$$

Again the above linear ODE can be integrated in time *exactly* and we obtain

$$\widehat{\psi}_q(x, t) = \exp \left[-i \left(\frac{1}{2} \lambda_q^2 - \Omega x \lambda_q \right) (t - t_n) \right] \widehat{\psi}_q(x, t_n), \quad t_n \leq t \leq t_{n+1}. \quad (3.25)$$

From time $t = t_n$ to $t = t_{n+1}$, we combine the splitting steps via the standard second order Strang splitting [9, 126]:

$$\begin{aligned} \psi_{jk}^{(1)} &= \sum_{p=-M/2}^{M/2-1} e^{-i\Delta t(\mu_p^2 + 2\Omega y_k \mu_p)/4} \widehat{(\psi_k^n)}_p e^{i\mu_p(x_j - a)}, \quad 0 \leq j \leq M, \quad 0 \leq k \leq N, \\ \psi_{jk}^{(2)} &= \sum_{q=-N/2}^{N/2-1} e^{-i\Delta t(\lambda_q^2 - 2\Omega x_j \lambda_q)/4} \widehat{(\psi_j^{(1)})}_q e^{i\lambda_q(y_k - c)}, \quad 0 \leq k \leq N, \quad 0 \leq j \leq M, \\ \psi_{jk}^{(3)} &= \begin{cases} e^{-i\Delta(V_2(x_j, y_k) + \beta_2 |\psi_{jk}^{(2)}|^2)} \psi_{jk}^{(2)}, & W(x_j, y_k) = 0, \\ \frac{\psi_{jk}^{(2)}}{e^{\Delta t W(x_j, y_k)}} e^{-i[\Delta t V_2(x_j, y_k) + \beta_2 |\psi_{jk}^{(2)}|^2 (1 - e^{-2\Delta t W(x_j, y_k)})/2W(x_j, y_k)]} & W(x_j, y_k) > 0, \end{cases} \\ \psi_{jk}^{(4)} &= \sum_{q=-N/2}^{N/2-1} e^{-i\Delta t(\lambda_q^2 - 2\Omega x_j \lambda_q)/4} \widehat{(\psi_j^{(3)})}_q e^{i\lambda_q(y_k - c)}, \quad 0 \leq k \leq N, \quad 0 \leq j \leq M, \\ \psi_{jk}^{n+1} &= \sum_{p=-M/2}^{M/2-1} e^{-i\Delta t(\mu_p^2 + 2\Omega y_k \mu_p)/4} \widehat{(\psi_k^{(4)})}_p e^{i\mu_p(x_j - a)}, \quad 0 \leq j \leq M, \quad 0 \leq k \leq N, \end{aligned} \quad (3.26)$$

where for each fixed k , $(\widehat{\psi_k^*})_p$ ($p = -M/2, \dots, M/2 - 1$), the Fourier coefficients of the vector $\psi_k^* = (\psi_{0k}^*, \psi_{1k}^*, \dots, \psi_{(M-1)k}^*)^T$, are defined as

$$(\widehat{\psi_k^*})_p = \frac{1}{M} \sum_{j=0}^{M-1} \psi_{jk}^* e^{-i\mu_p(x_j-a)}, \quad p = -\frac{M}{2}, \dots, \frac{M}{2} - 1; \quad (3.27)$$

similarly, for each fixed j , $(\widehat{\psi_j^*})_q$ ($q = -N/2, \dots, N/2 - 1$), the Fourier coefficients of vector $\psi_j^* = (\psi_{j0}^*, \psi_{j1}^*, \dots, \psi_{j(N-1)}^*)^T$, are defined as

$$(\widehat{\psi_j^*})_q = \frac{1}{N} \sum_{m=0}^{N-1} \psi_{jm}^* e^{-i\lambda_q(y_m-c)}, \quad q = -\frac{N}{2}, \dots, \frac{N}{2} - 1. \quad (3.28)$$

For the algorithm (3.26) presented here, the total memory requirement is $O(MN)$ and the total computational cost per time step is $O(MN \ln(MN))$. The scheme is time reversible, just as it holds for the GPE (2.10). It is unchanged if we interchange $n \leftrightarrow n+1$ and $\Delta t \leftrightarrow -\Delta t$. Also, a main advantage of the numerical method is its time-transverse invariance, just as it holds for the GPE (2.10) itself. If a constant α is added to the external potential V_2 , then the discrete wave functions ψ_{jk}^{n+1} obtained from (3.26) get multiplied by the phase factor $e^{-i\alpha(n+1)\Delta t}$, which leaves the discrete quadratic observable $|\psi_{jk}^{n+1}|^2$ unchanged. This property does not hold for the finite difference scheme [74, 132], the leap-frog spectral method [137] and the efficient discretization proposed in [10] for GPE with an angular momentum term.

3.2.3 Discretization in 3D

When $d = 3$ in (3.10), we choose mesh sizes $\Delta x > 0$, $\Delta y > 0$ and $\Delta z > 0$ with $\Delta x = (b-a)/M$, $\Delta y = (d-c)/N$ and $\Delta z = (f-e)/L$ for M , N and L even positive integers, and let the grid points be

$$x_j = a + j\Delta x, \quad 0 \leq j \leq M; \quad y_k = c + k\Delta y, \quad 0 \leq k \leq N; \quad z_l = e + l\Delta z, \quad 0 \leq l \leq L.$$

Let ψ_{jkl}^n be the approximation of $\psi(x_j, y_k, z_l, t_n)$ and ψ^n be the solution vector with component ψ_{jkl}^n .

Similarly as those for 2D case, from time $t = t_n$ to $t = t_{n+1}$, we solve (3.10) first

$$i \partial_t \psi(\mathbf{x}, t) = \left(-\frac{1}{2} \partial_{xx} - \frac{1}{4} \partial_{zz} - i\Omega y \partial_x \right) \psi(\mathbf{x}, t) \quad (3.29)$$

for the time step of length Δt , followed by solving

$$i \partial_t \psi(\mathbf{x}, t) = \left(-\frac{1}{2} \partial_{yy} - \frac{1}{4} \partial_{zz} + i\Omega x \partial_y \right) \psi(\mathbf{x}, t) \quad (3.30)$$

for the same time step. For each fixed y , the operator in the equation (3.29) is in x and z -directions with constant coefficients and thus we can discretize it in x and z -directions by a Fourier pseudospectral method. Similarly, for each fixed x , the operator in the equation (3.30) is in y and z -directions with constant coefficients and thus we can discretize it in y and z -directions by a Fourier pseudospectral method. The discretizations of (3.29) and (3.30) are similar as those for (3.18) and (3.19) respectively and they are omitted here. For simplicity and convenience of the reader, here we only present the algorithm for 3D GPE with an angular momentum rotation term (2.10) with $0 \leq j \leq M$, $0 \leq k \leq N$ and $0 \leq l \leq L$:

$$\begin{aligned} \psi_{jkl}^{(1)} &= \sum_{p=-M/2}^{M/2-1} \sum_{s=-L/2}^{L/2-1} e^{-i\Delta t(2\mu_p^2 + \gamma_s^2 + 4\Omega y_k \mu_p)/8} \widehat{(\psi_k^n)}_{ps} e^{i\mu_p(x_j-a)} e^{i\gamma_s(z_l-e)}, \\ \psi_{jkl}^{(2)} &= \sum_{q=-N/2}^{N/2-1} \sum_{s=-L/2}^{L/2-1} e^{-i\Delta t(2\lambda_q^2 + \gamma_s^2 - 4\Omega x_j \lambda_q)/8} \widehat{(\psi_j^{(1)})}_{qs} e^{i\lambda_q(y_k-c)} e^{i\gamma_s(z_l-e)}, \\ \psi_{jkl}^{(3)} &= \begin{cases} e^{-i\Delta t(V(x_j, y_k, z_l) + \beta_3 |\psi_{jkl}^{(2)}|^2)} \psi_{jkl}^{(2)}, & W(x_j, y_k, z_l) = 0, \\ \frac{\psi_{jkl}^{(2)}}{e^{\Delta t W(x_j, y_k, z_l)}} \exp -i(\Delta t V(x_j, y_k, z_l) + \beta_3 |\psi_{jkl}^{(2)}|^2 (1 - e^{-2\Delta t W(x_j, y_k, z_l)}) / 2W(x_j, y_k, z_l)) & W(x_j, y_k, z_l) > 0, \end{cases} \\ \psi_{jkl}^{(4)} &= \sum_{q=-N/2}^{N/2-1} \sum_{s=-L/2}^{L/2-1} e^{-i\Delta t(2\lambda_q^2 + \gamma_s^2 - 4\Omega x_j \lambda_q)/8} \widehat{(\psi_j^{(3)})}_{qs} e^{i\lambda_q(y_k-c)} e^{i\gamma_s(z_l-e)}, \\ \psi_{jkl}^{n+1} &= \sum_{p=-M/2}^{M/2-1} \sum_{s=-L/2}^{L/2-1} e^{-i\Delta t(2\mu_p^2 + \gamma_s^2 + 4\Omega y_k \mu_p)/8} \widehat{(\psi_k^{(4)})}_{ps} e^{i\mu_p(x_j-a)} e^{i\gamma_s(z_l-e)}, \end{aligned} \quad (3.31)$$

where for each fixed k , $\widehat{(\psi_k^*)}_{ps}$ ($-M/2 \leq p < M/2$, $-L/2 \leq s \leq L/2-1$), the Fourier coefficients of vector ψ_{jkl}^* ($0 \leq j < M$, $0 \leq l < L$), are defined as

$$\widehat{(\psi_k^*)}_{ps} = \frac{1}{ML} \sum_{j=0}^{M-1} \sum_{l=0}^{L-1} \psi_{jkl}^* e^{-i\mu_p(x_j-a)} e^{-i\gamma_s(z_l-e)}, \quad -\frac{M}{2} \leq p < \frac{M}{2}, \quad -\frac{L}{2} \leq s < \frac{L}{2};$$

similarly, for each fixed j , $(\widehat{\psi_j^*})_{qs}$ ($q = -N/1, \dots, N/2 - 1$, $s = -L/2, \dots, L/2 - 1$), the Fourier coefficients of vector ψ_{jkl}^* ($k = 0, \dots, N$, $l = 0, \dots, L$), are defined as

$$(\widehat{\psi_j^*})_{qs} = \frac{1}{NL} \sum_{m=0}^{N-1} \sum_{l=0}^{L-1} \psi_{jkl}^* e^{-i\lambda_q(y_k-c)} e^{-i\gamma_s(z_l-e)}, \quad -\frac{N}{2} \leq q < \frac{N}{2}, \quad -\frac{L}{2} \leq s < \frac{L}{2},$$

where $\gamma_s = \frac{2\pi s}{f-e}$ for $s = -L/2, \dots, L/2 - 1$.

For the discretization in 3D, the total memory requirement is $O(MNL)$ and the total computational cost per time step is $O(MNL \ln(MNL))$. Furthermore, the discretization is time reversible and time transverse invariant in the discretized level.

3.2.4 Stability

We define the usual discrete l^2 -norm for the solution ψ^n as

$$\|\psi^n\|_{l^2} = \sqrt{\frac{b-a}{M} \frac{d-c}{N} \sum_{j=0}^{M-1} \sum_{k=0}^{N-1} |\psi_{jk}^n|^2}, \quad (3.32)$$

for $d = 2$, and for $d = 3$

$$\|\psi^n\|_{l^2} = \sqrt{\frac{b-a}{M} \frac{d-c}{N} \frac{f-e}{L} \sum_{j=0}^{M-1} \sum_{k=0}^{N-1} \sum_{l=0}^{L-1} |\psi_{jkl}^n|^2}. \quad (3.33)$$

For the *stability* of the time-splitting spectral approximations (3.26) for 2D and (3.31) for 3D, we have the following lemma, which shows that the total density is conserved in the discretized level.

Lemma 3.2.1 *The time-splitting spectral schemes (3.26) for 2D and (3.31) for 3D GPE with an angular momentum rotation term are unconditionally stable. In fact, for every mesh sizes $\Delta x > 0$, $\Delta y > 0$ and $\Delta z > 0$, and time step size $\Delta t > 0$,*

$$\|\psi^n\|_{l^2} \equiv \|\psi^0\|_{l^2} = \|\psi_0\|_{l^2}, \quad n = 1, 2, \dots \quad (3.34)$$

Proof: Follows the line of the analogous results for the linear and nonlinear Schrödinger equations in [9, 14, 15, 17].

3.3 Numerical results

In this section, we first test the accuracy of our new numerical method (3.26) for 2D and (3.31) for 3D and compare our numerical results with the analytical results reviewed in section 3.1. Then we apply our new numerical method to study vortex lattice dynamics in rotating BEC by changing the trapping frequencies and to generate a giant vortex by introducing a localized loss term. Our aim is not only to find new physics but also to demonstrate the efficiency and high resolution of our new numerical method.

3.3.1 Accuracy test

To test the accuracy of our numerical method in 2D, we take $\Omega = 0.7$ and $W(\mathbf{x}) = 0$ in (3.7). The initial condition in (3.9) is taken as

$$\psi_0(x, y) = \frac{(\gamma_x \gamma_y)^{\frac{1}{4}}}{\pi^{\frac{1}{2}}} e^{-(\gamma_x x^2 + \gamma_y y^2)/2}, \quad \mathbf{x} = (x, y)^T \in \mathbb{R}^2. \quad (3.35)$$

We take $\gamma_x = 1.0$ and $\gamma_y = 2.0$ in (3.7) and (3.35). Similar example was used in [10, 137] for testing numerical accuracy for different numerical methods for rotating BEC. The GPE (3.7) is solved on $[-8, 8] \times [-8, 8]$, i.e. we take $a = -8$, $b = 8$, $c = -8$ and $d = 8$. Let ψ be the *exact* solution which is obtained numerically using our method with a very fine mesh and small time step, e.g. $\Delta x = \Delta y = \frac{1}{64}$ and $\Delta t = 0.0001$, and $\psi^{(\Delta x, \Delta y, \Delta t)}$ be the numerical solution obtained with the mesh size $(\Delta x, \Delta y)$ and time step Δt .

First we test the spectral accuracy in space by choosing a very small time step $\Delta t = 0.0001$, and solving the problem for each fixed β_2 with different mesh size $\Delta x = \Delta y$ so that the discretization errors in time can be neglected comparing to that in space. The errors $\|\psi(t) - \psi^{(\Delta x, \Delta y, \Delta t)}(t)\|_{l^2}$ at $t = 0.5$ are shown in Table 3.1 for different values β_2 and $h = \Delta x = \Delta y$.

Next we test the second-order accuracy in time. Table 3.2 lists the errors at $t = 0.5$ for different values of β_2 and time steps Δt with a fine mesh in space, i.e. $\Delta x = \Delta y = 1/16$.

h	1/2	1/4	1/8
$\beta_2 = 20$	2.68E-2	6.5E-5	3.41E-10
$\beta_2 = 50$	0.1315	2.01E-3	5.91E-8
$\beta_2 = 100$	0.4287	1.94E-2	8.89E-6

Table 3.1: Discretization error $\|\psi(t) - \psi^{(\Delta x, \Delta y, \Delta t)}(t)\|_{l^2}$ at $t = 0.5$ in space for 2D.

Δt	1/40	1/80	1/160	1/320	1/640
$\beta_2 = 20$	7.86E-4	1.95E-4	4.86E-5	1.21E-5	3.02E-6
$\beta_2 = 50$	2.95E-3	7.24E-4	1.80E-4	4.49E-5	1.12E-5
$\beta_2 = 100$	7.98E-3	1.98E-3	4.76E-4	1.19E-4	2.96E-5

Table 3.2: Discretization error $\|\psi(t) - \psi^{(\Delta x, \Delta y, \Delta t)}(t)\|_{l^2}$ at $t = 0.5$ in time for 2D.

Similarly, to test the accuracy of our numerical method in 3D, we take $\Omega = 0.7$ and $W(\mathbf{x}) = 0$ in (3.7). The initial condition in (3.9) is taken as

$$\psi_0(x, y, z) = \frac{(\gamma_x \gamma_y \gamma_z)^{\frac{1}{4}}}{\pi^{\frac{3}{4}}} e^{-(\gamma_x x^2 + \gamma_y y^2 + \gamma_z z^2)/2}, \quad \mathbf{x} = (x, y, z)^T \in \mathbb{R}^3. \quad (3.36)$$

We take $\gamma_x = \gamma_y = \gamma_z = 1.0$ in (3.7) and (3.36), and solve the GPE (3.7) in 3D on $[-8, 8] \times [-8, 8] \times [-8, 8]$. Again let ψ be the *exact* solution which is obtained numerically using our method with a fine mesh and small time step, e.g. $\Delta x = \Delta y = \Delta z = \frac{1}{8}$ and $\Delta t = 0.0001$, and $\psi^{(\Delta x, \Delta y, \Delta z, \Delta t)}$ be the numerical solution obtained with the mesh size $(\Delta x, \Delta y, \Delta z)$ and the time step Δt . Table 3.3 shows the spatial error $\|\psi(t) - \psi^{(\Delta x, \Delta y, \Delta z, \Delta t)}(t)\|_{l^2}$ at $t = 0.5$ with $\Delta t = 0.0001$ for different values β_3 and mesh size $h = \Delta x = \Delta y = \Delta z$. Table 3.4 lists the errors at $t = 0.5$ for different values of β_3 and time steps Δt with a fine mesh in space, i.e. $\Delta x = \Delta y = \Delta z = 1/8$.

From Tables 3.1&3.2 and 3.3&3.4, we can draw the following conclusions: (i) The method (3.26) or (3.31) is of spectral accuracy in space and second order accuracy in time. (ii) For a given fixed mesh size and time step, when β_d is increasing, the errors are increasing too. This implies that when the number of atoms in the condensate

h	1	1/2	1/4
$\beta_3 = 20$	5.78E-2	1.27E-3	2.38E-8
$\beta_3 = 50$	0.1515	9.50E-3	2.45E-6
$\beta_3 = 100$	0.3075	3.88E-2	7.08E-5

Table 3.3: Discretization error $\|\psi(t) - \psi^{(\Delta x, \Delta y, \Delta z, \Delta t)}(t)\|_{l^2}$ at $t = 0.5$ in space for 3D.

Δt	1/40	1/80	1/160	1/320	1/640
$\beta_3 = 20$	1.778E-4	4.435E-5	1.108E-5	2.767E-6	6.897E-7
$\beta_3 = 50$	6.266E-4	1.559E-4	3.892E-5	9.718E-6	2.422E-6
$\beta_3 = 100$	1.63E-3	4.0379E-4	1.0069E-4	2.5141E-5	6.265E-6

Table 3.4: Discretization error $\|\psi(t) - \psi^{(\Delta x, \Delta y, \Delta z, \Delta t)}(t)\|_{l^2}$ at $t = 0.5$ in time for 3D.

is increasing, i.e. β_d is increasing, more grid points and smaller time step are needed in practical computation in order to achieve a given accuracy.

Furthermore, Figure 3.1 shows time evolution of the normalization $N(\psi)(t)$, energy $E_{\beta, \Omega}(\psi)(t)$, angular momentum expectation $\langle L_z \rangle(t)$ and condensate widths for the above parameters setup in 2D and 3D respectively.

From Figure 3.1, we can see that: (i). The normalization is conserved in both cases which confirms (2.11). (ii). The energy is not conserved in the discretized level, but the perturbation is very small, e.g. less than 5% (c.f. Figure 3.1 a,c,e&g). (iii). The angular momentum expectation is conserved when $\gamma_x = \gamma_y = 1$ (c.f. Figure 3.1 a&e) which confirm the analytical result (3.1), and oscillates when $1 = \gamma_x \neq \gamma_y = 2$ (c.f. Figure 3.1 c&g). (iv) The condensate widths $\delta_x(t)$, $\delta_y(t)$ and $\delta_r(t)$ are periodic functions when $\gamma_x = \gamma_y = 1$ which confirm the analytical result (3.4) (c.f. Figure 3.1 b&f), and are not periodic functions when $1 = \gamma_x \neq \gamma_y = 2$ (c.f. Figure 3.1 d&h).

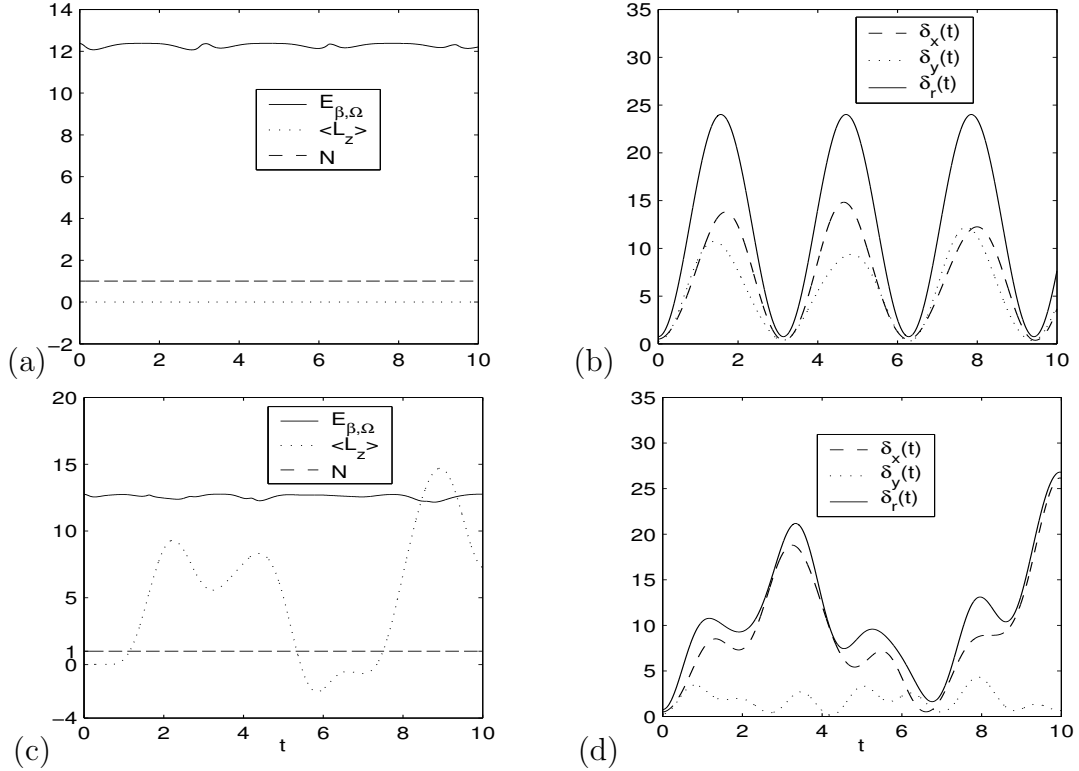


Figure 3.1: Time evolution of the normalization $N(t) := N(\psi)(t)$, energy $E_{\beta,\Omega}(\psi)(t)$, angular momentum expectation $\langle L_z \rangle(t)$ (left column), and condensate widths $\delta_x(t)$, $\delta_y(t)$ and $\delta_r(t)$ (right column). I. Results in 2D for $\gamma_x = \gamma_y = 1$ (a&b), and $\gamma_x = 1$ and $\gamma_y = 2$ (c&d).

3.3.2 Dynamics of a vortex lattice in rotating BEC

In this subsection we numerically study the dynamics of a vortex lattice in rotating BEC by changing trap frequencies. This study was motivated by the recent experiment in which the frequencies of trapping potential of a stable BEC were changed [44]. One of the most striking observations in the experiment is that the condensate contains sheet-like structures rather than individual vortex cores in the dynamics by deforming the static trap. By using the hydrodynamic forms of the GPE (3.7) in Thomas-Fermi regime, Cozzini et. al. [38] tried to study this phenomena theoretically. But they did not find the sheet-like structures by changing the trap frequencies in their theoretical study. Here we study this phenomena by directly simulating the

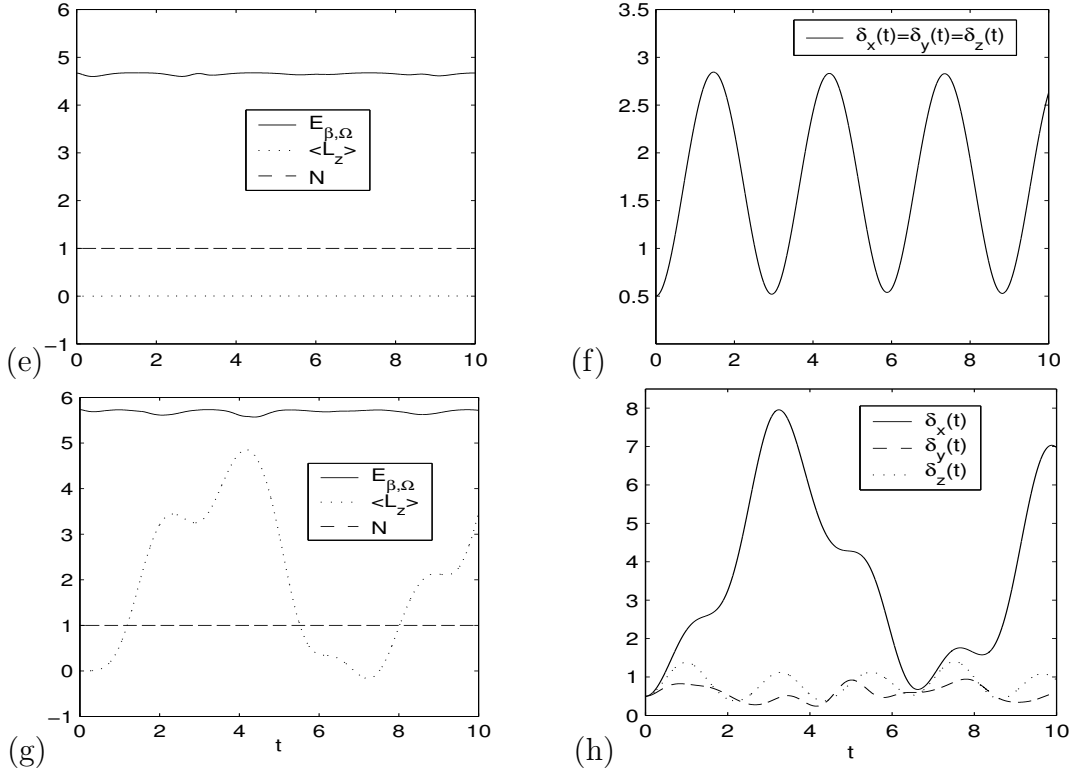


Figure 3.1 (cont'd): II. Results in 3D for $\gamma_x = \gamma_y = \gamma_z = 1$ (e&f), and $\gamma_x = 1$, $\gamma_y = 2$ and $\gamma_z = 1.5$ (g&h).

GPE (3.7) with our new numerical method.

Starting from the trapped BEC containing a vortex lattice composed by about 61 vortices initially, we numerically study their dynamics by solving the 2D GPE with our new numerical method (3.26). We take $d = 2$, $W(x, y) = 0$, and $\Omega = 0.99$ in (3.7). The initial data $\psi_0(\mathbf{x})$ in (3.7) is chosen as the ground state of (3.7) with $d = 2$, $\Omega = 0.99$, $\beta_2 = 100$ and $\gamma_x = \gamma_y = 1$, which is computed numerically by the normalized gradient flow proposed in [13]. In the ground state, there are about 61 vortices in the vortex lattice (c.f. Figure 3.2). We solve the problem on $\Omega_{\mathbf{x}} = [-24, 24] \times [-24, 24]$ with mesh size $\Delta x = \Delta y = 3/16$ and time step $\Delta t = 0.001$.

First we study free expansion of the quantized vortex lattice. In general, the size of a stable vortex lattice in the BEC is too small to visualize it. In experiments, by removing the trap, i. e., letting the vortex lattice freely expand, one can obtain

an enlarged vortex lattice so as to take a photo of it [38]. Of course, they hope the vortex structure doesn't change during the free expansion. Thus theoretical study of free expansion is very helpful for experiments. We start with the stable BEC and remove the trapping at time $t = 0$, i. e., $\gamma_x = \gamma_y = 0$ in the equation (3.7). Similar experiments and numerics were also carried out in [3]. Figure 3.2 shows image plots of the density $|\psi(\mathbf{x}, t)|^2$ at different times for the free expansion of the vortex lattice. From this figure, we can see that when the trap is removed at $t = 0$, the vortex lattice will expand with time and the vortex structure as well as the rotational symmetry is kept during the expansion. This gives a numerical justification for the free expansion used in BEC experiments.

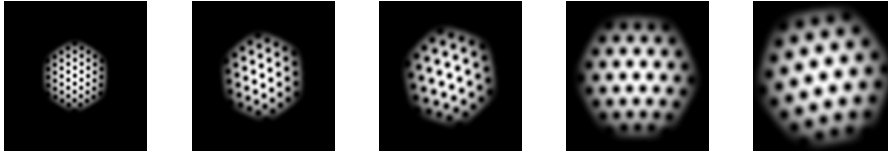


Figure 3.2: Results of free expansion of a quantized vortex lattice: Image plots of the density $|\psi(\mathbf{x}, t)|^2$ on $[-18, 18] \times [-18, 18]$ at different times $t = 0, 0.75, 1.5, 2.0$ and 2.75 (from left to right).

Next, we study dynamics of the quantized vortex lattice by changing the trapping frequencies. We study six different cases: I. $\gamma_x = 1, \gamma_y = 1.5$; II. $\gamma_x = 1, \gamma_y = 0.75$; III. $\gamma_x = 1.5, \gamma_y = 1$; IV. $\gamma_x = 0.75, \gamma_y = 1$; V. $\gamma_x = \sqrt{1.2}, \gamma_y = \sqrt{0.8}$; VI. $\gamma_x = \sqrt{1.4}, \gamma_y = \sqrt{0.6}$; Similar experiments and numerics were also carried out in [3].

Figure 3.3 shows image plots of the density function $|\psi(\mathbf{x}, t)|^2$ at different times for cases I-II for changing frequencies in y-direction only. Figure 3.4 shows similar results for cases III-IV for changing frequencies in x-direction only, and Figure 3.5 shows for cases V-VI for changing frequencies in both x- and y-directions.

In Figures 3.3-3.5, initially the condensate is assumed to be in its ground state. From the numerical results presented here, When the trap frequencies are changed at $t = 0$, we found that (i) Cases I & II corresponds to changing trapping frequency in y -direction only. The condensate initially starts to contract (c.f. (a) of Figure

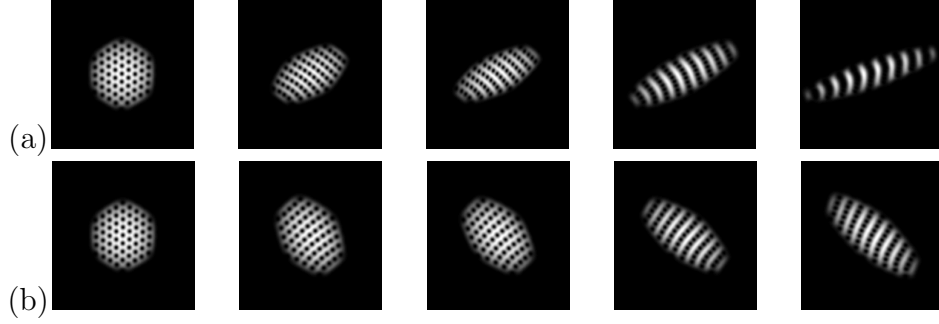


Figure 3.3: Image plots of the density $|\psi(\mathbf{x}, t)|^2$ on $[-18, 18] \times [-18, 18]$ at different times $t=0, 2.0, 4.0, 6.0,$ and 8.0 (from left to right) by changing trapping frequency in y -direction only from $\gamma_y = 1$ to : (a) $\gamma_y = 1.5$; (b) $\gamma_y = 0.75$.

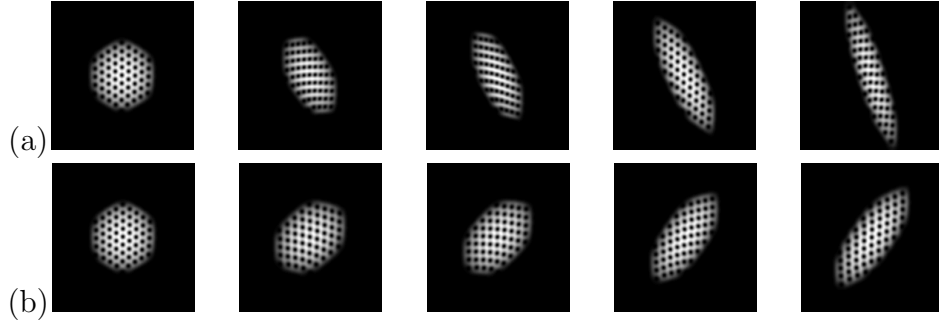


Figure 3.4: Image plots of the density $|\psi(\mathbf{x}, t)|^2$ on $[-18, 18] \times [-18, 18]$ at different times $t=0, 2.0, 4.0, 6.0,$ and 8.0 (from left to right) by changing trapping frequency in x -direction only from $\gamma_x = 1$ to : (a) $\gamma_x = 1.5$; (b) $\gamma_x = 0.75$.

3.3) or expand (c.f. (b) of Figure 3.3) in y -direction since the trap frequency in y -direction is increasing or decreasing at $t = 0$. (ii) Cases III & IV corresponds to changing trapping frequency in x -direction only. Similar results are observed (c.f. (a) and (b) of Figure 3.3). (iii) Cases V & VI corresponds to increasing and decreasing the trapping frequencies in x and y -directions by the same value (i.e., ϵ) respectively [38]. The condensate initially starts to contract and expand in x and y -directions respectively (c.f. Figure 3.5) (iv) We observed the remarkable sheet-like vortices in our numerical results (c.f. Figure 3.3&3.5). One can compare our numerical results with the experimental results in [38] and find very good qualitative agreement. Furthermore, we also found that when ϵ is bigger in Cases V&VI, the

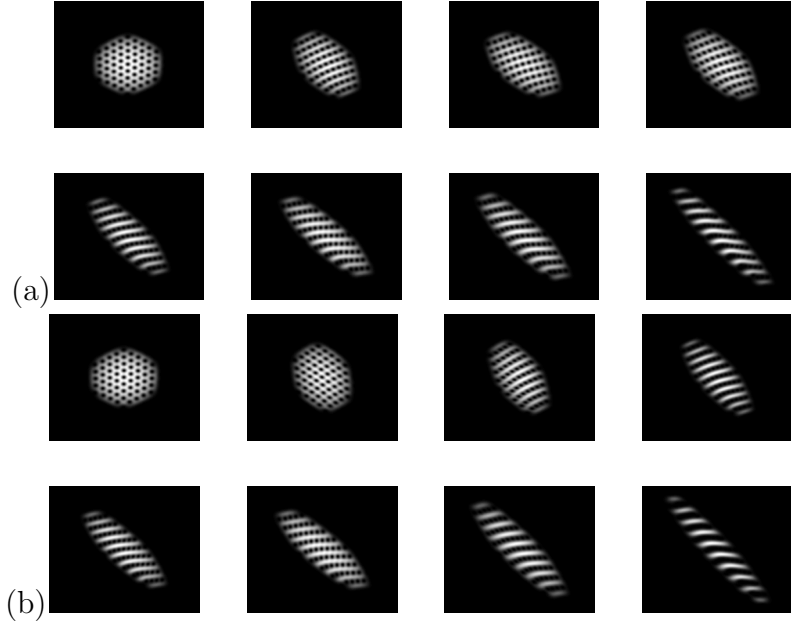


Figure 3.5: Image plots of the density $|\psi(\mathbf{x}, t)|^2$ by changing trapping frequencies at different times from $\gamma_x = 1, \gamma_y = 1$ to $\gamma_x = \sqrt{1 + \epsilon}, \gamma_y = \sqrt{1.0 - \epsilon}$ (a) $\epsilon = 0.2$ for times 0, 2, 3, 4, 5, 6, 7 and 8 (from left to right); (b) $\epsilon = 0.4$ for times $t = 0, 1.0, 1.5, 2.0, 2.5, 3.0, 4.0$ and 4.5.

sheet-like vortices appear up earlier.

3.3.3 Generation of giant vortex in rotating BEC

In this subsection we numerically generate a giant vortex in rotating BEC from its ground state by introducing a localized loss term [122]. This study was motivated by the recent experiment [45] and theoretical study [122] in which the giant vortex formation arises as a dynamics effect.

We take $d = 2, \beta_2 = 100$ and $\Omega = 0.99$ in (3.7). The initial data $\psi_0(\mathbf{x})$ in (3.9) is again chosen as the ground state of (2.10) with $d = 2, \Omega = 0.99, \beta_2 = 100$ and $\gamma_x = \gamma_y = 1$ which is computed numerically by the normalized gradient flow proposed in [13]. The localized loss term in (3.7) is chosen as a Gaussian function

of the form [122]

$$W(x, y) = w_0 e^{-\frac{(x-x_0)^2 + (y-y_0)^2}{r_0^2}}, \quad (3.37)$$

where w_0, x_0, y_0, r_0 are constants. We solve the problem on $\Omega_{\mathbf{x}} = [-24, 24] \times [-24, 24]$ with mesh size $\Delta x = \Delta y = 3/16$ and time step $\Delta t = 0.001$.

From the numerical results shown in Figures 3.6, we can see that the giant vortex lattice is generated due to the dynamic effect in a rotating BEC. The center of the giant vortex is the same as the center of the localized loss term and the size of the giant vortex depends on the values of r_0 and w_0 . One can compare our numerical results with the experimental results in [45] and find very good qualitative agreement.

3.4 Conclusion

We have proposed a new time-splitting Fourier pseudospectral method for computing the dynamics of a rotating BEC based on an efficient approximation of GPE with an angular momentum rotation term. The new method is explicit, unconditionally stable, and of spectral accuracy in space and second order in time. It is time reversible and time transverse invariant in the discretized level, just as the original GPE is. The efficient and accurate numerical method was applied to study dynamics of a quantized vortex lattice in rotating BEC. In Chapter 4, we extend this new numerical method to solve coupled GPEs for the dynamics of rotating two-component BECs. In Chapter 5, we extend the method to solve the generalized GPEs for studying spinor F=1 dynamics in a rotational frame.

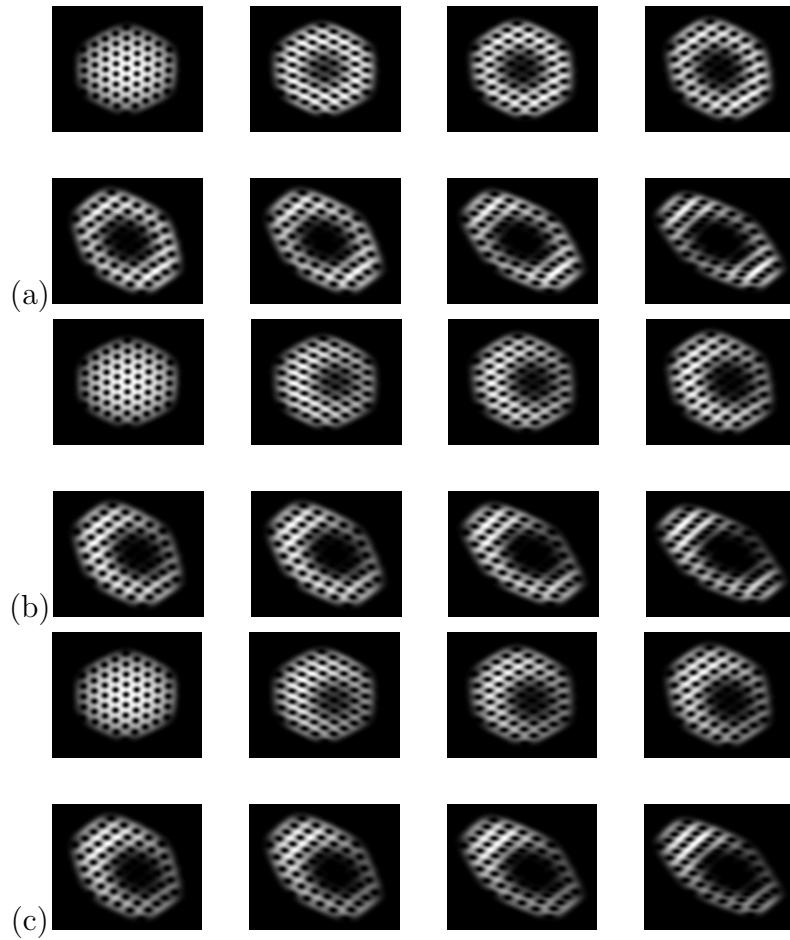


Figure 3.6: Image plots of the density $|\psi(\mathbf{x}, t)|^2$ on $[-12, 12] \times [-12, 12]$ at different times $t=0, 0.5, 0.75, 1.0, 1.25, 1.5, 1.75,$ and 2.0 with $w_0 = 1$ and $r_0 = \frac{\sqrt{7}}{2}$ in the equation (3.37) for generating giant vortices (a) $x_0 = 0, y_0 = 0$; (b) $x_0 = 1.5, y_0 = 0$; (c) $x_0 = 1.5, y_0 = 1$.

Applications to rotating two-component BEC

Motivated by recent experimental work on creating vortices in rotating two component trapped Bose-Einstein condensates performed in the JILA group [91], theoretically a mathematical model, the time-independent coupled GPEs with an angular momentum rotational term, is proposed to describe the equilibrium structure of rotating two-component BEC [59, 60, 74, 98]. These equations could be obtained as stationary solutions of time-dependent coupled GPEs, or derived by minimizing the total energy of the system. There are many solutions to the time-independent coupled GPEs, among which the ground state, symmetric state and central vortex state are perhaps of most interest. For the time-independent coupled GPEs without the angular momentum rotational term, by solving them numerically or analytically, many aspects of binary condensate mixtures, such as spontaneous symmetry breaking [47], ground state [10, 30, 105, 110, 129], central vortex structures [35, 58, 64, 103, 131], stable skyrmions [21] and condensate dynamics [97, 111, 124] can be used to predict results for various experimental setups.

For the numerical works on time-independent coupled GPEs with the angular momentum rotational term, Kasamatsu et. al [74] focused on finding ground state for BEC with equal intra-component and inter-component interactions. By changing

the ratio between intra-component and inter-component coupling constants they revealed a rich vortex phase diagram for the ground state solution, but no numerical results were reported for the nonequal intra-component interactions. García-Ripoll et al. [59] searched the ground state for rotating two-component BEC in the JILA experimental setup but focused on Josephson coupling effects. Mueller et al. [98] studied theoretically the rotating two-component BEC by assuming that the wave functions were an expansion of the Landau functions. They also found a rich vortex phase diagram. It was pointed out that when each component had different particle number or nonequal intra-component interaction, the ground state might have a different vortex phase diagram, which is not yet verified.

Since the experimental observation of quantized vortices in alkali atomic BEC [1, 50, 63, 87, 91], there has been a growing interest in studying the dynamics related to quantized vortices in rotating two-component BEC. Under the mean field approximation, the time-dependent coupled GPEs with a coupling term have been proposed to describe the dynamics of rotating two-component BEC such as those of ^{87}Rb atoms at a ultra-low temperature [59, 77, 96, 134, 135]. A numerical study of the time-dependent coupled GPEs will be interesting as it may shed light on some time-evolution properties of the rotating two-component BEC. For example, Williams [135] has shown how to prepare the topological modes through numerical simulation. Kasamatsu et al. [76] have numerically studied the dynamical formation of vortex lattice. Schweikhard et al. [117] have studied vortex lattice dynamics experimentally and compared it with simulation results. They found qualitative agreement between experiment results and simulations.

In this chapter, first we extend the GFDN method for rotating one-component BEC to study the stationary quantized vortex states for the rotating two-component BEC. Our focus is to compute the ground state solution of rotating two-component BEC with a relevant experiment setup, i.e., having either nonequal particle number for each component or nonequal intra-component interactions. We will also search the symmetric state and central vortex states for the two-component BEC and find

their energy diagrams, from which we report the critical velocity.

Next we extend the TSSP method for the single GPE to solve the coupled GPEs with a coupling term so as to study the complicated dynamics of quantized vortices in the rotating two-component BEC.

This chapter is organized as follows. In section 4.1, we take the three-dimensional time-dependent GPEs with an angular momentum rotational term, rescale it and reduce it to a two-dimensional problem in a limiting regime. In section 4.2, we present the minimization problem for ground state, symmetric and central vortex states and briefly introduce the numerical method to compute them. Numerical results for the stationary states of the rotating two-component BEC are described in detail. In section 4.3, we present some analytical properties of the coupled GPEs. We describe the TSSP method for the coupled GPEs with a coupling term and apply the method to study the generation of topological modes and the vortex lattice dynamics in the rotating two-component BEC. Some conclusions are made in section 4.4.

4.1 The time-dependent coupled GPEs

The mathematical model for describing the time evolution of rotating two-component BEC is the following coupled GPEs with an angular momentum rotational term [76]

$$i\hbar \frac{\partial \psi_j}{\partial t} = \left(-\frac{\hbar^2}{2m_j} \nabla^2 + V_j(\mathbf{x}) - \hbar\Omega L_z + g_{j1}|\psi_1|^2 + g_{j2}|\psi_2|^2 \right) \psi_j, \quad j = 1, 2, \quad (4.1)$$

where $\psi_j = \psi_j(\mathbf{x}, t)$ are the wave functions of the two components. The wave function is normalized as

$$\int_{\mathbb{R}^3} |\psi_j(\mathbf{x}, t)| d\mathbf{x} = N_j, \quad (4.2)$$

where N_j is the particle number of component j , m_j is the atomic mass of component j and the harmonic trapping potential $V_j(\mathbf{x}) = \frac{m_j}{2}(\omega_{x,j}^2 x^2 + \omega_{y,j}^2 y^2 + \omega_{z,j}^2 z^2)$. The intra-component and inter-component atomic interactions are represented as $g_{jj} = 4\pi\hbar^2 a_{jj}/m_j$ ($j=1,2$) and $g_{12} = g_{21} = 2\pi\hbar^2 a_{12}(m_1 + m_2)/(m_1 m_2)$ with a_{jj} ($j=1,2$)

being the s-wave scattering length of component j and a_{12} between components 1 and 2. The energy of the system is

$$E(\psi_1, \psi_2) = \int_{\mathbb{R}^3} \sum_{j=1}^2 \left[\frac{\hbar^2}{2m_j} |\nabla \psi_j(\mathbf{x}, t)|^2 + V_j(\mathbf{x}) |\psi_j(\mathbf{x}, t)|^2 - \Omega \bar{\psi}_j(\mathbf{x}, t) L_z \psi_j(\mathbf{x}, t) + \frac{1}{2} (g_{j1} |\psi_1(\mathbf{x}, t)|^2 + g_{j2} |\psi_2(\mathbf{x}, t)|^2) |\psi_j(\mathbf{x}, t)|^2 \right] d\mathbf{x}. \quad (4.3)$$

4.1.1 Dimensionless coupled GPEs

For convenience, we scale the equations (4.1) into its dimensionless form. We introduce

$$\tilde{t} = \omega_{x,1} t, \quad \tilde{\mathbf{x}} = \frac{\mathbf{x}}{c_0}, \quad \tilde{\psi}_j(\tilde{\mathbf{x}}, \tilde{t}) = \frac{c_0^{3/2}}{\sqrt{N_j}} \psi_j(\mathbf{x}, t), \quad \tilde{\Omega} = \frac{\Omega}{\omega_{x,1}}, \quad c_0 = \sqrt{\frac{\hbar}{m_1 \omega_{x,1}}}. \quad (4.4)$$

In fact, here we choose $1/\omega_{x,1}$ and c_0 as the dimensionless time and length units, respectively. Plugging (4.4) into (4.1), multiplying by $\frac{1}{m_1 \omega_{x,1}^2 (N_j c_0)^{1/2}}$ to the j th ($j = 1, 2$) equation, and then removing all \sim , we obtain the following dimensionless GPEs in 3D

$$i \frac{\partial \psi_j(\mathbf{x}, t)}{\partial t} = \left(-\frac{m_1}{2m_j} \nabla^2 - \Omega L_z + V_j(\mathbf{x}) + \sum_{l=1}^2 \beta_{jl} |\psi_l|^2 \right) \psi_j(\mathbf{x}, t), \quad j = 1, 2, \quad (4.5)$$

where

$$V_j(\mathbf{x}) = \frac{m_j}{2m_1} (\gamma_{x,j}^2 x^2 + \gamma_{y,j}^2 y^2 + \gamma_{z,j}^2 z^2),$$

$$\gamma_{x,j} = \frac{\omega_{x,j}}{\omega_{x,1}}, \quad \gamma_{y,j} = \frac{\omega_{y,j}}{\omega_{x,1}}, \quad \gamma_{z,j} = \frac{\omega_{z,j}}{\omega_{x,1}},$$

$$\beta_{jl} = \frac{g_{jl} N_l}{c_0^3 \hbar \omega_{x,1}} = \frac{2\pi a_{jl} N_l (m_j + m_l) m_1}{c_0 m_j m_l}, \quad j, l = 1, 2.$$

4.1.2 Reduction to two dimensions

Similar as what we have done for the rotating one-component BEC, when $\gamma_{y,j} \approx \gamma_{x,1}$ and $\gamma_{z,j} \gg \gamma_{x,1}$ ($j=1,2$), the three-dimensional coupled GPEs (4.5) can approximately be reduced to two-dimensional coupled ones (see the subsection 2.1.2). The

three-dimensional and two-dimensional coupled GPEs can be written in a unified form:

$$i \frac{\partial}{\partial t} \psi_j(\mathbf{x}, t) = \left(-\frac{m_1}{2m_j} \nabla^2 - \Omega L_z + V_j(\mathbf{x}) + \sum_{l=1}^2 \beta_{jl} |\psi_l|^2 \right) \psi_j(\mathbf{x}, t), \quad (4.6)$$

where the trap potentials

$$V_j(\mathbf{x}) = \begin{cases} \frac{m_j}{2m_1} (\gamma_{x,j}^2 x^2 + \gamma_{y,j}^2 y^2), & d = 2, \\ \frac{m_j}{2m_1} (\gamma_{x,j}^2 x^2 + \gamma_{y,j}^2 y^2 + \gamma_{z,j}^2 z^2), & d = 3. \end{cases}$$

The intra-component interactions and inter-component interactions are now represented by the constants β_{jl} ($j, l = 1, 2$) respectively.

Two important invariants of (4.6) are the normalization of the wave function of component j

$$N_j(\psi_j(\mathbf{x}, t)) = \int_{\mathbb{R}^d} |\psi_j(\mathbf{x}, t)|^2 d\mathbf{x} = 1, \quad t \geq 0, \quad j = 1, 2, \quad (4.7)$$

and the energy per particle

$$E_\beta(\psi_1, \psi_2) = \sum_{j=1}^2 \frac{N_j}{N} \int_{\mathbb{R}^d} \left[\frac{m_1}{2m_j} |\nabla \psi_j|^2 + V_j(\mathbf{x}) |\psi_j|^2 - \Omega \bar{\psi}_j L_z \psi_j + \frac{1}{2} \sum_{l=1}^2 \beta_{jl} |\psi_l|^2 |\psi_j|^2 \right] d\mathbf{x}, \quad (4.8)$$

where $\beta = \max_{1 \leq j, l \leq 2} |\beta_{jl}|$.

4.1.3 Semiclassical scaling

When $\beta \gg 1$, i.e. the two components are in a strongly repulsive interacting condensation or in a semiclassical regime, another scaling for the coupled GPEs (4.6) is also very useful in practice. We choose $\mathbf{x} = \tilde{\mathbf{x}} \varepsilon^{-\frac{1}{2}}$ and $\psi_j(\mathbf{x}) = \varepsilon^{\frac{d}{4}} \psi_j^\varepsilon(\tilde{\mathbf{x}})$ with $\varepsilon = \beta^{-\frac{2}{d+2}}$, removing all \sim again, we obtain

$$i\varepsilon \frac{\partial}{\partial t} \psi_j^\varepsilon(\mathbf{x}, t) = \left(-\frac{\varepsilon^2 m_1}{2m_j} \nabla^2 - \varepsilon \Omega L_z + V_j(\mathbf{x}) + \sum_{l=1}^2 f_{jl} |\psi_l^\varepsilon|^2 \right) \psi_j^\varepsilon(\mathbf{x}, t), \quad (4.9)$$

where $f_{jl} = \beta_{jl}/\beta$. The energy functional related to the equation (4.9) becomes,

$$E_\varepsilon(\psi_1^\varepsilon, \psi_2^\varepsilon) = \sum_{j=1}^2 \frac{N_j}{N} \int_{\mathbb{R}^d} \left[\frac{m_1}{2m_j} \varepsilon^2 |\nabla \psi_j^\varepsilon|^2 + V_j(\mathbf{x}) |\psi_j^\varepsilon|^2 - \varepsilon \Omega \bar{\psi}_j^\varepsilon L_z \psi_j^\varepsilon + \frac{1}{2} \sum_{l=1}^2 f_{jl} |\psi_l^\varepsilon|^2 |\psi_j^\varepsilon|^2 \right] d\mathbf{x}. \quad (4.10)$$

From the formula (4.10) and $E_\beta(\psi_1, \psi_2) = \varepsilon^{-1} E_\varepsilon(\psi_1^\varepsilon, \psi_2^\varepsilon)$, we know easily that $E_\beta(\psi_1, \psi_2) \sim O(\varepsilon^{-1}) = O(\beta^{\frac{2}{d+2}})$. Our numerical results in the subsection 4.2.4 confirm this asymptotic results (c.f. Figure 4.7).

4.2 Stationary states

To find a stationary state, or a stationary solution of (4.6), we write

$$\psi_j(\mathbf{x}, t) = e^{-i\mu_j t} \phi_j(\mathbf{x}), \quad j = 1, 2, \quad (4.11)$$

where μ_j is the chemical potential of the j component and ϕ_j is independent of time. Inserting (4.11) into (4.6) gives the following time-independent GPEs for $\phi_j(\mathbf{x})$

$$\mu_j \phi_j(\mathbf{x}) = \left(-\frac{m_1}{2m_j} \nabla^2 - \Omega L_z + V_j(\mathbf{x}) + \sum_{l=1}^2 \beta_{jl} |\phi_l(\mathbf{x})|^2 \right) \phi_j(\mathbf{x}), \quad (4.12)$$

under the normalization condition for each component.

$$\int_{\mathbb{R}^d} |\phi_j(\mathbf{x})|^2 d\mathbf{x} = 1, \quad j = 1, 2. \quad (4.13)$$

This is a nonlinear eigenvalue problem with two constraints and its eigenvalue μ_j can be computed from its corresponding eigenfunction $\phi_j(\mathbf{x})$ by

$$\begin{aligned} \mu_j &= \mu_j(\phi_1, \phi_2) \\ &\equiv \int_{\mathbb{R}^d} \sum_{j=1}^2 \left[\frac{m_1}{2m_j} |\nabla \phi_j|^2 + V_j |\phi_j|^2 - \Omega \bar{\phi}_j L_z \phi_j + \sum_{l=1}^2 \beta_{jl} |\phi_l|^2 |\phi_j|^2 \right] d\mathbf{x}. \end{aligned}$$

4.2.1 Ground state

The ground state solution $\Phi^g(\mathbf{x}) := (\phi_1^g(\mathbf{x}), \phi_2^g(\mathbf{x}))$ of rotating two-component BEC is found by minimizing the energy $E_\beta(\phi_1, \phi_2)$ over the set $\mathbf{U} = \{\Phi = (\phi_1, \phi_2) \mid E_\beta(\phi_1, \phi_2) < \infty, \int_{\mathbb{R}^d} |\phi_j(\mathbf{x})|^2 d\mathbf{x} = 1, \quad j = 1, 2\}$, i.e.,

Find $(\mathcal{U}^g = (\mu_1^g, \mu_2^g), \Phi^g = (\phi_1^g, \phi_2^g) \in \mathbf{U})$ such that

$$\begin{aligned} E_\beta(\Phi^g) &= \min_{\Phi \in \mathbf{U}} E_\beta(\phi_1, \phi_2), \\ \mu_j^g &= \mu_j(\phi_1^g, \phi_2^g). \end{aligned}$$

It is very easily to see that (\mathcal{U}^g, Φ^g) is a solution of nonlinear eigenvalue problem (4.12) under the constraints (4.13). Seiringer et al. have proved that the existence of the ground state solution [118] when $\beta_{jl} \geq 0, j, l = 1, 2$ and $\Omega < \Omega_a$ (Ω_a is some constant).

In addition, there are many other solutions to (4.12) under the constraints (4.13) except for ground state solutions. Any eigenfunction pair $(\phi_1(\mathbf{x}), \phi_2(\mathbf{x}))$ of (4.12) under the constraints (4.13) whose energy greater than $E_\beta(\phi_1^g, \phi_2^g)$ is usually called as an excited state in the physics literature. In the following subsection we are interested in finding symmetric states and central vortex states.

4.2.2 Symmetric and central vortex states

For simplification, here we only present the symmetric and central vortex states in 2D. For radially symmetric trap (i.e., $V_j = \frac{m_j}{2m_1} \gamma_{r,j}^2 r^2$ where $\gamma_{r,j} = \gamma_{x,j} = \gamma_{y,j}$). We may assume each wave function of the two-component BEC to be the eigen-states of the L_z operator [58, 131, 135], i.e., $\phi_j(\mathbf{x})$ may be written as $\phi_j(r) \exp(i\kappa_j\theta)$ (κ_j is an integer, $j=1,2$). $\kappa_j = 0$ corresponds to symmetric state, while $\kappa_j \neq 0$ corresponds to central vortex state. We therefore substitute the ansatz $\phi_j(x, y) = \phi_j(r) \exp(i\kappa_j\theta)$ into (4.12) and obtain the equation for ϕ_j ,

$$\left(-\frac{m_1}{2m_j r} \frac{\partial}{\partial r} \left(r \frac{\partial}{\partial r} \right) + \frac{m_j}{2m_1} \frac{\kappa_j^2}{r^2} + V_j(r) + \sum_{l=1}^2 \beta_{jl} \phi_l^2 - \mu_j \right) \phi_j(r) = 0, \quad (4.14)$$

where μ_1 and μ_2 are determined through the constraint

$$2\pi \int_0^\infty \phi_j^2(r) r dr = 1, \quad j = 1, 2. \quad (4.15)$$

To find the stationary symmetric state and central vortex state in 2D, we may solve the following minimization problem:

For given κ_1, κ_2 , find $(\mu_1^c, \mu_2^c, \Phi_{\kappa_1, \kappa_2} = (\phi_1^{\kappa_1}(r), \phi_2^{\kappa_2}(r)) \in V_\kappa)$ such that

$$\begin{aligned} E_\beta(\Phi_{\kappa_1, \kappa_2}) &= \min_{\phi=(\phi_1, \phi_2) \in V_\kappa} E_\beta(\phi_1 \exp(i\kappa_1\theta), \phi_2 \exp(i\kappa_2\theta)), \\ \mu_j^c &= \mu_j(\phi_1(r) \exp(i\kappa_1\theta), \phi_2(r) \exp(i\kappa_2\theta)), \end{aligned}$$

where

$$\begin{aligned} V_\kappa &= \{ \phi = (\phi_1(r), \phi_2(r)) \mid E_\beta(\phi_1(r) \exp(i\kappa_1\theta), \phi_2(r) \exp(i\kappa_2\theta)) < \infty, \\ &2\pi \int_0^\infty |\phi_j(r)|^2 r dr = 1, \quad j = 1, 2 \}. \end{aligned}$$

For the symmetric and central vortex states in 3D, we substitute $\phi_j(\mathbf{x}) = \phi_j(r, z) \exp(i\kappa_j\theta)$ into (4.12) and can obtain similar equations as (4.14) and similar minimization problem as above.

4.2.3 Numerical methods for stationary states

In this subsection, we briefly explain the method for computing ground state. In fact we extend the method for computing the stationary states of rotating one-component BEC to compute those of rotating two-component BEC. To do this, we consider the following GFDN:

$$\frac{\partial \phi_j}{\partial t} = \left[\frac{m_1}{2m_j} \nabla^2 - V_j(\mathbf{x}) - \sum_{l=1}^2 \beta_{jl} |\phi_l|^2 + \Omega L_z \right] \phi_j, \quad t_n \leq t < t_{n+1}, \quad (4.16)$$

$$\phi_j(\mathbf{x}, t_{n+1}) \doteq \phi_j(\mathbf{x}, t_{n+1}^+) = \frac{\phi_j(\mathbf{x}, t_{n+1}^-)}{\|\phi_j(\mathbf{x}, t_{n+1}^-)\|}, \quad (4.17)$$

$$\phi_j(\mathbf{x}, t_{n+1}) = 0, \quad \mathbf{x} \in \Gamma = \partial\Omega_x, \quad (4.18)$$

$$\phi_j(\mathbf{x}, 0) = \phi_{j,0}(\mathbf{x}), \quad \mathbf{x} \in \Omega_x, \quad \int_{\Omega_x} |\phi_{j,0}(\mathbf{x})|^2 d\mathbf{x} = 1, \quad (4.19)$$

where $j=1,2$ and $\phi_j(\mathbf{x}, t_n^\pm) = \lim_{t \rightarrow t_n^\pm} \phi_j(\mathbf{x}, t)$.

By doing similar proof as what we have done in the chapter 2, the above GFDN is equivalent to evolve the following CNGF:

$$\frac{\partial \phi_j}{\partial t} = \frac{m_1}{2m_j} \nabla^2 \phi_j - V_j(\mathbf{x}) \phi_j - \sum_{l=1}^2 \beta_{jl} |\phi_l|^2 \phi_j + \Omega L_z \phi_j + \mu_\Phi^j \phi_j, \quad (4.20)$$

$$\phi_j(\mathbf{x}, t) = 0, \quad \mathbf{x} \in \Gamma, \quad j = 1, 2, \quad (4.21)$$

$$\phi_j(\mathbf{x}, 0) = \phi_{j,0}(\mathbf{x}), \quad \mathbf{x} \in \Omega_x, \quad \int_{\Omega_x} |\phi_{j,0}(\mathbf{x})|^2 d\mathbf{x} = 1, \quad (4.22)$$

where

$$\mu_{\Phi}^j = \frac{1}{\|\phi_j(\cdot, t)\|^2} \int_{\Omega_{\mathbf{x}}} \left[\frac{m_1}{2m_j} |\nabla \phi_j|^2 + V_j |\phi_j|^2 + \sum_{l=1}^2 \beta_{jl} |\phi_l|^2 |\phi_j|^2 - \Omega \bar{\phi}_j L_z \phi_j \right] d\mathbf{x},$$

with $\Phi = (\phi_1(\mathbf{x}, t), \phi_2(\mathbf{x}, t))$. For the CNGF, we have the following theorem:

Theorem 4.2.1 *Suppose $V_j(\mathbf{x}) \geq 0$ for all $\mathbf{x} \in \mathbb{R}^d$, $\beta_{jl} \geq 0$ ($j, l=1, 2$) with $\beta_{12} = \beta_{21}$ and $\|\phi_{j,0}\| = 1$ ($j=1, 2$). Then the CNGF (4.20)-(4.22) is normalization conserving and energy diminishing, i.e.,*

$$\begin{aligned} \|\phi_j(\cdot, t)\|^2 &= \int_{\mathbb{R}^d} |\phi_j(\mathbf{x}, t)|^2 d\mathbf{x} = \|\phi_{j,0}\|^2 = 1, \quad t \geq 0, \\ \frac{d}{dt} E_{\beta}(\phi_1(\cdot, t), \phi_2(\cdot, t)) &= -2 \sum_{j=1}^2 \left\| \frac{\partial \phi_j}{\partial t}(\cdot, t) \right\|^2 \leq 0, \quad t \geq 0, \end{aligned}$$

which in turn implies

$$E_{\beta}(\phi_1(\cdot, t_1), \phi_2(\cdot, t_1)) \geq E_{\beta}(\phi_1(\cdot, t_2), \phi_2(\cdot, t_2)), \quad 0 \leq t_1 \leq t_2 < \infty.$$

Proof: Follows the proofs presented in the section 2.3 of Chapter 2.

From this theorem, when the initial data are chosen appropriately, the ground state solution ϕ_j^g and its corresponding chemical potential μ_j^g ($j=1, 2$) can be obtained from the steady state solution of the GFDN (4.16)-(4.19) or the CNGF (4.20)-(4.22). In our numerical calculations, we choose the initial data as a linear combination of the ϕ_{ho} and ϕ_{ho}^v . We discretize the equations (4.16) in space by finite difference and in time by backward Euler method. The obtained discretization equations will be solved by standard iterative methods. Detailed algorithm can be derived from those presented in chapter 2 for the rotating one-component BEC.

4.2.4 Numerical results for the stationary states

In this subsection we report numerical results for ground state, symmetric state and central vortex states of rotating two-component BEC. Because a mixture of spin states of ^{87}Rb and a mixture of spin states of ^{23}Na is realized in JILA [63] and in

MIT [92] respectively, in all calculations we assume $m_1 = m_2$ and $N_1 = N_2$ (except that $N_1 : N_2 = 10 : 1$ in Example 4.3), and consider three cases of inter-component and intra-component interactions: case I, $\beta_{11} : \beta_{12} : \beta_{21} : \beta_{22} = \beta_2 \times (1 : \delta : \delta : 1)$ [74] [75]; case II, $\beta_{11} : \beta_{12} : \beta_{21} : \beta_{22} = \beta_2 \times (1.03 : 0.97 : 0.97 : 1)$ with β_2 being some constant [91] and case III, $\beta_{11} = 100$, $\beta_{12} = \beta_{21} = 94$, and $\beta_{22} = 97$ [63]. The problem is solved in the domain $\Omega_{\mathbf{x}} = [-6, 6] \times [-6, 6]$. The trap potential $V_1(x, y) = V_2(x, y) = \frac{1}{2}(x^2 + y^2)$. The initial conditions for the equations (4.16) is $\phi_{j,0} = \frac{(1 - \Omega)\phi_{\text{ho}}(x, y) + \Omega\phi_{\text{ho}}^v(x, y)}{\|(1 - \Omega)\phi_{\text{ho}}(x, y) + \Omega\phi_{\text{ho}}^v(x, y)\|}$, $(x, y) \in \Omega_{\mathbf{x}}$ ($j=1,2$).

Example 4.1 Ground state in 2D with case I for different Ω and $\beta_2 = 100$. Figure 4.1 shows that in the ground state when $\delta = 0.7$, each component contain identical vortex lattices, with one lattice displaced relative to each other, which confirms the predictions made by Muller et al. [98]. Figure 4.2 shows that in the ground state when $\delta = 1.1 > 0$, each component has the vortex stripe with same number of vortices; these agree with the numerical results obtained by Kasamatsu et al. [74]. We can also observe that the vortex number is growing larger and larger as Ω increases.

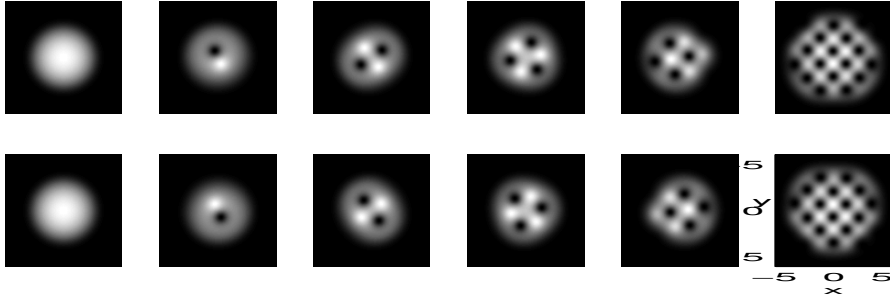


Figure 4.1: Image plots of the ground state density $|\phi_j^g(x, y)|^2$ for $\Omega = 0, 0.4, 0.47, 0.5, 0.6, 0.9$ respectively, upper row for $|\phi_1^g(x, y)|^2$, low row for $|\phi_2^g(x, y)|^2$. Case I with $\delta = 0.7$ in Example 4.1.

Example 4.2 Ground state in 2D with case II and case III for different Ω and $\beta_2 = 100$. Figure 4.3 (for case II) and Figure 4.4 (for case III) show numerical results for the ground state with different Ω . From these results we find when $\beta_{11} \neq \beta_{22}$, in

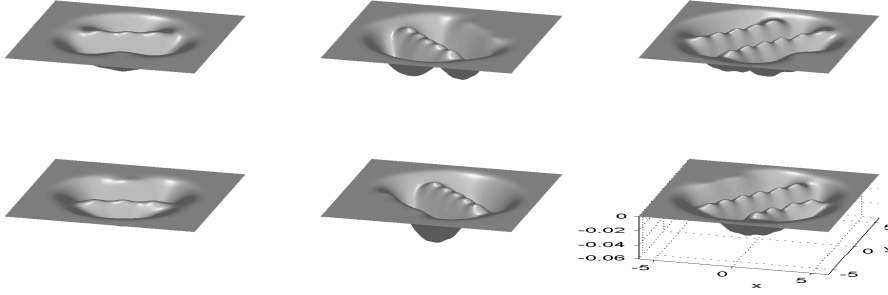


Figure 4.2: Surface plots of the ground state density $-\left|\phi_j^g(x, y)\right|^2$ for $\Omega = 0.5, 0.7, 0.8$ respectively. Upper row for $-\left|\phi_1^g(x, y)\right|^2$, low row for $-\left|\phi_2^g(x, y)\right|^2$. Case I with $\delta = 1.1$ in Example 4.1.

the ground state, the two components, even though they have equal inter-component interactions, may not contain an equal number of vortices, these results however, is different from the predictions made by Muller et al. [98].

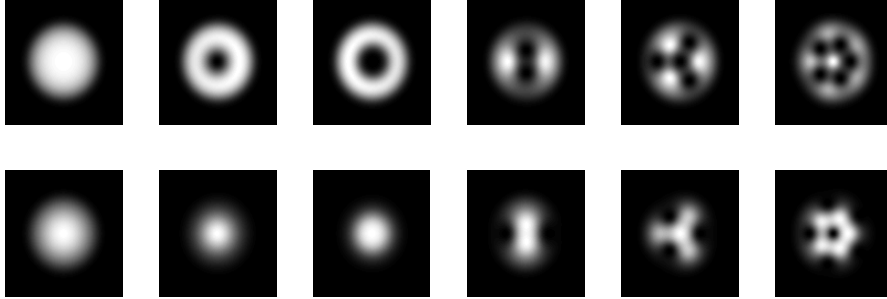


Figure 4.3: Image plots of ground state density $\left|\phi_j^g(x, y)\right|^2$ for $\Omega = 0, 0.2, 0.3, 0.4, 0.5, 0.6$ respectively. Upper row for $\left|\phi_1^g(x, y)\right|^2$, low row for $\left|\phi_2^g(x, y)\right|^2$. Case II in Example 4.2 .

Example 4.3 Ground state in 2D for different Ω and the interaction constants being $\beta_{11} = 1030$, $\beta_{12} = 100$, $\beta_{21} = 1000$, and $\beta_{22} = 970$. Figure 4.5 shows that in the ground state, a sharp different vortex structure is observed in the two components: the first component have vortices at which the second component have peaks.

Example 4.4 Energy diagrams for the ground state, symmetric state and central vortex states in 2D with case II. We let $\beta_2 = 0, 10, 100, 1000$ respectively and Ω change from 0 to 1. We take $E^g = E_\beta(\Phi_g)$, $E^{0,0} = E_\beta(\Phi_{0,0})$, $E^{0,1} = E_\beta(\Phi_{0,1})$, $E^{1,1} =$

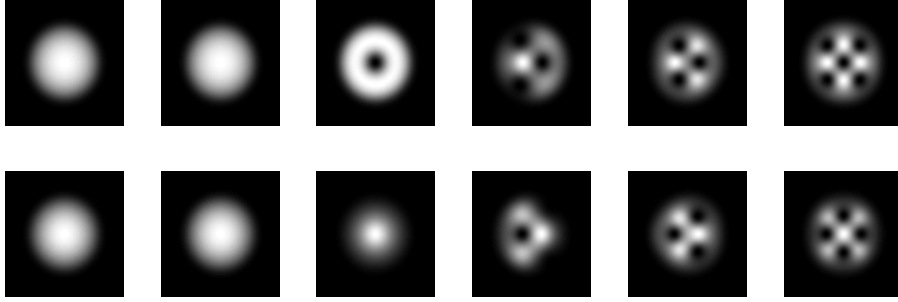


Figure 4.4: Image plots of the ground state density $|\phi_j^g(x, y)|^2$ for $\Omega = 0, 0.2, 0.3, 0.4, 0.5, 0.6$ respectively. Upper row for $|\phi_1^g(x, y)|^2$, low row for $|\phi_2^g(x, y)|^2$.

Case III in Example 4.2.

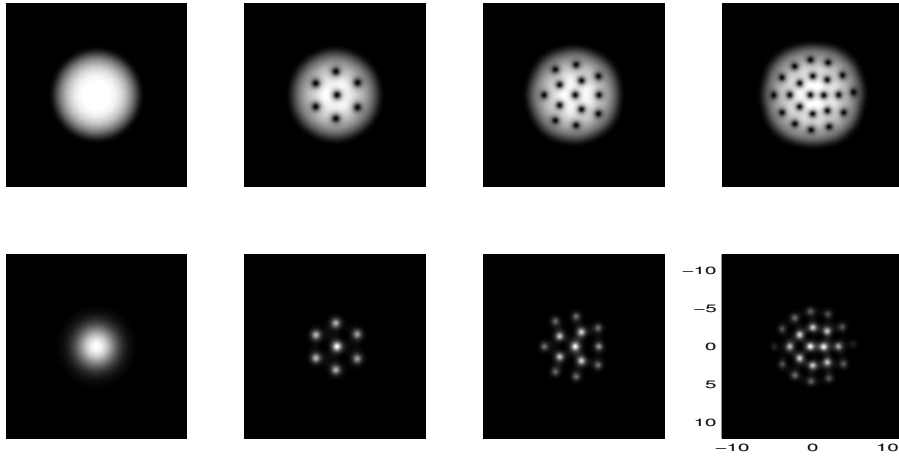


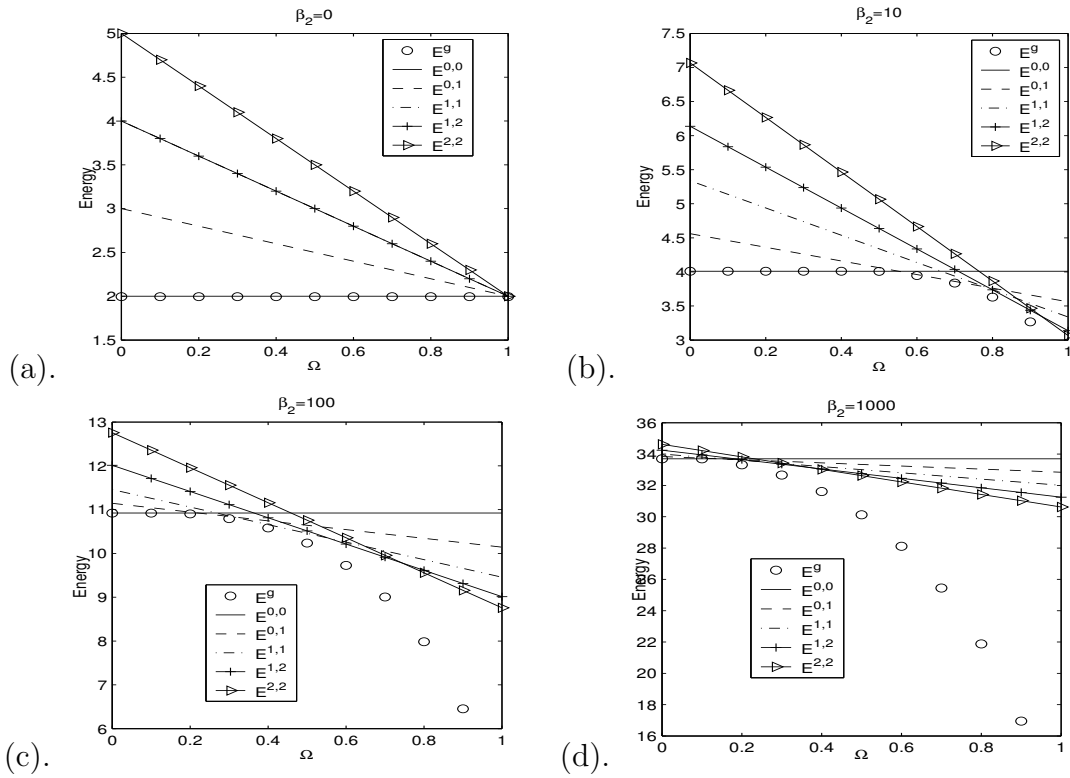
Figure 4.5: Image plots of the ground state density $|\phi_j(x, y)|^2$ for $\Omega = 0.0, 0.4, 0.6, 0.8$ respectively in Example 4.3. Upper row for $|\phi_1^g(x, y)|^2$, low row for $|\phi_2^g(x, y)|^2$.

$E_\beta(\Phi_{1,1})$, $E^{1,2} = E_\beta(\Phi_{1,2})$, and $E^{2,2} = E_\beta(\Phi_{2,2})$ in Figure 4.6. From the energy diagrams for different β_2 and Ω shown in Figure 4.6, we can report the following critical angular velocity at which the ground state solutions lose symmetry (c.f. Table 4.1). The critical angular velocity at which the ground state lose symmetry is defined as $\Omega_c = \max\{\Omega, E_\beta(\Phi^g) = E_\beta(\Phi_{0,0})\}$. From Table 4.1, we can see that: (a) the critical frequency are decreasing when the particle number of each component are increasing (c.f. Table 4.1); (b) $\Omega^c = 1$ when $\beta_2 = 0$ and $0 < \Omega^c < 1$. Furthermore, from Figure 4.7, we find that $E^g \sim O(\beta_2^{\frac{1}{2}}) \sim O(\beta_2^{\frac{1}{2}})$ for fixed Ω , which agrees well

β_2	0	10	100	1000
Ω_c	1.0	0.57	0.23	0.11

Table 4.1: Critical angular velocity for rotating two-component BEC in 2D.

with the leading asymptotics of the energy obtained from the semiclassical scaling presented in section 4.1.3.

Figure 4.6: Energy diagram for ground state, symmetric state and central vortex states with respect to different Ω in Example 4.4.

Example 4.5 Symmetric states and central vortex states in 2D with case II for different β_2 respectively. Figure 4.8 (a) shows that both components have the symmetric state; Figure 4.8 (b) shows that 1st component have the symmetric state, while the 2nd component have the central vortex states with vorticity 1. Figure 4.9 (a) and 4.9 (b) show that both components have the central vortex states with vorticities (1,1) and (1,2) respectively. From Figure 4.8 and Figure 4.9, we can see

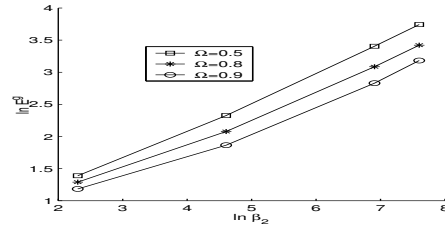


Figure 4.7: Energy diagram for ground state with respect to different β_2 in Example 4.4.

that: (a) the peak of density $|\phi_j(r)|^2$ is decreasing when β_2 is increasing (i.e. particle number of each component is increasing); (b) the density profile of each component does not depend on the rotating frequency Ω .

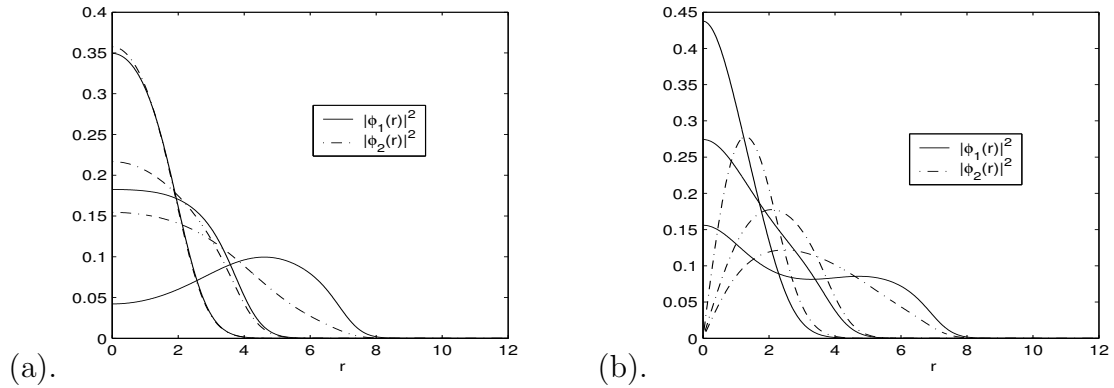


Figure 4.8: (a) Symmetric states are in both components; (b) symmetric state is in the 1st component, central vortex state with vorticity 1 is in the 2nd component for $\beta_2 = 10, 100, 1000$ respectively (in the order of decreasing of peak).

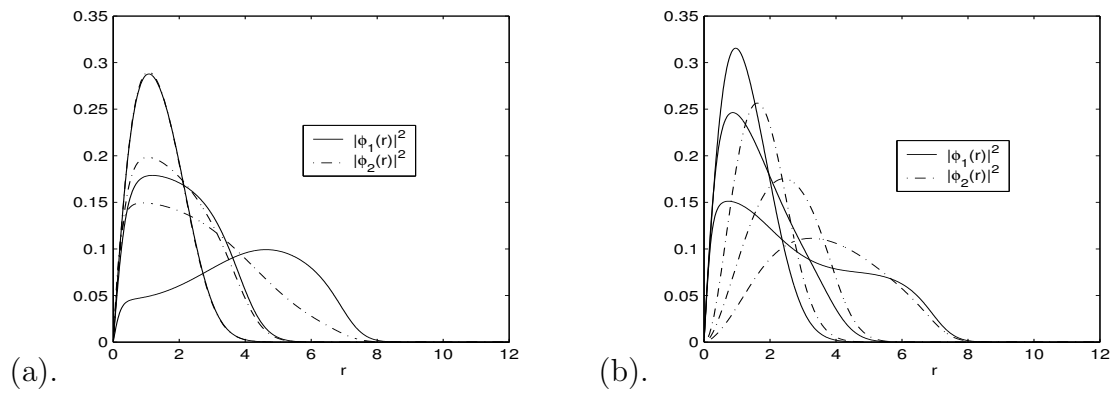


Figure 4.9: (a) Central vortex states with vorticity 1 are in both components; (b) central vortex state with vorticity 1 is in the 1st component, central vortex state with vorticity 2 is in the 2nd component for $\beta_2 = 10, 100, 1000$ respectively (in the order of decreasing of peak) .

4.3 Dynamics of rotating two-component BEC

To study the dynamics for the rotating two-component BEC numerically, we consider the following dimensionless coupled GPEs with a coupling term

$$i \frac{\partial}{\partial t} \psi_j(\mathbf{x}, t) = \left(-\frac{1}{2} \nabla^2 - \Omega L_z + V_j(\mathbf{x}) + \sum_{l=1}^2 \beta_{jl} |\psi_l|^2 \right) \psi_j(\mathbf{x}, t) - \lambda \psi_{k_j}, \quad (4.23)$$

where the coupling term λ describes an internal Josephson coupling induced by an external driving field [59, 77, 133]. $k_j = 2$ when $j = 1$; $k_j = 1$ when $j = 2$.

4.3.1 Some properties of the coupled GPEs

In this subsection, we present some analytical properties of the coupled GPEs (4.23), which will be used to test our new numerical method proposed in the next subsection.

When $\lambda = 0$, the normalization of each wave function is conserved, i. e.,

$$N_j(\psi_j(\mathbf{x}, t)) = N_j(\psi_j(\mathbf{x}, 0)), \quad t \geq 0, \quad j = 1, 2; \quad (4.24)$$

when $\lambda \neq 0$, the normalization of each wave function is not conserved, however, the total normalization of the two wave functions is conserved, i.e.,

$$N_1(\psi_1(\mathbf{x}, t)) + N_2(\psi_2(\mathbf{x}, t)) = N_1(\psi_1(\mathbf{x}, 0)) + N_2(\psi_2(\mathbf{x}, 0)). \quad (4.25)$$

The energy of the system is also conserved

$$E_\beta(\psi_1, \psi_2) = \int_{\mathbb{R}^d} \sum_{j=1}^2 \left[\frac{1}{2} |\nabla \psi_j|^2 + V_j(\mathbf{x}) |\psi_j|^2 - \Omega \bar{\psi}_j L_z \psi_j + \frac{1}{2} \sum_{l=1}^2 \beta_{jl} |\psi_l|^2 |\psi_j|^2 \right] - \lambda (\bar{\psi}_1 \psi_2 + \bar{\psi}_2 \psi_1) \, d\mathbf{x}. \quad (4.26)$$

Moreover, for the total angular momentum expectation, i.e.,

$$\langle L_z \rangle(t) := \langle L_z^1 \rangle(t) + \langle L_z^2 \rangle(t), \quad (4.27)$$

where $\langle L_z \rangle^j(t) = \int_{\mathbb{R}^d} \bar{\psi}_j(\mathbf{x}, t) L_z \psi_j(\mathbf{x}, t) \, d\mathbf{x}$ ($d=2,3$), we have the following lemma,

Lemma 4.3.1 *Suppose $\psi_j(\mathbf{x}, t)$ is the solution of the coupled GPEs (4.23) with $\beta_{12} = \beta_{21}$, then we have*

$$\frac{d\langle L_z \rangle(t)}{dt} = \sum_{j=1}^2 (\gamma_{x,j}^2 - \gamma_{y,j}^2) \int_{\mathbb{R}^d} xy |\psi_j(\mathbf{x}, t)|^2 d\mathbf{x}, \quad t \geq 0. \quad (4.28)$$

Moreover, if $\gamma_{x,j} = \gamma_{y,j}$ ($j=1,2$), we can obtain that $\frac{d\langle L_z \rangle}{dt} = 0$, i.e., the total angular momentum expectation is conserved.

Finally, for the total condensate width of two-component BEC in 2D, i. e.,

$$\delta(t) = \sum_{j=1}^2 (\delta_x^j(t) + \delta_y^j(t)), \quad (4.29)$$

where $\delta_\alpha^j(t) = \int_{\mathbb{R}^2} \alpha^2 |\psi_j(x, y, t)|^2 dx dy$ ($\alpha = x$ or y), we have the following lemma,

Lemma 4.3.2 *Suppose $\psi_j(x, y, t)$ is the solution of the coupled GPEs (4.23) in 2D with $\beta_{12} = \beta_{21}$, and $\gamma_{x,1} = \gamma_{y,1} = \gamma_{x,2} = \gamma_{y,2}$ ($:= \gamma_r$), then we have*

$$\frac{d^2 \delta(t)}{dt^2} = -4\gamma_r^2 \delta(t) + 4E_\beta(\psi_1, \psi_2) + 4\Omega \langle L_z \rangle(0), \quad t \geq 0, \quad (4.30)$$

which is a second-order ODE with constant coefficients for $\delta(t)$, i.e., $\delta(t)$ is periodic with respect to time.

The proofs of lemma (4.3.1) lemma (4.3.2) can be followed as the way done in [19].

4.3.2 A TSSP method for the coupled GPEs

In this subsection, we extend the efficient and unconditional stable TSSP method for the GPE in a rotating frame to solve the coupled GPEs (4.23). In practical computation, we always truncate the problem (4.23) into a bounded computational domain with homogeneous Dirichlet boundary conditions and given initial conditions:

$$i \frac{\partial}{\partial t} \psi_j = \left(-\frac{1}{2} \nabla^2 - \Omega L_z + V_j(\mathbf{x}) + \sum_{l=1}^2 \beta_{jl} |\psi_l|^2 \right) \psi_j - \lambda \psi_{k_j}, \quad (4.31)$$

$$\psi_j(\mathbf{x}, t) = 0, \quad \mathbf{x} \in \Gamma = \partial\Omega_{\mathbf{x}}, \quad t \geq 0, \quad (4.32)$$

$$\psi_j(\mathbf{x}, 0) = \psi_{j,0}(\mathbf{x}), \quad \mathbf{x} \in \Omega_{\mathbf{x}}, \quad (4.33)$$

where the initial data $\psi_{j,0}(\mathbf{x})$ ($j=1,2$) in the equations (4.33) are chosen such that $\sum_{j=1}^2 \|\psi_{j,0}(\mathbf{x})\|^2 = 1$.

Time-splitting

We choose a time step size $\Delta t > 0$. For $n = 0, 1, 2, \dots$, from time $t = t_n$ to $t = t_{n+1}$, first one solves

$$i \partial_t \psi_j(\mathbf{x}, t) = -\frac{1}{2} \nabla^2 \psi_j(\mathbf{x}, t) - \Omega L_z \psi_j(\mathbf{x}, t), \quad j = 1, 2 \quad (4.34)$$

for the time step of length Δt , second one solves

$$i \partial_t \psi_j(\mathbf{x}, t) = V_j(\mathbf{x}) + \beta_{j1} |\psi_1|^2 + \beta_{j2} |\psi_2|^2, \quad j = 1, 2 \quad (4.35)$$

for the same time step, and finally one solves the equations

$$i \frac{\partial}{\partial t} \Psi(\mathbf{x}, t) = C \Psi(\mathbf{x}, t) \quad (4.36)$$

for the same time step again. Here $\Psi(\mathbf{x}, t) = \begin{pmatrix} \psi_1(\mathbf{x}, t) \\ \psi_2(\mathbf{x}, t) \end{pmatrix}$ and $C = -\lambda \begin{pmatrix} 0 & 1 \\ 1 & 0 \end{pmatrix}$.

For any $t \in [t_n, t_{n+1}]$, the equations (4.34) are decoupled and each equation for $\psi_j(\mathbf{x}, t)$ ($j=1,2$) can be solved by using the Fourier Pseudospectral technique presented in section 3.2.

For the equations (4.35), since $|\psi_j(\mathbf{x}, t)|^2$ are conserved with respect to $t \in [t_n, t_{n+1}]$, they can be exactly solved as follows:

$$\psi_j(\mathbf{x}, t) = e^{-i(V_j(\mathbf{x}) + \beta_{j1} |\psi_1(\mathbf{x}, t_n)|^2 + \beta_{j2} |\psi_2(\mathbf{x}, t_n)|^2)(t - t_n)}, \quad j = 1, 2.$$

For the equations (4.36), since λ is real, the matrix C can be factorized to be PQP^{-1} where $P = \frac{1}{\sqrt{2}} \begin{pmatrix} 1 & 1 \\ 1 & -1 \end{pmatrix}$, $Q = \begin{pmatrix} -\lambda & 0 \\ 0 & \lambda \end{pmatrix}$ and $P^{-1} = \frac{1}{\sqrt{2}} \begin{pmatrix} 1.0 & 1.0 \\ 1.0 & -1.0 \end{pmatrix}$. Thus we can obtain a one-step approximations of the equations (4.36) as

$$\Psi^{n+1} = P \exp(-i\Delta t Q) P^{-1} \Psi^n,$$

where $\Psi^n = \Psi(t_n)$.

Discretization in 2D

When $d=2$ in (4.31), we choose the same mesh (x_j, y_k) as those defined in (3.17). Let $\psi_{r,jk}^n$ be the approximation of $\psi_r(x_j, y_k, t_n)$ and ψ_r^n be the solution vector with component $\psi_{r,jk}^n$ ($r=1$, or 2). From time t_n to time t_{n+1} , we apply the second-order time-splitting [36] and obtain the following algorithm of the TSSP method for the coupled GPEs (4.31):

$$\begin{aligned}
\psi_{r,jk}^{(1)} &= \sum_{p=-M/2}^{M/2-1} e^{-i\Delta t(\mu_p^2+2\Omega y_k \mu_p)/4} \widehat{(\psi_{r,k}^n)}_p e^{i\mu_p(x_j-a)}, \quad 0 \leq j \leq M, \quad 0 \leq k \leq N, \\
\psi_{r,jk}^{(2)} &= \sum_{q=-N/2}^{N/2-1} e^{-i\Delta t(\lambda_q^2-2\Omega x_j \lambda_q)/4} \widehat{(\psi_{r,j}^{(1)})}_q e^{i\lambda_q(y_k-c)}, \quad r = 1, 2, \\
\psi_{1,jk}^{(3)} &= \cos(i\lambda\Delta t/2)\psi_{1,jk}^{(2)} + \sin(i\lambda\Delta t/2)\psi_{2,jk}^{(2)}, \\
\psi_{2,jk}^{(3)} &= \sin(i\lambda\Delta t/2)\psi_{1,jk}^{(2)} + \cos(i\lambda\Delta t/2)\psi_{2,jk}^{(2)}, \\
\psi_{r,jk}^{(4)} &= e^{-i\Delta t(V_r(x_j,y_k)+\beta_{r1}|\psi_{1,jk}^{(3)}|^2+\beta_{r2}|\psi_{2,jk}^{(3)}|^2)} \psi_{r,jk}^{(3)}, \\
\psi_{1,jk}^{(5)} &= \cos(i\lambda\Delta t/2)\psi_{1,jk}^{(4)} + \sin(i\lambda\Delta t/2)\psi_{2,jk}^{(4)}, \\
\psi_{2,jk}^{(5)} &= \sin(i\lambda\Delta t/2)\psi_{1,jk}^{(4)} + \cos(i\lambda\Delta t/2)\psi_{2,jk}^{(4)}, \\
\psi_{r,jk}^{(6)} &= \sum_{q=-N/2}^{N/2-1} e^{-i\Delta t(\lambda_q^2-2\Omega x_j \lambda_q)/4} \widehat{(\psi_{r,j}^{(5)})}_q e^{i\lambda_q(y_k-c)}, \\
\psi_{r,jk}^{n+1} &= \sum_{p=-M/2}^{M/2-1} e^{-i\Delta t(\mu_p^2+2\Omega y_k \mu_p)/4} \widehat{(\psi_{r,k}^{(6)})}_p e^{i\mu_p(x_j-a)}, \tag{4.37}
\end{aligned}$$

where for each fixed k , $\widehat{(\psi_{r,k}^*)}_p$ ($p = -M/2, \dots, M/2 - 1$) and for each fixed j , $\widehat{(\psi_{r,j}^*)}_q$ ($q = -N/2, \dots, N/2 - 1$) are the Fourier coefficients of the vector $\psi_{r,k}^* = (\psi_{r,0k}^*, \psi_{r,1k}^*, \dots, \psi_{r,(M-1)k}^*)^T$ and the vector $\psi_{r,j}^* = (\psi_{r,j0}^*, \psi_{r,j1}^*, \dots, \psi_{r,j(N-1)}^*)^T$ respectively.

Remark 4.3.1 *The above-shown TSSP method (4.37) is presented for the coupled GPEs (4.31) in 2D. The method can be extended to the coupled GPEs (4.31) in 3D as what have been presented in Chapter 3.*

Remark 4.3.2 *In some cases the trapping potential V_j in the equations (4.35) depends on time t , we can solve them in the way that*

$$\psi_j(\mathbf{x}, t) = e^{-i(V_j^n(\mathbf{x}) + \beta_{j1}|\psi_1(\mathbf{x}, t_n)|^2 + \beta_{j2}|\psi_2(\mathbf{x}, t_n)|^2)(t - t_n)}, \quad j = 1, 2,$$

where $V_j^n(\mathbf{x}) = \int_{t_n}^t V_j(\mathbf{x}, \tau) d\tau$ and $t \in [t_n, t_{n+1}]$.

Stability

For the **stability** of the time-splitting spectral approximations (4.37) for the coupled GPEs (4.31) in 2D, we have the following lemma, which shows that the total density $\sum_{r=1}^2 \|\psi_r(\mathbf{x}, t)\|^2$ is conserved in the discretized level.

Lemma 4.3.3 *The time-splitting spectral approximations (4.37) for the coupled GPEs (4.31) in 2D are unconditionally stable. In fact, for every mesh sizes, and time step size,*

$$\sum_{r=1}^2 \|\psi_r^n\|_{l^2}^2 \equiv \sum_{r=1}^2 \|\psi_r^0\|_{l^2}^2, \quad r = 1, 2, \quad n = 1, 2, \dots \quad (4.38)$$

Proof: Follows the line of the analogous results for the linear and nonlinear Schrödinger equations in [10, 11].

4.3.3 Numerical results for the dynamics

In this subsection we apply the proposed TSSP method to solve the coupled GPEs (4.31). We first compare our numerical results with analytical results reviewed in the subsection 4.3.1. We next generate similar topological modes such as one vortex, double vortices, dipole and quadrupole for two-component BEC as which have been found in [134, 135]. We finally study vortex lattice dynamics in the rotating two-component BEC.

Example 4.6 To test the accuracy of the newly proposed TSSP method for the coupled GPEs (4.31), we solve these equations with $\Omega = 0.6$, $\beta_{11} = \beta_{22} = 100$, $\beta_{12} = \beta_{21} = 70$, $V_j(x, y) = \frac{1}{2}(\gamma_x^2 x^2 + \gamma_y^2 y^2)$ ($j = 1, 2$), and $\lambda = 2.0$. The initial data are taken as $\psi_1(x, y, 0) = \frac{1}{\sqrt{2\pi}} e^{-(x^2+y^2)/2}$, and $\psi_2(x, y, 0) = \frac{1.5^{\frac{1}{4}}}{\sqrt{2\pi}} e^{-(x^2+1.5y^2)/2}$.

From our analytical results in the subsection 4.3.1, we know that, when $\lambda \neq 0$, the total norm of two components and the total angular momentum expectation and are conserved, which are confirmed by the numerical results shown in Figure 4.10 (a) and (c). Furthermore the total condensate width are periodic when $\gamma_x = \gamma_y$ and not periodic otherwise, which are confirmed by the results shown in Figure 4.10 (b) and (d). Although time evolution of the energy is not well conserved in the discretized level, it oscillates not more than 5 percent of its true value, which is not plotted in Figure 4.10.

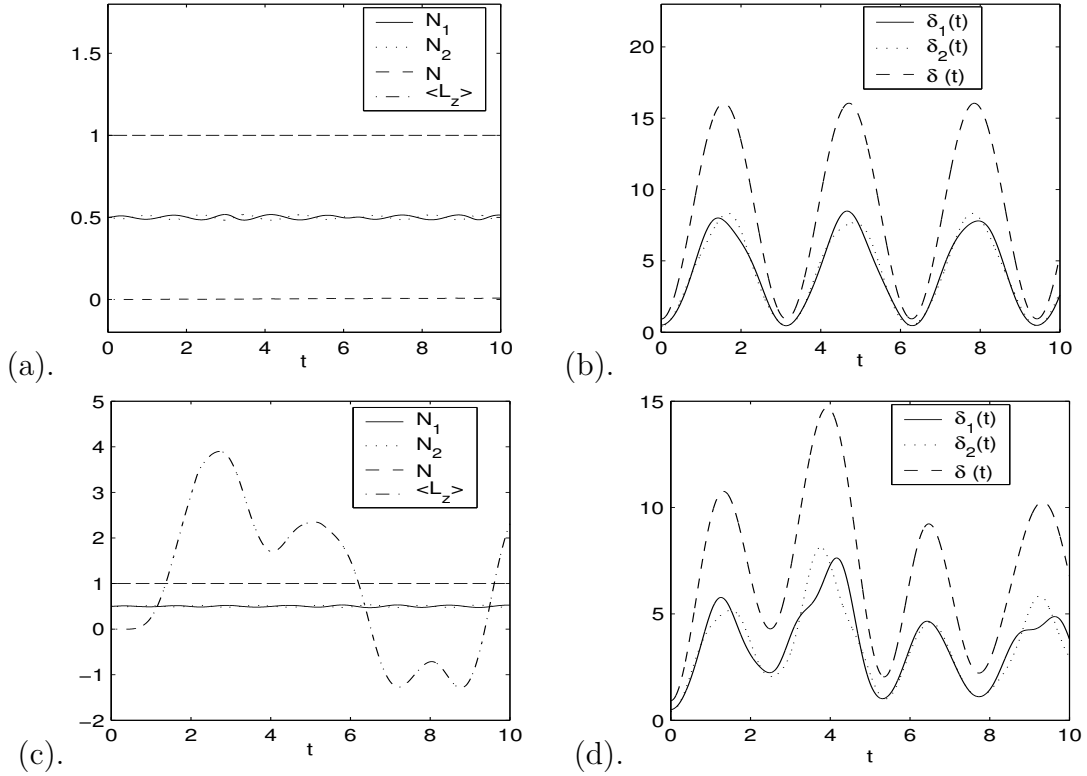


Figure 4.10: Time evolutions of the normalization $N_1 := N_1(\psi_1)$, $N_2 := N_2(\psi_2)$, $N := N_1 + N_2$ and the total angular momentum expectation $L_z := \langle L_z \rangle(t)$ with $\lambda = 2.0$. (a&b) are results for $\gamma_x = \gamma_y = 1.0$; (c&d) are results for $\gamma_x = 1.0$ and $\gamma_y = 1.5$.

Example 4.7 To generate the topological modes in the two-component BEC, we solve the coupled GPEs (4.31) with $\Omega = 0$, $\beta_{11} = 1671.587$, $\beta_{12} = \beta_{21} = 1622.9$, $\beta_{22} =$

1574.213 and $\lambda = -2.5$. The time-dependent potentials take the form [135, 134]: $V_1(x, y, t) = \frac{1}{2}(x^2 + y^2) + \tilde{\delta}/2 + \tilde{\kappa}(\tilde{f}(x, y) \cos(\tilde{\omega}t) + \tilde{g}(x, y) \sin(\tilde{\omega}t))$, $V_2(x, y, t) = \frac{1}{2}(x^2 + y^2) - \tilde{\delta}/2 - \tilde{\kappa}(\tilde{f}(x, y) \cos(\tilde{\omega}t) + \tilde{g}(x, y) \sin(\tilde{\omega}t))$ where $\tilde{\delta} = 20.0$, $\tilde{\omega} = 20.54$ and $\tilde{\kappa} = 0.499$. For $\tilde{f}(x, y)$ and $\tilde{g}(x, y)$, we have four cases: case A, $\tilde{f}(x, y) = x$ and $\tilde{g}(x, y) = y$; case B, $\tilde{f}(x, y) = x^2 - y^2$ and $\tilde{g}(x, y) = 2xy$; case C, $\tilde{f}(x, y) = x$ and $\tilde{g}(x, y) = 0$; and case D: $\tilde{f}(x, y) = xy$ and $\tilde{g}(x, y) = 0$.

We prepare the initial data with $\psi_2(x, y, 0) = 0$ and $\psi_1(x, y, 0)$ being the ground state $\phi^g(x, y)$ of the non-rotating one-component BEC in the symmetric trap $\frac{1}{2}(x^2 + y^2)$ with $\beta_2 = 1622.9$ (see section 2.3).

Figures 4.11, 4.12, 4.13 and 4.14 show the time evolution of the density of the second component. We find that we can dynamically generate one vortex for case A (c.f. Figure 4.11), double vortices for case B (c.f. figure 4.12), a dipole for case C (c.f. figure 4.13) and quadrupole for case D (c.f. figure 4.14) in the second component. These numerical results agree very well with those obtained in [135], where the author applied the time-splitting finite difference method to solve the coupled GPEs (4.31) with the above-mentioned parameters.

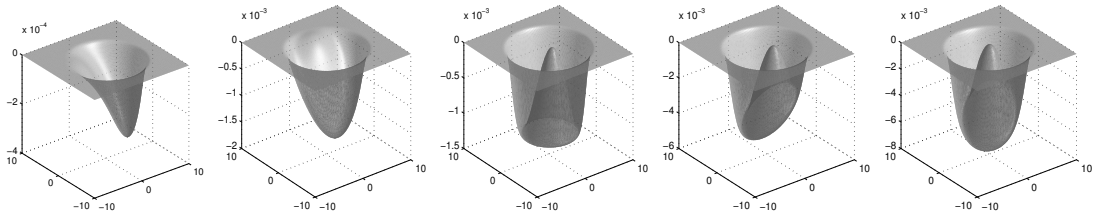


Figure 4.11: Surface plots of the density $|\psi_2(x, y, t)|^2$ at $t=0.25, 0.75, 1.5, 2.75$ and 3.75 respectively for case A.

Example 4.8 To study the vortex lattice dynamics of the rotating two-component BEC when only the second component prepared with the vortex lattice initially, we solve the coupled GPEs (4.31) with $\Omega = 0.85$, $\beta_{11} = 2060$, $\beta_{12} = \beta_{21} = 2000$, $\beta_{22} = 1940$, $V_j(x, y) = \frac{1}{2}(x^2 + y^2)$ ($j = 1, 2$) and $\lambda = -1.0$. We prepare the initial conditions with $\psi_2(x, y, 0) = 0$ and $\psi_1(x, y, 0)$ being the ground state $\phi^g(x, y)$ of rotating one-component BEC in a symmetric trap $\frac{1}{2}(x^2 + y^2)$ with $\beta_2 = 1000$ and

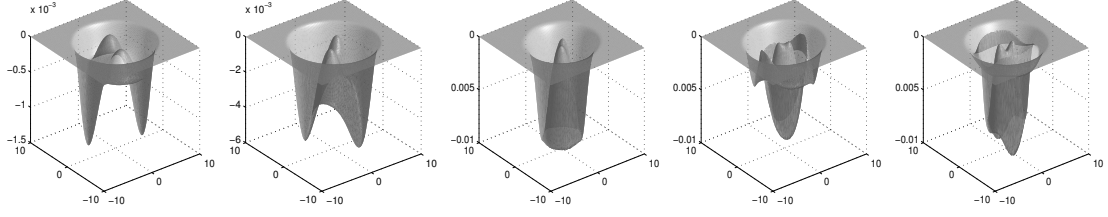


Figure 4.12: Surface plots of the density $|\psi_2(x, y, t)|^2$ at $t=0.25, 0.75, 2.0, 3.0$ and 4.0 respectively for case B.

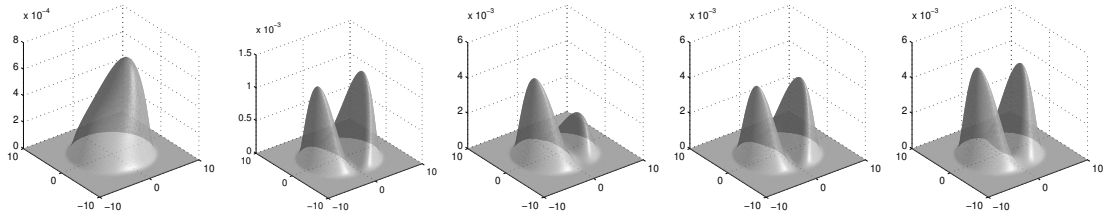


Figure 4.13: Surface plots of the density $|\psi_2(x, y, t)|^2$ at $t=0.5, 1.5, 2.5, 3.0$ and 3.5 respectively for case C.

$\Omega = 0.85$ (see section 2.3).

Figure 4.15 and Figure 4.16 (a)&(b) show that the population of component one, i.e., $|\psi_1(x, y, t)|^2$, transferred to that of component two periodically (c.f. Figure 4.16 (a)). When the coupling term $|\lambda|$ increases larger, the transferring period becomes shorter (c.f. Figure 4.16 (b)).

Example 4.9 To study the dynamics of the rotating two-component BEC when both components are prepared with the vortex lattice initially, we solve the coupled GPEs (4.31) with $\Omega = 0.6$, $\beta_{11} = \beta_{22} = \beta_2$, $\beta_{12} = \beta_{21} = \beta_2 \times 0.7$, $\beta_2 = 2000$,

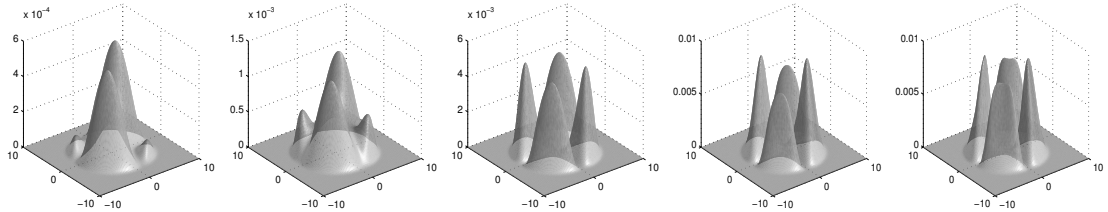


Figure 4.14: Surface plots of the density $|\psi_2(x, y, t)|^2$ at $t=0.25, 0.5, 1.5, 2.5$ and 3.5 respectively for case D.

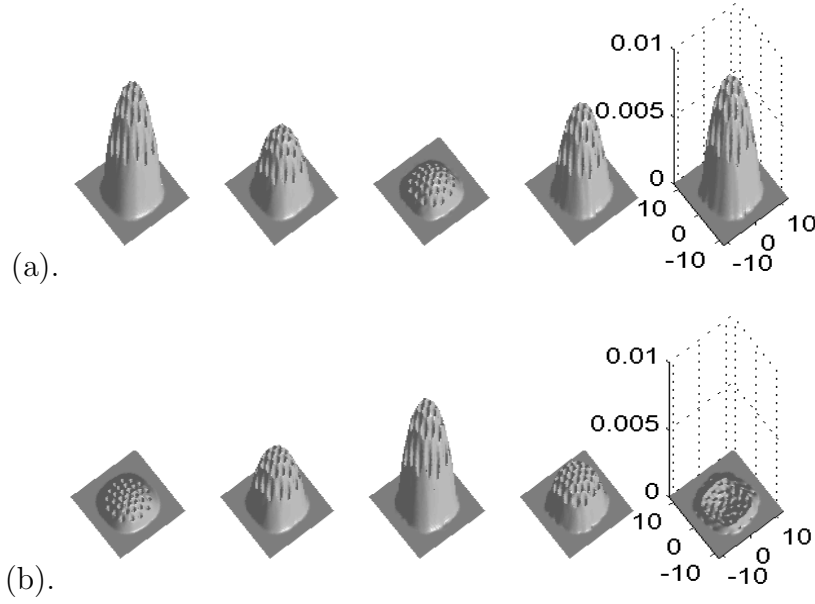


Figure 4.15: Surface plots of the density $|\psi_1(x, y, t)|^2$ (upper row) and $|\psi_2(x, y, t)|^2$ (low row) at $t=0.25, 0.75, 1.25, 2.5$ and 3.0 respectively for vortex lattice dynamics.

$\lambda = 0$ and the trap potentials $V_j(x, y) = \frac{1}{2}(\gamma_x^2 x^2 + \gamma_y^2 y^2)$ ($\gamma_x^2 = \gamma_y^2 = 1.0$). These parameters follows the typical experimental setups [75].

The initial conditions used for the simulations are ground state $\phi_j^g(x, y)$ ($j=1,2$) of the rotating two-component BEC with $\beta_{11} = \beta_{22} = 2000$ $\beta_{12} = \beta_{21} = 1400$ and $\Omega = 0.6$, (see subsection 4.2.3). Both of the condensates have vortex lattice initially.

First we study how the changes in the trap potentials' frequencies affect the evolution of vortices. In Figure 4.17, we consider the traps are suddenly removed at $t = 0$, i.e., the free expansion of vortices in the rotating two-component condensates. We can see that the vortex patterns of both components are not destroyed, instead the vortex expanded with respect to time. In Figure 4.18(a), we suddenly increase the value of γ_y^2 by a factor of 1.5 from 1.0 to 1.5 at $t = 0$. With this sudden increases, the condensates start to shrink in the y-direction and move clockwise and finally reach to steady state. In Figure 4.18(b), we suddenly increase the value of γ_x^2 by a factor of 1.5 from 1.0 to 1.5 at $t = 0$. With these sudden increases, the condensates start to shrink in the x-direction and move clockwise and finally reach to a steady

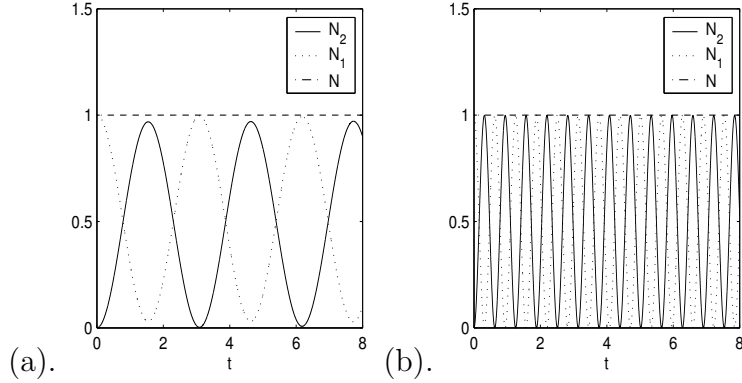


Figure 4.16: Time evolutions of norms $N_1 := N_1(\psi_1)$, $N_2 := N_2(\psi_2)$ and $N = N_1 + N_2$ change with respect to time t . (a) $\lambda = -1.0$; (b) $\lambda = -5.0$.

state. Moreover, we find that the condensates start to shrink in the x -axis (or y -axis) direction and move anticlockwise if we decrease the value of γ_y^2 (or γ_x^2).

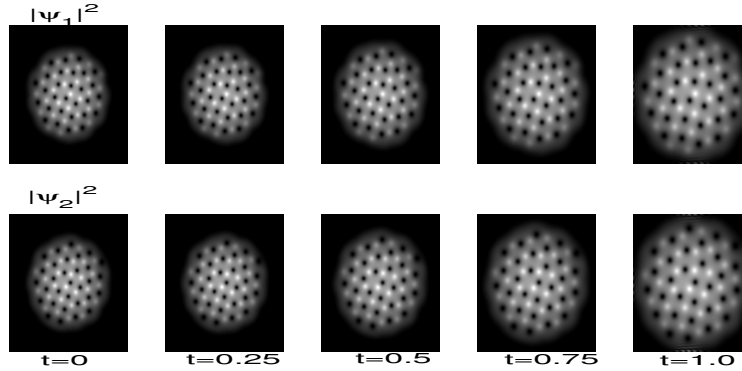


Figure 4.17: Results of free expansion of quantized vortex lattice at different times. Size of each square is $[-12, 12] \times [-12, 12]$.

Second we study how the changes in the trapping potentials' centers affect the evolution of vortices. In simulation presented in Figure 4.19(a), we let the trapping potentials $V_1(x, y) = \frac{1}{2}(x^2 + (y - 0.5)^2)$ and $V_2(x, y) = \frac{1}{2}(x^2 + (y + 0.5)^2)$ at $t=0$. In the simulation presented in Figure 4.19(b), we let the trapping potentials $V_1(x, y) = \frac{1}{2}((x - 0.5)^2 + y^2)$ and $V_2(x, y) = \frac{1}{2}((x + 0.5)^2 + y^2)$ at $t=0$. We observe that the more time goes on, the less vortices from component 1 overlap those from component 2 in the y -axis or x -axis direction (c.f. Figure 4.19(a) & (b)).

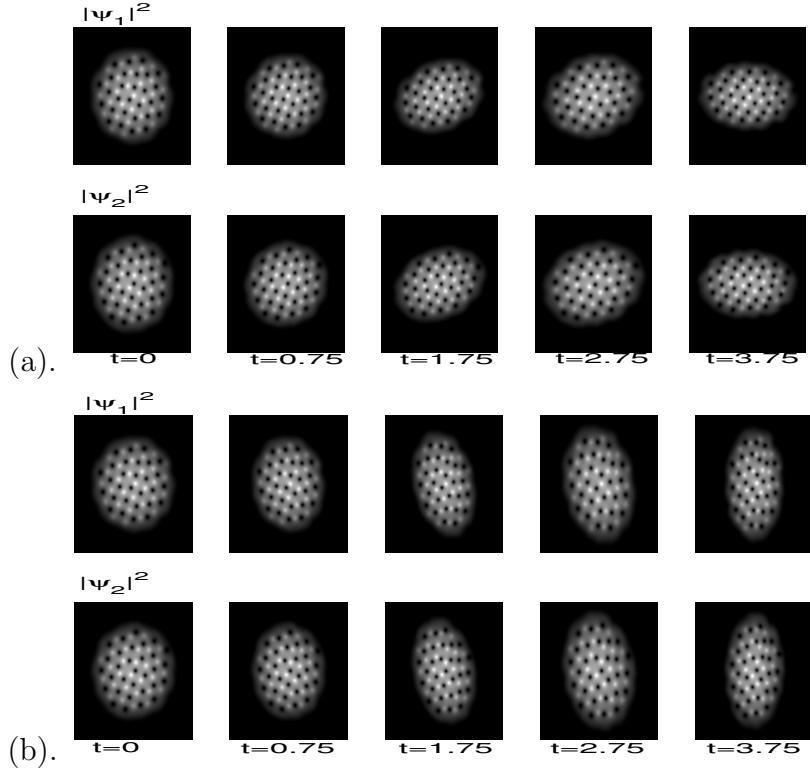


Figure 4.18: Image plots of the density $\psi_j(\mathbf{x}, t)$ on $[-12, 12] \times [-12, 12]$ at different times upon sudden increase of the trapping frequency (a) γ_y^2 , or (b) γ_x^2 from 1 to 1.5 at $t=0$.

Third we study how the changes in interactions between the two-component condensates affect the evolution of vortices. In simulation presented in Figure 4.20(a), we suddenly increase the parameter β_2 from 2000 to 5000 at $t = 0$. Evolution of the resultant condensates show that the overall size of both condensates increases. However each vortex core in the condensates shrinks. In Figure 4.20(b), we suddenly decrease the parameter β_2 from 2000 to 500 at $t = 0$. We can see that the whole pattern of vortices become smaller but each vortex core in the condensates expands.

Finally we study the effect of the inclusion of the internal Josephson coupling term λ on the dynamics of vortices. From Figure 4.21, we find that the inclusion of λ immediately destroy the pattern of equilibrated vortices and finally the vortex in each component loses its independent identity. With the increasing value of $|\lambda|$, the

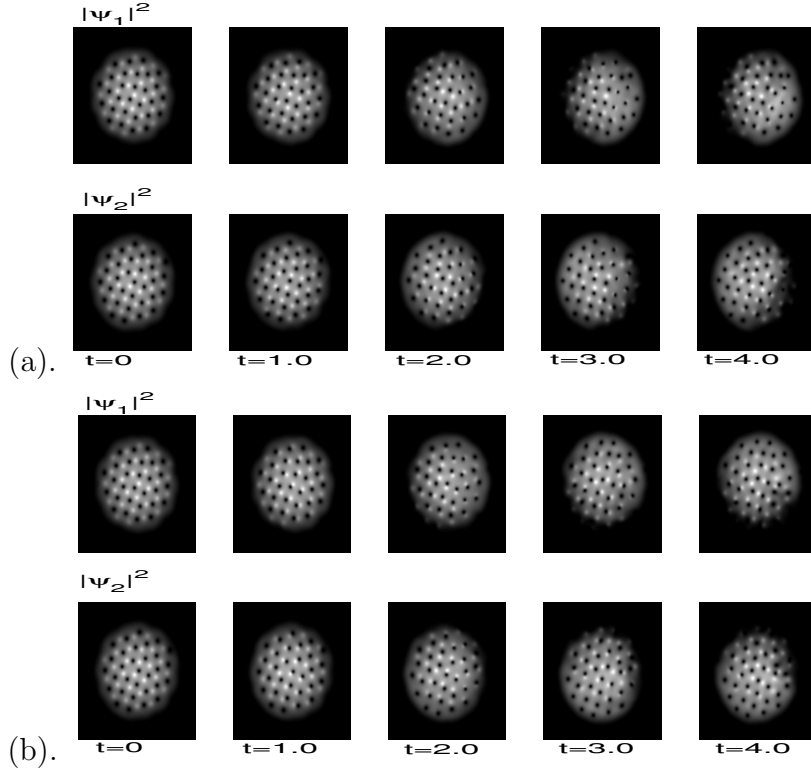


Figure 4.19: Image plots of the density $\psi_j(\mathbf{x}, t)$ on $[-12, 12] \times [-12, 12]$ at different times with traps having a shifted center 0.5 (a) in y direction; or (b) in x direction only.

observed phenomena continues and chaotic behavior become more evident.

4.4 Conclusion

We have conducted extensive numerical study to find the ground state for the rotating two-component BEC in 2D. We also searched the excited states such as symmetric states and central vortex states. From our numerical studies on the ground state, when the two components have equal number of particle numbers, we have the following observations: (1) Each component has a vortex lattice and lattices are interlaced, vortex cores in either component are filled by fluid of the other component; (2) When the two components have different intra-component interactions

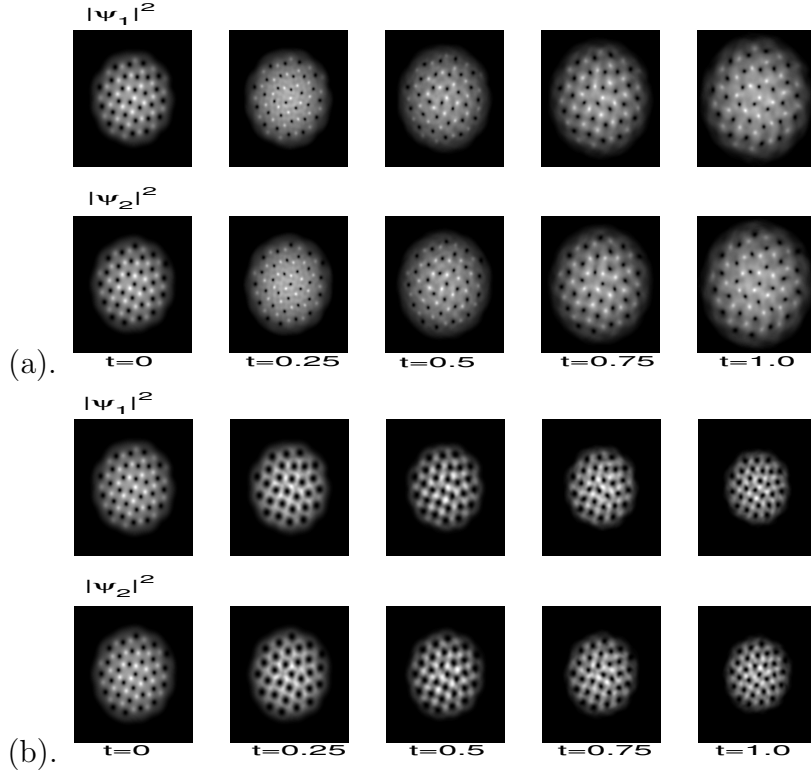


Figure 4.20: Image plots of the density $\psi_j(\mathbf{x}, t)$ on $[-12, 12] \times [-12, 12]$ at different times upon (a) sudden increase of β_2 from 2000 to 5000 at $t=0$; or (b) sudden decrease of β_2 from 2000 to 500 at $t=0$.

(i.e., $\beta_{11} \neq \beta_{22}$, even in the case that the difference is a few percent), component 1 does not have the same number of vortices as component 2 with the frequency Ω increasing, although the two components have a coexistence system of different vortex-core size; (3) with the increasing of particle numbers N of both components ($N = N_1 = N_2$), the vortex number in each component will increase gradually. When the two components have different particle numbers (i.e. $N_1 \neq N_2$), for example $N_1 > N_2$, we may see that component 1 has vortices at which component 2 has its peaks. After comparing the energy of symmetric state with those of the ground state, we find that the critical frequency at which the ground state lose symmetry becomes less when the particle number becomes larger. We also find that the peak of central vortex state for each component decreases when the particle number

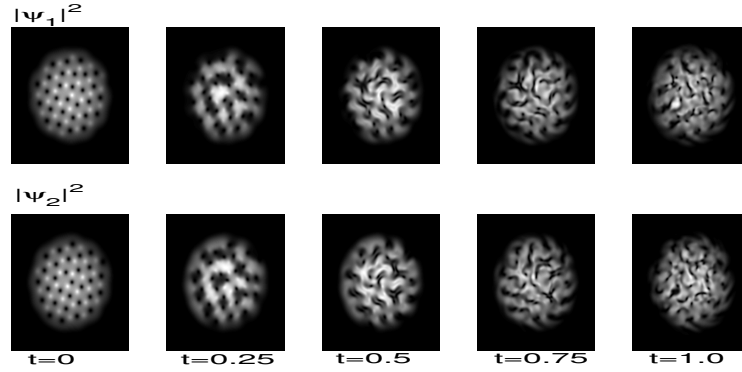


Figure 4.21: Image plots of the density $\psi_j(\mathbf{x}, t)$ on $[-12, 12] \times [-12, 12]$ at different times with inclusion of the coupling term $\lambda = 2.0$ at $t=0$.

of each component increases.

We also have proposed a new TSSP method for the coupled GPEs with a coupling term and applied it into studying the generation of topological modes and the vortex lattice dynamics of the rotating two-component BEC. We find that our numerical results agree with the analytical results from the coupled GPEs. Our numerical results on the generation of topological modes agree well with those presented in [134]. If we prepare one component with a vortex lattice initially, the Josephson coupling term λ can determine the transferring speed of population from one component to another. If we prepare both components with vortex lattice initially, we find that the dynamical behaviors of the equilibrated vortices in the rotating two-component BEC are rich: By increasing or decreasing the trap frequencies in the y-axis or x-axis direction, the vortex pattern move clockwise or anticlockwise but continues to overlapping each other. By switching off the traps, the vortices expand until reaching the computed area. By shifting the trap centers in the y-axis or x-axis direction, the vortices of each component will overlap each other less with time going on in in the y-axis or x-axis direction. By increasing or decreasing interactions between atoms, the vortices expand or shrink. By including the Josephson coupling term into the condensates, we find the vortex dynamics becomes chaotic.

Applications to dynamics of spinor $F=1$ BEC

One of the recent developments in Bose-Einstein condensation is the study of dilute Bose gases with spin degrees of freedom [92]. The first achievement of spinor Bose-Einstein condensation in experiments was recently done by an optical method in ^{23}Na [125] and ^{87}Rb [114]. These systems can keep internal degrees of freedom with hyperfine spin $F=1$.

The general theoretical framework for describing a spinor $F=1$ BEC was given by Ohmi and Machida [101], and independently by Ho [64]. This framework is based on mean field theory with the Bogoliubov approximation extended to a vectorial order parameter with three components, corresponding to $m_F = 1, 0, -1$ of the $F=1$ atomic hyperfine state. As a result, for a spinor $F=1$ condensate, the three spin components $m_F = 1, 0, -1$ are described by a vector order parameter, $\Psi(\mathbf{x}, t) = (\psi_1(\mathbf{x}, t), \psi_0(\mathbf{x}, t), \psi_{-1}(\mathbf{x}, t))^T$, which is governed by a generalized GPEs [64, 101]. Based on the generalized GPEs, much of previous theoretical work were concerned with spin textures, spin mixing, spinor domain formation, topological excitations, central vortex states and ground state properties of spinor $F=1$ without rotation by finding the stationary solutions of the generalized GPEs [24, 64, 68, 69, 95, 101, 113, 125, 137].

For rotating spinor $F=1$ condensates, either within or not within a magnetic field, the vector order parameter, $\Psi(\mathbf{x}, t)$ is governed by a generalized GPEs with an angular momentum [77]. For the stationary states such as symmetric and central vortex states of rotating spinor $F=1$ BEC, Mizushima et al. have performed a systematically numerical study on their structure and stability in the zero magnetic field (see [94] and reference inside). The ground state of rotating spinor $F=1$ condensates have been investigated theoretically by assuming that the bosons are in the quantum states in the lowest Landau level [109]. The ground state of rotating spinor $F=1$ condensates have also been studied through direct numerical simulation by Mizushima et al. [79, 90, 94].

Few studies are investigated on the dynamics of the spinor $F=1$ BEC with or without rotation [107, 115], which, however, becomes one of the focuses of research in the spinor BEC physics recently [16, 31, 77, 99, 106, 114]. The dynamics of such spinor $F=1$ condensates at extremely low temperature is governed by the time-dependent generalized GPEs. These generalized GPEs are coupled nonlinear Schrödinger equations, which are difficult to solve in higher dimensions [99, 105, 109]. In this chapter, we will design a TSSP method for the generalized GPEs. This TSSP method has a lot of advantages: the method is time-reversible, time-invariant and of spectral accuracy in space; it is unconditionally stable as what was described in Chapter 3. Moreover, with this efficient and accurate method, we could obtain the dynamics of the spinor $F=1$ BEC by numerically integrating the generalized GPEs, without any further approximation such as the Single Mode Approximation [106] or variational ansatz [138].

This chapter is organized as follows. In section 5.1, we introduce the generalized GPEs for the spinor BEC and its dimensionless formulation in 3D; then we reduce them to equations in 2D and one dimension (1D). In section 5.2, we present some analytical properties of the generalized GPEs. In section 5.3, we describe the TSSP method for the generalized GPEs in detail. In section 5.4, we test the accuracy of the method and compare numerical results with analytical results presented in

section 5.2 and previous numerical studies. We then apply the method to study the generation of vortices for the spinor $F=1$ BEC held in a magnetic field and the effect of the magnetic field on vortex lattice dynamics. Some conclusions are made in section 5.5.

5.1 The generalized Gross-Pitaevskii equations

The mathematical model for spinor $F = 1$ BEC in the absence of magnetic field is the following generalized Gross Pitavsekii equations [30, 77, 94, 115]

$$\begin{aligned} i\hbar \frac{\partial}{\partial t} \psi_1 &= \left(-\frac{\hbar^2 \nabla^2}{2m} + V - \Omega L_z + g_n \rho \right) \psi_1 + g_s (\rho_1 + \rho_0 - \rho_{-1}) \psi_1 + g_s \bar{\psi}_{-1} \psi_0^2, \\ i\hbar \frac{\partial}{\partial t} \psi_0 &= \left(-\frac{\hbar^2 \nabla^2}{2m} + V - \Omega L_z + g_n \rho \right) \psi_0 + g_s (\rho_1 + \rho_{-1}) \psi_0 + 2g_s \psi_1 \psi_{-1} \bar{\psi}_0, \\ i\hbar \frac{\partial}{\partial t} \psi_{-1} &= \left(-\frac{\hbar^2 \nabla^2}{2m} + V - \Omega L_z + g_n \rho \right) \psi_{-1} + g_s (\rho_0 + \rho_{-1} - \rho_1) \psi_{-1} + g_s \bar{\psi}_1 \psi_0^2, \end{aligned} \quad (5.1)$$

where $\psi_j = \psi_j(\mathbf{x}, t)$ ($j = 1, 0, -1$) are wave functions of three components for the spinor BEC, $\rho_j = |\psi_j|^2$ and $\rho = \sum_{j=-1}^1 \rho_j$. The trap potential $V = V(\mathbf{x}) = \frac{1}{2}m(\omega_x^2 x^2 + \omega_y^2 y^2 + \omega_z^2 z^2)$. The interaction between atoms with the mass m is characterized by the interaction strengths through the ‘‘density’’ channel, $g_n = \frac{4\pi\hbar^2}{m} \cdot \frac{a_0 + 2a_2}{3}$, and the ‘‘spin’’ channel, $g_s = \frac{4\pi\hbar^2}{m} \cdot \frac{a_2 - a_0}{3}$, where a_0 and a_2 are the s -wave scattering length with the total spin 0 and 2 channels, respectively. When $\Omega \neq 0$, the spinor $F=1$ BEC is in a rotating trap.

For the wave functions ψ_j , the total particle number $N = \sum_{j=-1}^1 N_j$, $N_j = \int_{\mathbb{R}^3} \rho_j(\mathbf{x}) d\mathbf{x}$, the total magnetization $M = \sum_{j=-1}^1 \int_{\mathbb{R}^3} j |\psi_j(\mathbf{x}, t)|^2 d\mathbf{x}$, and the energy of the system

$$\begin{aligned} E(\psi_1, \psi_0, \psi_{-1}) &= \int_{\mathbb{R}^3} \left[\sum_{j=-1}^1 \left(\frac{\hbar^2}{2m} |\nabla \psi_j|^2 + V |\psi_j|^2 - \Omega \bar{\psi}_j L_z \psi_j \right) + \frac{g_n}{2} \rho^2 + \right. \\ &\quad \left. \frac{g_s}{2} (\rho_1^2 + \rho_{-1}^2 + 2\rho_1 \rho_0 + 2\rho_0 \rho_{-1} - 2\rho_1 \rho_{-1}) \right. \\ &\quad \left. + g_s (\bar{\psi}_{-1} \psi_0^2 \bar{\psi}_1 + \psi_{-1} \bar{\psi}_0^2 \psi_1) \right] d\mathbf{x}, \end{aligned} \quad (5.2)$$

are conserved.

5.1.1 Dimensionless formulation

By introducing the parameters

$$\tilde{t} = \omega_m t, \quad \tilde{\mathbf{x}} = \frac{\mathbf{x}}{b_0}, \quad \tilde{\Psi}_j(\tilde{\mathbf{x}}, \tilde{t}) = \frac{b_0^{3/2}}{\sqrt{N}} \Psi_j(\mathbf{x}, t), \quad \tilde{\Omega} = \frac{\Omega}{\omega_m}, \quad b_0 = \sqrt{\frac{\hbar}{m\omega_m}}. \quad (5.3)$$

Here we choose $1/\omega_m$ and b_0 as the dimensionless time and length units, respectively.

Plugging (5.3) into equations (5.1), multiplying by $\frac{1}{m\omega_m^2(Nb_0)^{\frac{1}{2}}}$ to the j th ($j = 1, 0, -1$) equation, and then removing all $\tilde{}$, we obtain the following dimensionless GPEs in

3D

$$\begin{aligned} i\frac{\partial}{\partial t}\psi_1 &= \left(-\frac{1}{2}\Delta + V - \Omega L_z + \lambda_n\rho\right)\psi_1 + \lambda_s(\rho_1 + \rho_0 - \rho_{-1})\psi_1 + \lambda_s\bar{\psi}_{-1}\psi_0^2, \\ i\frac{\partial}{\partial t}\psi_0 &= \left(-\frac{1}{2}\Delta + V - \Omega L_z + \lambda_n\rho\right)\psi_0 + \lambda_s(\rho_1 + \rho_{-1})\psi_0 + 2\lambda_s\psi_1\psi_{-1}\bar{\psi}_0, \\ i\frac{\partial}{\partial t}\psi_{-1} &= \left(-\frac{1}{2}\Delta + V - \Omega L_z + \lambda_n\rho\right)\psi_{-1} + \lambda_s(\rho_0 + \rho_{-1} - \rho_1)\psi_{-1} + \lambda_s\bar{\psi}_1\psi_0^2, \end{aligned} \quad (5.4)$$

where $V = V(\mathbf{x}) = \frac{1}{2}(\gamma_x^2 x^2 + \gamma_y^2 y^2 + \gamma_z^2 z^2)$, $\gamma_\alpha = \frac{\omega_\alpha}{\omega_m}$ with $\alpha = x, y, z$, $\lambda_n = \frac{4\pi N(a_0 + 2a_2)}{3b_0}$ and $\lambda_s = \frac{4\pi N(a_2 - a_0)}{3b_0}$.

5.1.2 Reduction to lower dimensions

Similar as what have been described in one-component and two-component BEC, when $\gamma_x = 1$, $\gamma_y \approx 1$ and $\gamma_z \gg \gamma_x$ ($\Leftrightarrow \omega_y \approx \omega_x$, and $\omega_z \gg \omega_x$ when choosing $\omega_m = \omega_x$), the three-dimensional generalized GPEs (5.4) can approximately be reduced to two-dimensional generalized GPEs. In addition, when $\Omega = 0$, $\gamma_x = 1$, $\gamma_y \gg \gamma_x$ and $\gamma_z \gg \gamma_x$ ($\Leftrightarrow \omega_y \gg \omega_x$, and $\omega_z \gg \omega_x$ when choosing $\omega_m = \omega_x$), the three-dimensional generalized GPEs (5.4) can also approximately be reduced to one-dimensional generalized GPEs.

Thus, here we consider the generalized GPEs in d -dimensions ($d=1,2,3$):

$$\begin{aligned} i\frac{\partial}{\partial t}\psi_1 &= \left(-\frac{1}{2}\Delta + V_d(\mathbf{x}) - \Omega L_z + \lambda_n\rho\right)\psi_1 + \lambda_s(\rho_1 + \rho_0 - \rho_{-1})\psi_1 + \lambda_s\bar{\psi}_{-1}\psi_0^2, \\ i\frac{\partial}{\partial t}\psi_0 &= \left(-\frac{1}{2}\Delta + V_d(\mathbf{x}) - \Omega L_z + \lambda_n\rho\right)\psi_0 + \lambda_s(\rho_1 + \rho_{-1})\psi_0 + 2\lambda_s\psi_1\psi_{-1}\bar{\psi}_0, \\ i\frac{\partial}{\partial t}\psi_{-1} &= \left(-\frac{1}{2}\Delta + V_d(\mathbf{x}) - \Omega L_z + \lambda_n\rho\right)\psi_{-1} + \lambda_s(\rho_0 + \rho_{-1} - \rho_1)\psi_{-1} + \lambda_s\bar{\psi}_1\psi_0^2, \end{aligned} \quad (5.5)$$

where $\Omega = 0$ when $d = 1$. λ_n and λ_s are two constants. $\rho_j = \rho_j(\mathbf{x}, t) = |\psi_j(\mathbf{x}, t)|^2$ and $\rho = \sum_{j=-1}^1 \rho_j$. The trap potential

$$V_d(\mathbf{x}) = \begin{cases} \frac{1}{2}\gamma_x^2 x^2, & d = 1, \\ (\gamma_x^2 x^2 + \gamma_y^2 y^2) / 2, & d = 2, \\ (\gamma_x^2 x^2 + \gamma_y^2 y^2 + \gamma_z^2 z^2) / 2, & d = 3, \end{cases}$$

with $\gamma_x \geq 0$, $\gamma_y \geq 0$ and $\gamma_z \geq 0$.

5.2 Some properties of the generalized GPEs

In this section, we present some analytical properties of the generalized GPEs (5.5), which will be used to test our new numerical method proposed in the next section.

The two important invariants of the generalized GPEs (5.5) are the total normalization

$$\sum_{j=-1}^1 N_j(\psi_j(\mathbf{x}, t)) = \sum_{j=-1}^1 N_j(\psi_j(\mathbf{x}, 0)) = 1, \quad N_j(\psi_j(\mathbf{x}, t)) := \int_{\mathbb{R}^d} |\psi_j(\mathbf{x}, t)|^2 d\mathbf{x}, \quad (5.6)$$

and the magnetization per particle

$$\sum_{j=-1}^1 \int_{\mathbb{R}^d} j |\psi_j(\mathbf{x}, t)|^2 d\mathbf{x} = \sum_{j=-1}^1 \int_{\mathbb{R}^d} j |\psi_j(\mathbf{x}, 0)|^2 d\mathbf{x}. \quad (5.7)$$

Moreover the dimensionless energy per particle

$$\begin{aligned} E(\psi_1, \psi_0, \psi_{-1}) &= \int_{\mathbb{R}^d} \left[\sum_{j=-1}^1 \left(\frac{1}{2} |\nabla \psi_j|^2 + V_d |\psi_j|^2 - \Omega \bar{\psi}_j L_z \psi_j \right) + \frac{\lambda_n}{2} \rho^2 + \right. \\ &\quad \left. + \frac{\lambda_s}{2} (\rho_1^2 + \rho_{-1}^2 + 2\rho_1 \rho_0 + 2\rho_0 \rho_{-1} - 2\rho_1 \rho_{-1}) \right. \\ &\quad \left. + \lambda_s (\bar{\psi}_{-1} \psi_0^2 \bar{\psi}_1 + \psi_{-1} \bar{\psi}_0^2 \psi_1) \right] d\mathbf{x}, \quad (5.8) \end{aligned}$$

is also conserved.

For the total angular momentum expectation of spinor F=1 BEC, i.e.,

$$\langle L_z \rangle(t) := \langle L_z^1 \rangle(t) + \langle L_z^0 \rangle(t) + \langle L_z^{-1} \rangle(t), \quad (5.9)$$

where $\langle L_z^j \rangle(t) = \int_{\mathbb{R}^d} \bar{\psi}_j(\mathbf{x}, t) L_z \psi_j(\mathbf{x}, t) d\mathbf{x}$ ($j=1,0,-1$), we have the following lemma,

Lemma 5.2.1 *Suppose $\psi_j(\mathbf{x}, t)$ is the solution of the generalized GPEs (5.5), then we have*

$$\frac{d\langle L_z \rangle(t)}{dt} = \sum_{j=-1}^1 (\gamma_x^2 - \gamma_y^2) \int_{\mathbb{R}^d} xy |\psi_j(\mathbf{x}, t)|^2 d\mathbf{x}, \quad t \geq 0. \quad (5.10)$$

Moreover, if $\gamma_x = \gamma_y$, we can obtain that $\frac{d\langle L_z \rangle(t)}{dt} = 0$, i.e., the total angular momentum expectation is conserved.

For the total condensate width of spinor F=1 BEC in 2D, i.e.,

$$\delta(t) = \sum_{j=-1}^1 \left(\delta_x^j(t) + \delta_y^j(t) \right), \quad (5.11)$$

where $\delta_\alpha^j(t) = \int_{\mathbb{R}^2} \alpha^2 |\psi_j(x, y, t)|^2 dx dy$ ($\alpha = x$ or y), we have the following lemma,

Lemma 5.2.2 *Suppose $\psi_j(x, y, t)$ is the solution of the generalized GPEs (5.5) in 2D and $\gamma_x = \gamma_y$ ($:= \gamma_r$), then we have*

$$\frac{d^2 \delta(t)}{dt^2} = -4\gamma_r^2 \delta(t) + 4E(\psi_1, \psi_0, \psi_{-1}) + 4\Omega \langle L_z \rangle(0), \quad t \geq 0, \quad (5.12)$$

which is a second order ODE with constant coefficients for $\delta(t)$, i.e., $\delta(t)$ is periodic with respect to time.

Proofs for the lemma 5.2.1 and the lemma 5.2.2 can be followed as the way done in [19].

5.3 A TSSP method for the generalized GPEs

In this section we design a TSSP method to solve the generalized GPEs in order to study the dynamics of spinor F=1 BEC within a magnetic field. In practical computation, we always truncate the equations (5.5) in a bounded domain with homogeneous Dirichlet boundary conditions:

$$\begin{aligned} i \frac{\partial}{\partial t} \psi_1 &= \{H + \lambda_n \rho\} \psi_1 + \lambda_s (\rho_1 + \rho_0 - \rho_{-1}) \psi_1 + \lambda_s \bar{\psi}_{-1} \psi_0^2 + B \psi_0, \\ i \frac{\partial}{\partial t} \psi_0 &= \{H + \lambda_n \rho\} \psi_0 + \lambda_s (\rho_1 + \rho_{-1}) \psi_0 + 2\lambda_s \psi_1 \psi_{-1} \bar{\psi}_0 + \bar{B} \psi_1 + B \psi_{-1}, \end{aligned}$$

$$\begin{aligned}
i \frac{\partial}{\partial t} \psi_{-1} &= \{H + \lambda_n \rho\} \psi_{-1} + \lambda_s (\rho_0 + \rho_{-1} - \rho_1) \psi_{-1} + \lambda_s \bar{\psi}_1 \psi_0^2 + \bar{B} \psi_0, \quad (5.13) \\
\psi_j(\mathbf{x}, t) &= 0, \quad \mathbf{x} \in \Gamma = \partial\Omega_x, \\
\psi_j(\mathbf{x}, 0) &= \psi_{j,0}(\mathbf{x}), j = 1, 0, -1, \quad \mathbf{x} \in \Omega_x,
\end{aligned}$$

where $H = -\frac{1}{2}\Delta + V_d(\mathbf{x}) - \Omega L_z$ and $B := B(\mathbf{x})$ describes the external Ioffe-Pitchard magnetic field \mathbf{B} used in the experiments [24, 107]. The initial data in the equations (5.13) are chosen such that $\sum_{j=-1}^1 \|\psi_{j,0}(\mathbf{x})\|^2 = 1$.

5.3.1 Time-splitting

We choose a time step size $\Delta t > 0$. For $n = 0, 1, 2, \dots$, from time $t = t_n$ to $t = t_{n+1}$, first one solves

$$i \partial_t \psi_j(\mathbf{x}, t) = -\frac{1}{2} \nabla^2 \psi_j(\mathbf{x}, t) - \Omega L_z \psi_j(\mathbf{x}, t), \quad j = 1, 0, -1 \quad (5.14)$$

for the time step of length Δt , second one solves

$$\begin{aligned}
i \partial_t \psi_1 &= (V_d(\mathbf{x}) + \lambda_n \rho + \lambda_s (\rho_1 + \rho_0 - \rho_{-1})) \psi_1, \\
i \partial_t \psi_0 &= (V_d(\mathbf{x}) + \lambda_n \rho + \lambda_s (\rho_1 + \rho_{-1})) \psi_0, \\
i \partial_t \psi_{-1} &= (V_d(\mathbf{x}) + \lambda_n \rho + \lambda_s (-\rho_1 + \rho_0 + \rho_{-1})) \psi_{-1}
\end{aligned} \quad (5.15)$$

for the same time step, and for $t \in [t_n, t_{n+1}]$, finally one solves

$$i \frac{\partial}{\partial t} \Psi(\mathbf{x}, t) = C \Psi(\mathbf{x}, t), \quad (5.16)$$

where $\Psi(\mathbf{x}, t) = (\psi_1(\mathbf{x}, t), \psi_0(\mathbf{x}, t), \psi_{-1}(\mathbf{x}, t))^T$ and

$$C = \begin{pmatrix} 0 & \lambda_s \psi_0 \bar{\psi}_{-1} + B & 0 \\ \lambda_s \bar{\psi}_0 \psi_{-1} + \bar{B} & 0 & \lambda_s \bar{\psi}_0 \psi_1 + B \\ 0 & \lambda_s \psi_0 \bar{\psi}_1 + \bar{B} & 0 \end{pmatrix}.$$

For any $t \in [t_n, t_{n+1}]$, the equations (5.14) are decoupled and each equation for $\psi_j(\mathbf{x}, t)$ ($j=1,0,-1$) can be solved using the Fourier Pseudospectral method presented

in section 3.2. For the equations (5.15), since $\rho_j(\mathbf{x}, t) = |\psi_j(\mathbf{x}, t)|^2$ are conserved for any $t \in [t_n, t_{n+1}]$, they can be solved exactly as follows:

$$\begin{aligned}\psi_1(\mathbf{x}, t) &= e^{-i(V_d(\mathbf{x}) + \lambda_n \rho(\mathbf{x}, t_n) + \lambda_s(\rho_1(\mathbf{x}, t_n) + \rho_0(\mathbf{x}, t_n) - \rho_{-1}(\mathbf{x}, t_n)))(t - t_n)} \psi_1(\mathbf{x}, t_n), \\ \psi_0(\mathbf{x}, t) &= e^{-i(V_d(\mathbf{x}) + \lambda_n \rho(\mathbf{x}, t_n) + \lambda_s(\rho_1(\mathbf{x}, t_n) + \rho_{-1}(\mathbf{x}, t_n)))(t - t_n)} \psi_0(\mathbf{x}, t_n), \\ \psi_{-1}(\mathbf{x}, t) &= e^{-i(V_d(\mathbf{x}) + \lambda_n \rho(\mathbf{x}, t_n) + \lambda_s(\rho_0(\mathbf{x}, t_n) + \rho_{-1}(\mathbf{x}, t_n) - \rho_1(\mathbf{x}, t_n)))(t - t_n)} \psi_{-1}(\mathbf{x}, t_n).\end{aligned}$$

For the equations (5.16), we integrate (5.16) over the time interval $[t_n, t_{n+1}]$, approximate the integral by the trapezoidal quadrature [20], and we get

$$\begin{aligned}\Psi(t_{n+1}) &= \exp\left(-i \int_{t_n}^{t_{n+1}} C(\Psi(\tau)) d\tau\right) \Psi^n \\ &\approx \exp\left(-i \frac{\Delta t}{2} [C(\Psi^n) + C(\Psi^{n+1})]\right) \Psi^n \\ &\approx \exp\left(-i \frac{\Delta t}{2} [C(\Psi^n) + C(\Psi^{(1)})]\right) \Psi^n \\ &:= \exp(-i \Delta t M(\Psi^n)) \Psi^n,\end{aligned}\tag{5.17}$$

where $\Psi^n = \Psi(t_n)$ and $\Psi^{(1)}$ is an approximation of $\Psi(t_{n+1})$ and can be computed from the ODEs (5.16) by any explicit method. Here we use the Forward Euler method to compute $\Psi^{(1)} = \Psi^n - i \Delta t C(\Psi^n) \Psi^n$, and obtain

$$M(\Psi^n) = \frac{1}{2} [C(\Psi^n) + C(\Psi^{(1)})] := \begin{pmatrix} 0 & b_{12} & 0 \\ \bar{b}_{12} & 0 & b_{23} \\ 0 & \bar{b}_{23} & 0 \end{pmatrix},\tag{5.18}$$

where $b_{12} = \frac{\lambda_s}{2}(\psi_0^n \bar{\psi}_{-1}^n + \psi_0^{(1)} \bar{\psi}_{-1}^{(1)}) + B$, $b_{23} = \frac{\lambda_s}{2}(\psi_1^n \bar{\psi}_0^n + \psi_1^{(1)} \bar{\psi}_0^{(1)}) + B$. Since C is Hermitian, i.e., $\bar{C}^T = C$, thus $M = M(\Psi^n)$ is also a Hermitian. Therefore, we can find explicitly a unitary matrix P with $P^{-1} = (\bar{P})^T$ and a real diagonal matrix Λ such that

$$M = P \Lambda P^{-1},$$

where

$$\Lambda = \Lambda(\Psi^n) = \begin{pmatrix} 0 & 0 & 0 \\ 0 & \alpha & 0 \\ 0 & 0 & -\alpha \end{pmatrix}, \quad P = P(\Psi^n) = \frac{1}{\alpha \sqrt{2}} \begin{pmatrix} \sqrt{2} b_{23} & b_{12} & -b_{12} \\ 0 & \alpha & \alpha \\ -\sqrt{2} b_{12} & \bar{b}_{23} & -\bar{b}_{23} \end{pmatrix},$$

for $\alpha = \sqrt{|b_{12}|^2 + |b_{23}|^2} > 0$; P is an identity matrix if $\alpha = 0$. Thus we can finally obtain a one-step approximation of the ODEs (5.16) as

$$\Psi^{n+1} = P \exp(-i\Delta t \Lambda) P^{-1} \Psi^n.$$

5.3.2 Discretization in 2D

When $d=2$ in (5.13), we choose the same mesh (x_j, y_k) as those defined in (3.17). Let $\psi_{r,jk}^n$ be the approximation of $\psi_r(x_j, y_k, t_n)$. From time t_n to time t_{n+1} , we apply the second-order time-splitting [36, 126] and obtain the following algorithm of the TSSP method for the generalized GPEs (5.13) in 2D:

$$\begin{aligned} \psi_{r,jk}^{(1)} &= \sum_{p=-M/2}^{M/2-1} e^{-i\Delta t(\mu_p^2 + 2\Omega y_k \mu_p)/4} \widehat{(\psi_{r,k}^n)}_p e^{i\mu_p(x_j - a)}, \quad 0 \leq j \leq M, \quad 0 \leq k \leq N, \\ \psi_{r,jk}^{(2)} &= \sum_{q=-N/2}^{N/2-1} e^{-i\Delta t(\lambda_q^2 - 2\Omega x_j \lambda_q)/4} \widehat{(\psi_{r,j}^{(1)})}_q e^{i\lambda_q(y_k - c)}, \quad r = 1, 0, -1, \\ \Psi_{jk}^{(3)} &= P(\Psi_{jk}^{(2)}) \exp\left(-\frac{i\Delta t}{2} \Lambda(\Psi_{jk}^{(2)})\right) P^{-1}(\Psi_{jk}^{(2)}) \Psi_{jk}^{(2)}, \\ \psi_{1,jk}^{(4)} &= e^{-i\Delta t(V(x_j, y_k) + \lambda_n \rho_{jk}^{(3)} + \lambda_s(\rho_{1,jk}^{(3)} + \rho_{0,jk}^{(3)} - \rho_{-1,jk}^{(3)}))} \psi_{1,jk}^{(3)}, \\ \psi_{0,jk}^{(4)} &= e^{-i\Delta t(V(x_j, y_k) + \lambda_n \rho_{jk}^{(3)} + \lambda_s(\rho_{1,jk}^{(3)} + \rho_{-1,jk}^{(3)}))} \psi_{0,jk}^{(3)}, \\ \psi_{-1,jk}^{(4)} &= e^{-i\Delta t(V(x_j, y_k) + \lambda_n \rho_{jk}^{(3)} + \lambda_s(\rho_{0,jk}^{(3)} + \rho_{-1,jk}^{(3)} - \rho_{1,jk}^{(3)}))} \psi_{-1,jk}^{(3)}, \\ \Psi_{jk}^{(5)} &= P(\Psi_{jk}^{(4)}) \exp\left(-\frac{i\Delta t}{2} \Lambda(\Psi_{jk}^{(4)})\right) P^{-1}(\Psi_{jk}^{(4)}) \Psi_{jk}^{(4)}, \\ \psi_{r,jk}^{(6)} &= \sum_{q=-N/2}^{N/2-1} e^{-i\Delta t(\lambda_q^2 - 2\Omega x_j \lambda_q)/4} \widehat{(\psi_{r,j}^{(5)})}_q e^{i\lambda_q(y_k - c)}, \\ \psi_{r,jk}^{n+1} &= \sum_{p=-M/2}^{M/2-1} e^{-i\Delta t(\mu_p^2 + 2\Omega y_k \mu_p)/4} \widehat{(\psi_{r,k}^{(6)})}_p e^{i\mu_p(x_j - a)}, \end{aligned} \quad (5.19)$$

where $\Psi_{jk}^* = \Psi(x_j, y_k, *)$. We remark that the presented TSSP method (5.19) for the generalized equations is second order in time and of spectral accuracy in space which will be shown in section 5.4.

5.3.3 Stability

When $d = 2$, let $\psi_{r,jk}^n$ ($r=1,0,-1$) be the approximation of $\psi_r(x_j, y_k, t_n)$ and ψ_r^n be the solution vector with component $\psi_{r,jk}^n$.

For the *stability* of the time-splitting spectral approximations (5.19) for the 2D generalized GPEs (5.13), we have the following lemma, which shows that the total density $\sum_{r=-1}^1 \|\psi_r(\mathbf{x}, t)\|^2$ is conserved in the discretized level.

Lemma 5.3.1 *The time-splitting spectral scheme (5.19) is unconditionally stable. In fact, for every mesh size and time step size $\Delta t > 0$,*

$$\sum_{r=-1}^1 \|\psi_r^n\|_{l^2}^2 = \sum_{r=-1}^1 \|\psi_r^0\|_{l^2}^2. \quad (5.20)$$

Proof: Follows the line of the analogous results for the linear and nonlinear Schrödinger equations in [10, 11].

5.4 Numerical results

In this section, we first use exact solutions of a special generalized GPEs in 1D to test the accuracy of the TSSP method. We next look into whether the numerical results obtained agree with the analytical results presented in the section 5.2 and one of the previous numerical studies on generation of solitons [107]. We finally apply the TSSP method to solve the generalized GPEs (5.13) in 2D in order to study the dynamic generation of vortices in the spinor F=1 BEC within an Ioffe-Pritchard magnetic field, and to investigate the effect of this magnetic field on the vortex lattice dynamics of the rotating spinor BEC.

5.4.1 Accuracy tests

To test the accuracy of our numerical method in 1D, we take $\lambda_n = \lambda_s = -1$ in the generalized GPEs (5.13) in 1D with trap potential $V(x) = 0$ and magnetic field

$B(x) = 0$. These equations admit the following solution [67]:

$$\begin{aligned}\psi_1^{exact}(x, t) &= \beta k_R \operatorname{sech}(x_R + \rho/2) e^{ix_I}, \\ \psi_0^{exact}(x, t) &= \alpha k_R \operatorname{sech}(x_R + \rho/2) e^{ix_I}, \\ \psi_{-1}^{exact}(x, t) &= \gamma k_R \operatorname{sech}(x_R + \rho/2) e^{ix_I},\end{aligned}$$

where $\alpha^2 + \beta^2 + \gamma^2 = 1$, $\alpha^2 = 2\beta\gamma$, $x_R = k_R(\sqrt{2}x - 2k_I t)$, $x_I = k_I\sqrt{2}x + (k_R^2 - k_I^2)t$ and $\rho = -2\ln(2k_R)$ ($k_R, k_I, \alpha, \beta, \gamma$ are real constants). In our calculations we take $k_R = 0.5, k_I = 0.75, \alpha = \frac{4}{17}\sqrt{2}, \beta = \frac{16}{17}, \gamma = \frac{1}{17}$. Table 5.1 shows that the method has the spectral accuracy in space. Table 5.2 shows that the method have the second accuracy in time.

Δx	1.25	5/8	5/16
	2.571E-2	1.547E-4	7.037E-7

Table 5.1: Discretization error $\max_{j=1,0,-1} \|\psi_j^{exact}(t) - \psi_j^{(\Delta x, \Delta t)}(t)\|_{l^2}$ at $t = 0.5$ in space for 1D, $\Delta t = 10^{-4}$.

Δt	1/20	1/40	1/80	1/160
	2.902E-5	7.278E-6	1.918E-6	7.7504E-7

Table 5.2: Discretization error $\max_{j=1,0,-1} \|\psi_j^{exact}(t) - \psi_j^{(\Delta x, \Delta t)}(t)\|_{l^2}$ at $t = 0.5$ in time for 1D, $\Delta x = 5/128$.

To compare the numerical results obtained from the TSSP method with the analytical results of the generalized GPEs (5.13) in 1D, we solve the equations (5.13) with $B(x) = 0$, $\lambda_n = 100$ and $\lambda_s = 2$ on $[-12, 12]$, and prepare $\psi_1(x, 0) = \psi_{-1}(x, 0) = \frac{\sqrt{0.05}}{\pi^{\frac{1}{4}}} e^{-\frac{x^2}{2}}$ and $\psi_0(x, 0) = \frac{\sqrt{0.9}}{\pi^{\frac{1}{4}}} e^{-\frac{x^2}{2}}$ as initial conditions. Figure 5.1 (a) and (b) show that the method numerically conserves the total normalization, the magnetization and the energy in 1D.

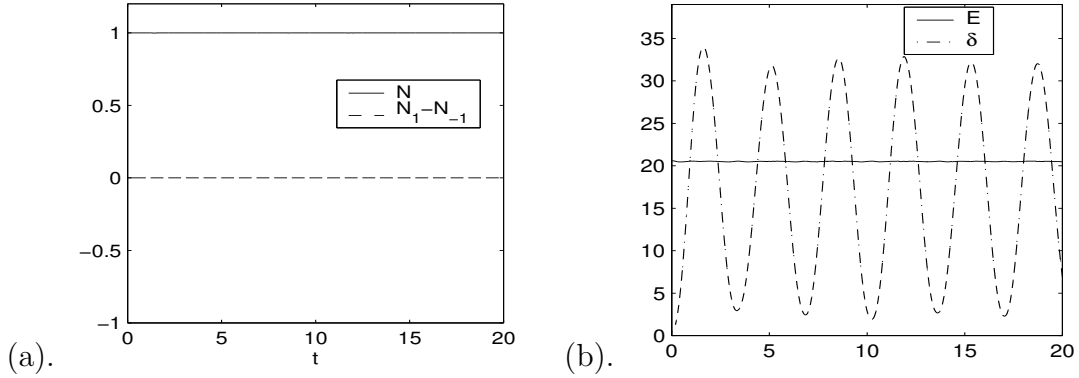


Figure 5.1: (a) Time evolutions of the total normalization $N := N_1 + N_0 + N_{-1}$ ($N_j = N_j(\psi_j)$, $j=1,0,-1$) and the magnetization $N_1 - N_{-1}$; (b) the energy $E := E(\psi_1, \psi_0, \psi_{-1})$ and the total condensate width $\delta := \sum_{j=1,0,-1} \int_{-12}^{12} x^2 |\psi_j(x, t)|^2 dx$ with $\gamma_x = 1.0$ in 1D.

Furthermore, to compare the numerical results obtained from the TSSP method with the analytical results of the generalized GPEs (5.13) in 2D, we solve the equations with $B(x, y) = 0$, $\lambda_n = 100$ and $\lambda_s = 2$ on the domain $\Omega_x = [-8, 8] \times [-8, 8]$, and prepare $\psi_1(x, y, 0) = \psi_{-1}(x, y, 0) = \frac{\sqrt{0.05}}{\sqrt{\pi}} e^{-\frac{(x^2+y^2)}{2}}$ and $\psi_0(x, y, 0) = \frac{\sqrt{0.9}}{\sqrt{\pi}} e^{-\frac{(x^2+y^2)}{2}}$. When we have a symmetric trap, i.e., $\gamma_x = \gamma_y$, the method numerically conserves the total norm, the magnetization, the total angular momentum and the energy in 2D; the total condensate width changes periodically (c.f. Figure 5.2). However, when we have a non-symmetric trap, i.e., $\gamma_x \neq \gamma_y$, the total condensate width does not change periodically. The total angular momentum is not conserved numerically either (c.f. Figure 5.3). The numerical results presented in Figures 5.2 and 5.3 agree very well with those analytical properties shown in the section 5.2.

Finally, we solve the equations (5.13) in 1D with $\lambda_n = 100$, $\lambda_s = 2$, and $B(x) = -\frac{1}{\sqrt{2}}(x - x_0)$ on $[-40, 40]$ using the newly proposed TSSP method. The mesh size $\Delta x = 5/128$. We prepare initial data with type I: $\psi_0(x, 0) = \frac{1}{\pi^{\frac{1}{4}}} e^{-\frac{x^2}{2}}$ and $\psi_1(x, 0) = \psi_{-1}(x, 0) = 0$. From Figure 5.4, we can find that: (a) more solitons will be formed with increasing time if the spinor BEC held in the magnetic field $B(x) = -\frac{1}{\sqrt{2}}(x - x_0)$; (b) the centers of the solitons can be shifted by changing the value of x_0 : if

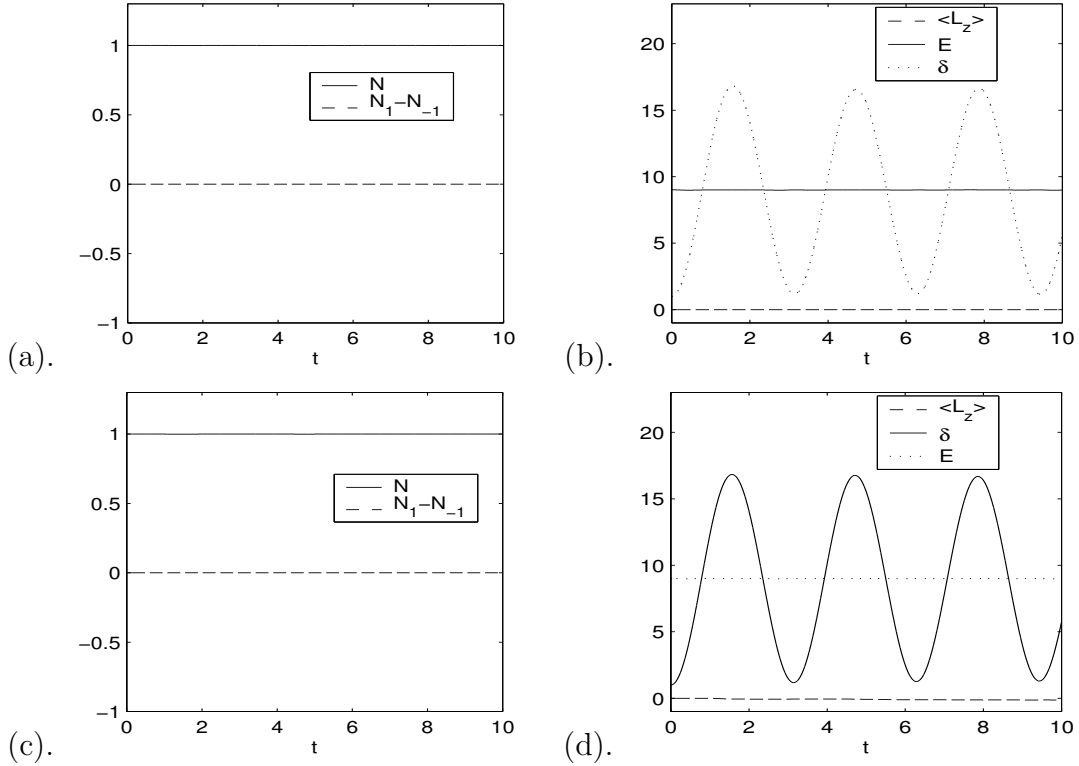


Figure 5.2: Time evolutions of the total normalization $N := N_1 + N_0 + N_{-1}$ ($N_j = N_j(\psi_j)$, $j = 1, 0, -1$) and the magnetization $N_1 - N_{-1}$ (left column), the total angular momentum $\langle L_z \rangle := \Omega \langle L_z \rangle(t)$, the energy $E := E(\psi_1, \psi_0, \psi_{-1})$ and the total condensate width $\delta := \delta(t)$ with $\gamma_x = \gamma_y = 1.0$ in 2D (right column). In (a) & (b), $\Omega = 0$; in (c) & (d), $\Omega = 0.9$.

$x_0 > 0$, then the centers of the solitons will move to left from their original positions; if $x_0 < 0$, then the centers of solitons will move to right. Similar numerical results are also observed in [107].

5.4.2 Generation of vortices

Recently a coreless vortex was phase-printed in the spinor $F=1$ condensates, which are held in an Ioffe-Pritchard magnetic field [82]. To understand this physical phenomena, theoretically one models this field in 2D by assuming $B(x, y) = b_x[(x - x_0) + i(y - y_0)]^n$ where n is an integer, x_0 and y_0 are real constants [107]. In this

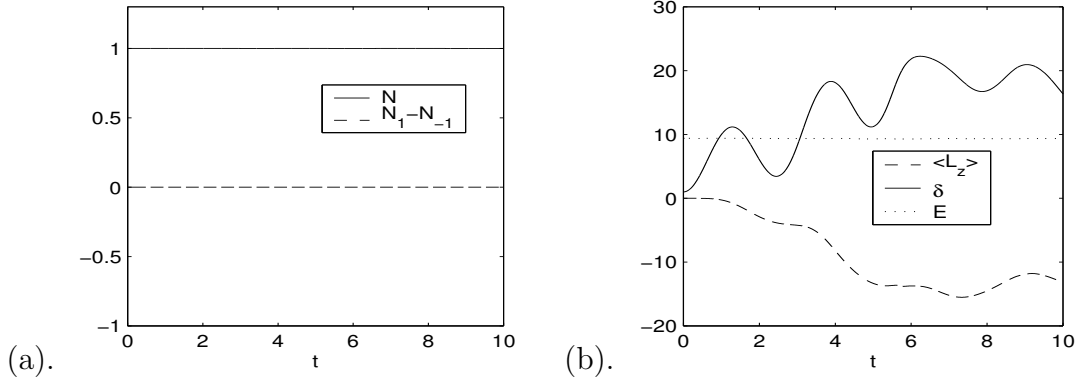


Figure 5.3: (a) Time evolutions of the total normalization $N := N_1 + N_0 + N_{-1}$ ($N_j = N_j(\psi_j)$, $j=1,0,-1$) and the magnetization $N_1 - N_{-1}$; (b) the total angular momentum $\langle L_z \rangle := \Omega \langle L_z \rangle(t)$, the energy $E := E(\psi_1, \psi_0, \psi_{-1})$ and the total condensate width $\delta := \delta(t)$ with $\gamma_x = 1$ and $\gamma_y = 1.5$ and $\Omega = 0.9$ in 2D.

subsection, we present a direct numerical simulation to understand the formation of coreless vortex in the spinor F=1 BEC held in this magnetic field.

We solve the equations (5.13) in 2D with $\lambda_n = 100$, $\lambda_s = 2$ and $\Omega = 0$ by using the proposed TSSP method. The computation domain $(x, y) \in [-10, 10] \times [-10, 10]$ and mesh size $\Delta x = \Delta y = 5/32$. $B(x, y) = b_x[(x - x_0) + i(y - y_0)]$ with $b_x = -\frac{0.05}{\sqrt{2}}$ or $-\frac{1}{\sqrt{2}}$. In the 2D calculations, we prepare two kinds of initial data, type II: $\psi_0(x, y, 0) = \frac{1}{\sqrt{\pi}} e^{-\frac{(x^2+y^2)}{2}}$ and $\psi_1(x, y, 0) = \psi_{-1}(x, y, 0) = 0$; type III: $\psi_1(x, y, 0) = \frac{-1}{\sqrt{\pi}} e^{-\frac{(x^2+y^2)}{2}}$ and $\psi_0(x, y, 0) = \psi_{-1}(x, y, 0) = 0$.

From Figures 5.5, 5.6, we find that vortex arises up in the dynamics of the spinor F=1 BEC if one turns on the Ioffe-Pritchard magnetic field; the vortex core lies on the center of the magnetic field, i.e., (x_0, y_0) . Furthermore if one increases the amplitude of the magnetic field, i.e., the value of $|b_x|$, we find that, from Figures 5.7, 5.8, vortex rings will show up in the dynamics of the spinor F=1 BEC. One might find that numerical results shown in Figures 5.5, 5.6, 5.7 and 5.8 could be compared with phase-imprinted figures on the coreless vortex, which are observed in spinor BEC experiments [82].

Moreover, prepared with initial data type II, if we let the magnetic field $B(x, y) =$

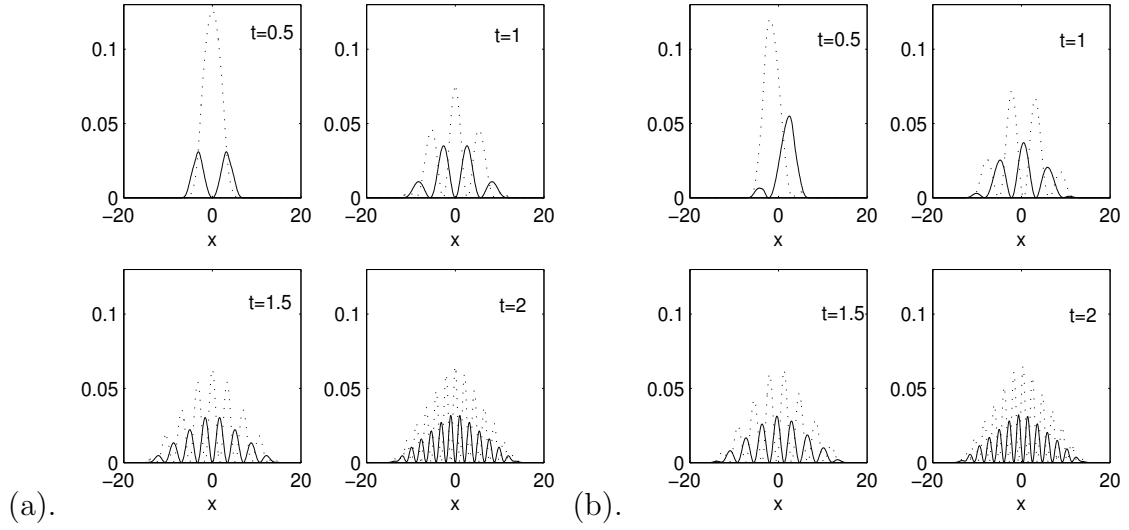


Figure 5.4: Generation of solitons in 1D with initial data type I, dotted line for spin-(± 1) density $|\psi_{\pm 1}(x, t)|^2$; solid line for spin-0 density $|\psi_0(x, t)|^2$ (a) $x_0 = 0$; (b) $x_0 = 5$.

$-\frac{0.05}{\sqrt{2}}(x+iy)^2$, we find that core sizes of vortices in Figure 5.9(a) are bigger than those in Figure 5.5(a); if we let the magnetic field $B(x, y) = -\frac{0.05}{\sqrt{2}}(x+iy)^3$, we find that vortex rings appear up in Figure 5.9(b), while no such rings are observed in Figure 5.5(a), where it is applied with the magnetic field $B(x, y) = -\frac{0.05}{\sqrt{2}}(x+iy)$. Similar observations can be found in Figure 5.10(a)&(b), which are obtained by solving the equations (5.13) with the same parameters but starting from initial data type III. These complex configurations of vortices occur perhaps because the higher-order magnetic field might be able to create vortices with higher-order winding numbers [107].

5.4.3 Dynamics of a vortex lattice

In 2D, when $\lambda_n \gg \lambda_s$, the ground state of the rotating spinor F=1 BEC that is not contained in a magnetic field, can be approximated to be that of a rotating three-component BEC. In this ground state, each spin- j ($j=1,0,-1$) density has an

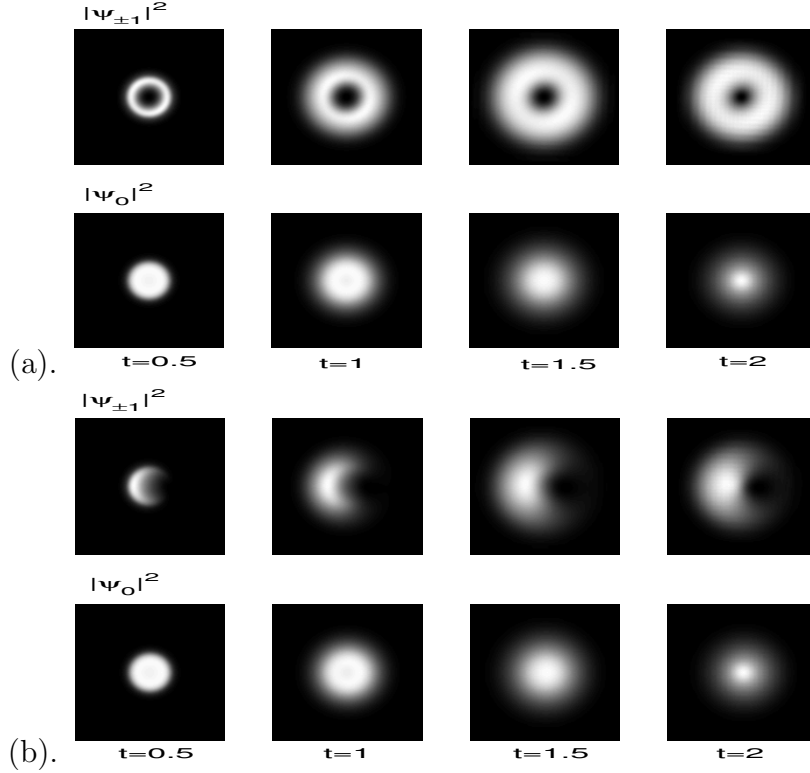


Figure 5.5: Image plots of the density $|\psi_j|^2$ ($j=1,0,-1$) at different times for spinor BEC within a magnetic field $B(x, y) = -\frac{0.05}{\sqrt{2}}[(x - x_0) + i(y - y_0)]$ with initial data type II. (a) $(x_0, y_0) = (0, 0)$; (b) $(x_0, y_0) = (2, 0)$.

identical vortex lattice if Ω is near γ_{xy} . We extended the GFDN method proposed in Chapter 2 to find one of the ground states of rotating three-component BEC with $\lambda_n = 1000$, $\Omega = 0.85$, and a symmetric trap $V_2(x, y) = \frac{1}{2}(x^2 + y^2)$. We prepared the obtained ground state as the initial condition of the equations (5.13). We then solved the equations (5.13) in 2D with $\lambda_n = 1000$, $\lambda_s = 20$ and $\Omega = 0.85$ by using the proposed TSSP method. The computation domain $(x, y) \in [-12, 12] \times [-12, 12]$ and mesh size $\Delta x = \Delta y = 3/16$. $B(x, y) = -\frac{0.05}{\sqrt{2}}(x + iy)$. Figure 5.11 shows the effect of this magnetic field on the vortex lattice where only the spin-0 density has the vortex lattice initially. Figure 5.12 shows the effect of this magnetic field on the vortex lattice where only the spin- -1 density has the vortex lattice initially. From Figures 5.11, 5.12, we find that the magnetic field can disturb the vortex lattice into

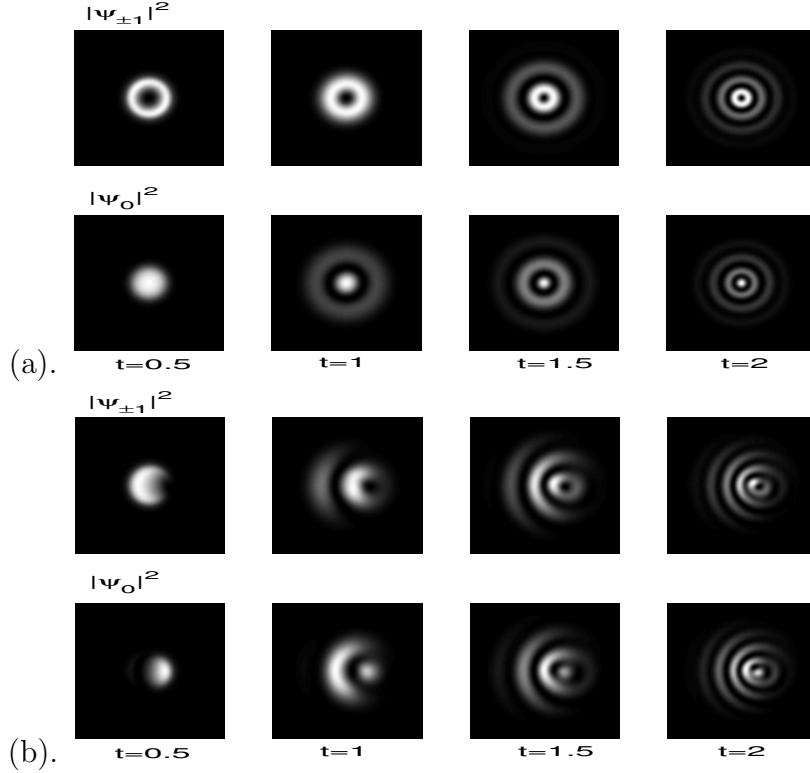


Figure 5.6: Image plots of the density $|\psi_j|^2$ ($j=1,0,-1$) at different times for spinor BEC within a magnetic field $B(x, y) = -\frac{1}{\sqrt{2}}[(x - x_0) + i(y - y_0)]$ with initial data type II. (a) $(x_0, y_0) = (0, 0)$; (b) $(x_0, y_0) = (2, 0)$.

a complex configuration. From these numerical results, we may predict that if the rotating spinor F=1 BEC is held in the Ioffe-Pritchard magnetic field, in the ground state, each spin of the rotating spinor BEC might not have a vortex lattice.

5.5 Conclusion

We propose a new TSSP method for the generalized GPEs. By using this spectrally accurate method to solve the generalized GPEs, we find that one can generate vortices in the spinor F=1 BEC if the BEC are held in the Ioffe-Pritchard magnetic trap; this magnetic field can quickly disturb the vortex lattice in the spinor BEC into complex structure.

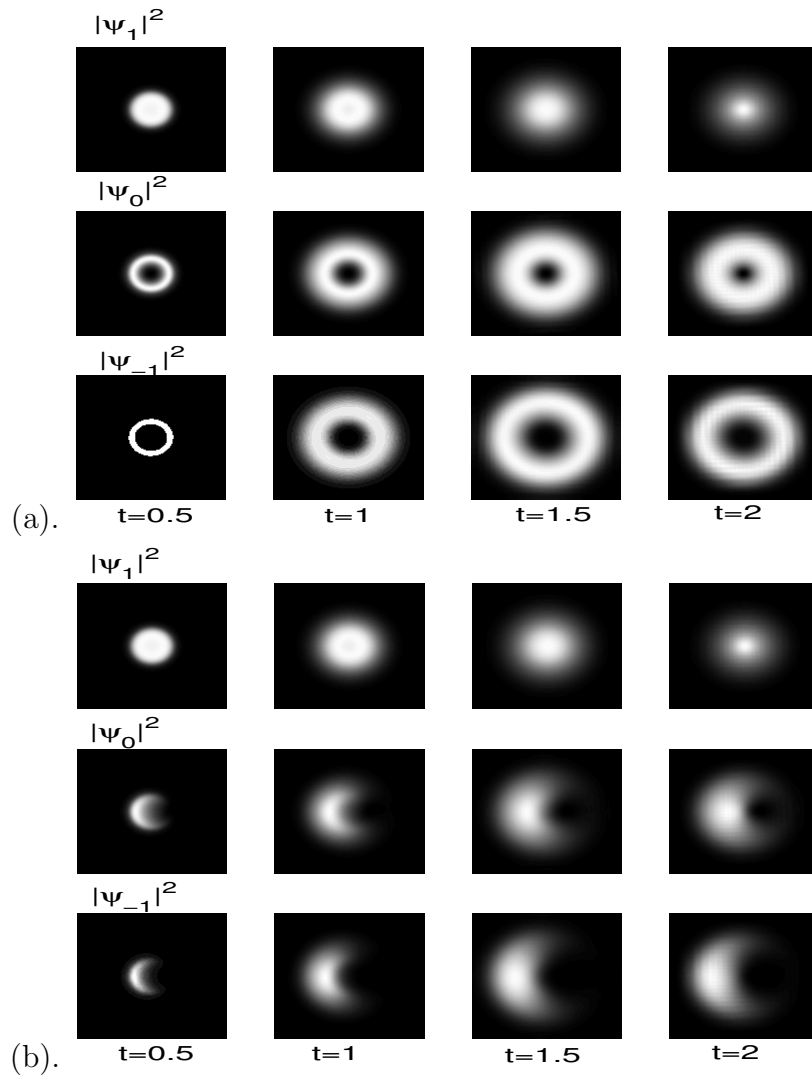


Figure 5.7: Image plots of the density $|\psi_j|^2$ ($j=1,0,-1$) at different times for spinor BEC within a magnetic field $B(x, y) = -\frac{0.05}{\sqrt{2}}[(x - x_0) + i(y - y_0)]$ with initial data type III. (a) $(x_0, y_0) = (0, 0)$; (b) $(x_0, y_0) = (2, 0)$.

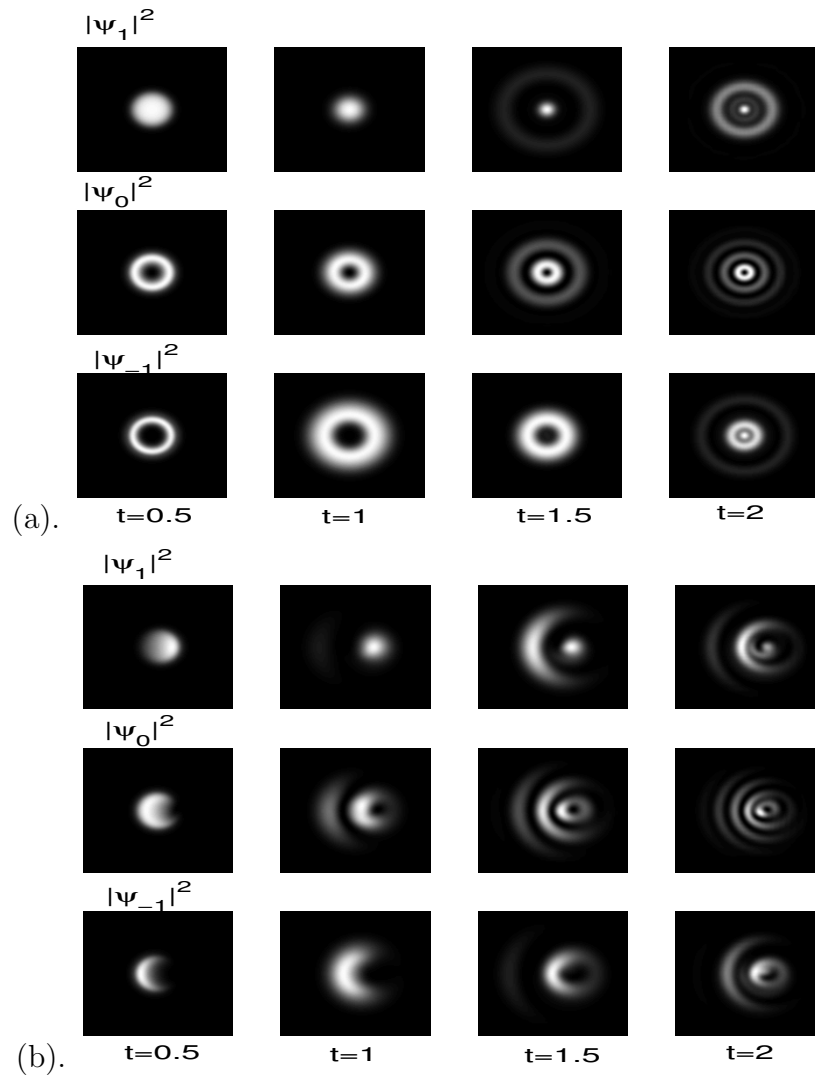


Figure 5.8: Image plots of the density $|\psi_j|^2$ ($j=1,0,-1$) at different times for spinor BEC within a magnetic field $B(x, y) = -\frac{1}{\sqrt{2}}[(x - x_0) + i(y - y_0)]$ with initial data type III. (a) $(x_0, y_0) = (0, 0)$; (b) $(x_0, y_0) = (2, 0)$.

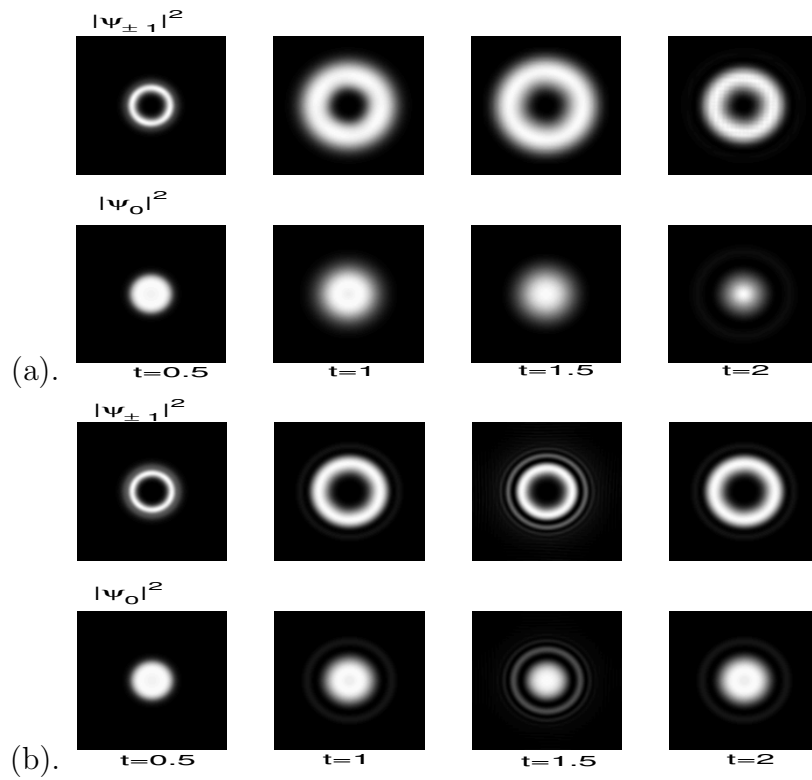


Figure 5.9: Image plots of the density $|\psi_j|^2$ ($j=1,0,-1$) at different times for spinor BEC within a magnetic field $B(x,y) =$ (a) $-\frac{0.05}{\sqrt{2}}(x+iy)^2$; (b) $-\frac{0.05}{\sqrt{2}}(x+iy)^3$ with initial data type II.

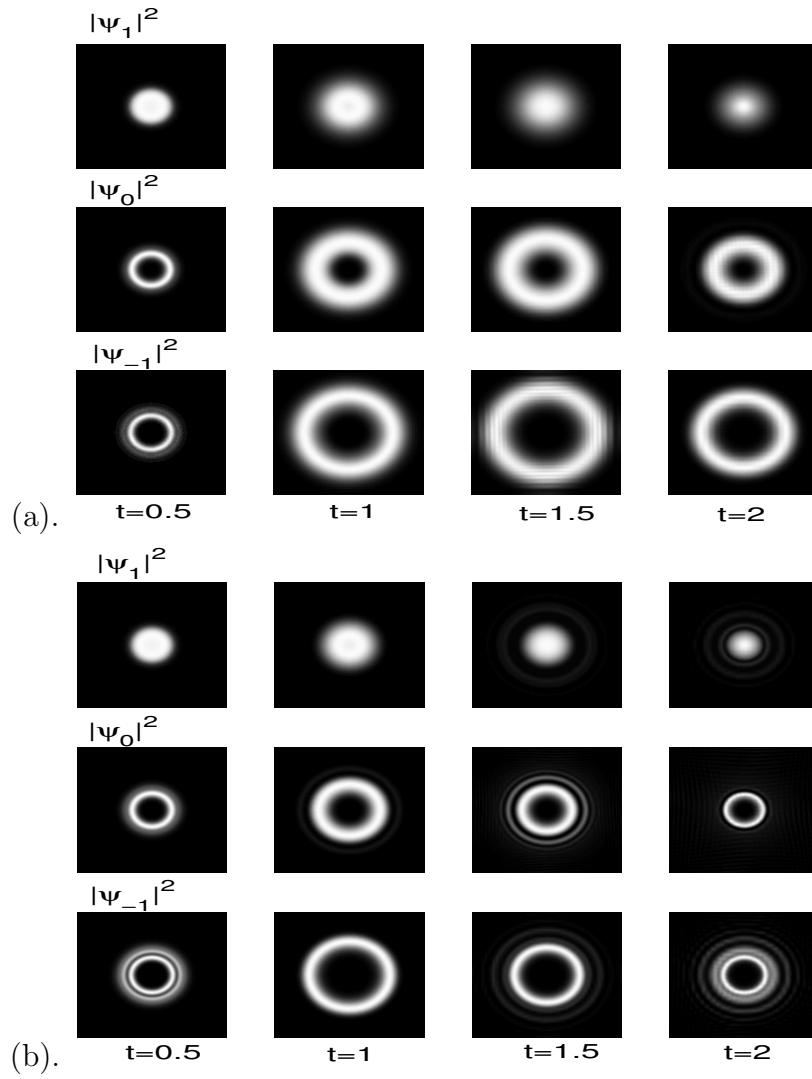


Figure 5.10: Image plots of the density $|\psi_j|^2$ ($j=1,0,-1$) at different times for spinor BEC within a magnetic field $B(x,y) =$ (a) $-\frac{0.05}{\sqrt{2}}(x+iy)^2$; (b) $-\frac{0.05}{\sqrt{2}}(x+iy)^3$ with initial data type III.

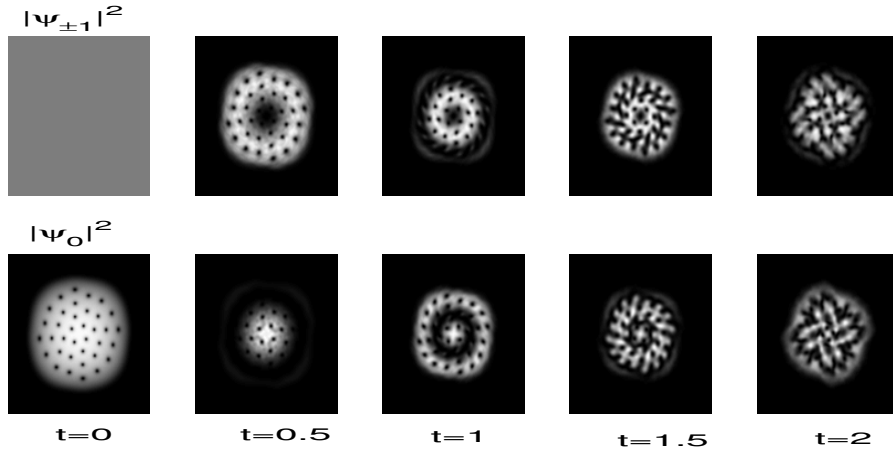


Figure 5.11: Image plots of the density $|\psi_j|^2$ ($j=1,0,-1$) at different times for vortex lattice dynamics of rotating spinor BEC within the magnetic field $B(x, y) = -\frac{0.05}{\sqrt{2}}(x + iy)$.

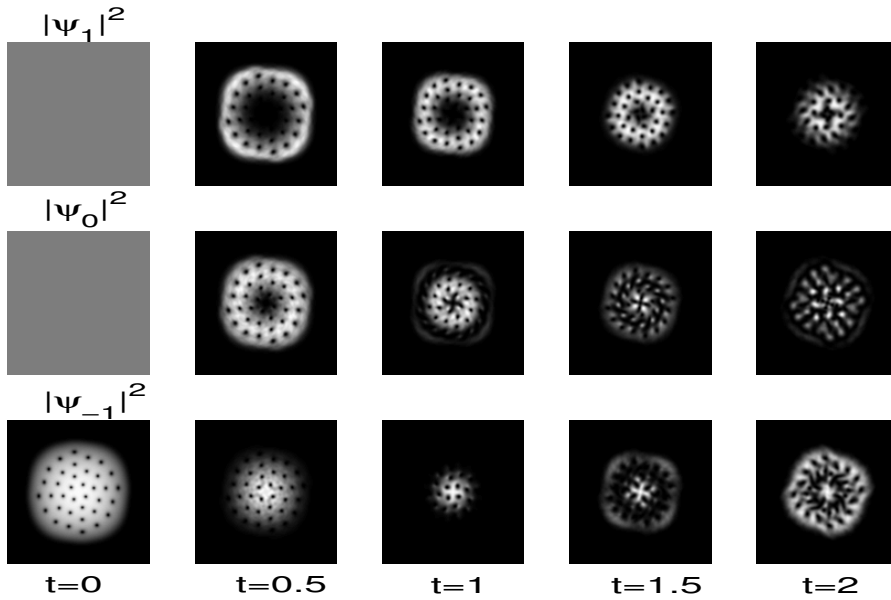


Figure 5.12: Image plots of the density $|\psi_j|^2$ ($j=1,0,-1$) at different times for vortex lattice dynamics of rotating spinor BEC within the magnetic field $B(x, y) = -\frac{0.05}{\sqrt{2}}(x + iy)$.

Concluding remarks and future work

We have analytically and numerically carried out an extensive study on quantized vortex states as well as their dynamics in the rotating one-component, two-component and spinor $F = 1$ BEC at extremely low temperature.

In the first part of the thesis, we studied quantized vortex states in the rotating one-component BEC at equilibrium and their dynamics. First we have shown that GFDN is a numerically efficient way to search the stationary solutions of the single GPE. We also justified the method mathematically. We have applied it to find three of the most important stationary solutions of the GPE: the ground state, symmetric states and central vortex states. From our numerical results, we found nucleation of quantized vortex states in the rotating one-component BEC at the equilibrium. The numerical results implied that the number of the quantized vortices depended on the angular momentum velocity represented by Ω . However, the stationary states such as the symmetric and central vortex states were independent of the angular momentum velocity. The numerical results on the ground state in the harmonic trap also implied that when $\Omega > \Omega^c$, by increasing the the value of Ω ($< \gamma_{xy}$), the number of vortices in the ground state increased from one vortex to several vortices until a large number of orderly vortices composed a vortex lattice. This reconfirmed some of the experimental results, although the exact relationship between the number of vortices and the angular momentum is not clear up to now. The numerical results

on the ground state in the harmonic plus quadratic trap implied that even when $\Omega > \gamma^{xy}$, the ground state might not have vortices. However, by increasing Ω further, we could finally see the giant vortex inside. We have also applied the GFDN method to search the ground state in 3D and found the bent vortex line in the ground state, but the detailed structure of it remains unclear, and this would need further work in the future.

We next proposed a new TSSP method to solve the time-dependent single GPE in a rotating frame. We have applied the TSSP method to study the dynamics of the quantized vortices after their formation at equilibrium in the rotating one-component BEC. By preparing the initial conditions with a vortex lattice, we found that the dynamics of the vortex lattice obtained through our numerical work agreed well with the experimental results on the non-equilibrium properties of the vortex lattice. We also dynamically generated the giant vortex, which could be compared with the experiment results. In future, we plan to apply the TSSP method to study vortex line dynamics in rotating BEC in 3D.

The second part of the thesis is to study quantized vortex states in the rotating two-component BEC at equilibrium and their dynamics. By applying the proposed GFDN, we searched the stationary solutions of the coupled GPEs such as ground state solution, symmetric states and central vortex states. Our numerical studies on ground state showed that diagrams of quantized vortices in the two-component BEC were richer than those found in rotating one-component BEC. This is perhaps one of the reasons that quantized vortices were first detected in two-component BEC [134]. In some ways, we may anticipate that superfluid phenomena like vortices are widespread in the rotating two-component BEC.

Next we proposed a new TSSP method for the coupled GPEs with a coupling constant. We have applied it to study the generation of topological modes such as quantized vortices and the vortex lattice dynamics of the rotating two-component BEC. Results on generation of topological modes also agreed well with those presented in [134]. If we prepared one component with vortex lattice initially, the

coupling term λ could determine the transferring speed of population from one component to another. If we prepared both components with vortex lattice initially, by changing the trap frequency, we found that the dynamical behaviors of the equilibrated vortices in the rotating two-component BEC were very rich. These dynamical behaviors are relatively novel and have not been reported in the literature. Our numerical results suggest that the trap frequency and interaction between atoms were probably two of the dominant factors for the shape of the quantized vortices. These are not surprising since the BEC at extremely low temperature is in the same state. From the numerical study of the dynamics of the quantized vortices, some of superfluid behavior revealed in the rotating two component BEC could be compared with the experimental results [2, 117]. Our numerical results reconfirmed that the coupled GPEs correctly described the dynamics of the BEC at very low temperature. In future work, we may use the TSSP method to solve the GPEs in three dimensions so as to study the dynamics of the quantized vortices in rotating two-component BEC, which are closer to the real experiments. We may use the numerical solutions of the equations in 3D to reveal other dynamical behaviors such as collective excitations or dynamics of the skyrimons or merons for the rotating two-component BEC.

In the last part of the thesis, we proposed a new TSSP method for the generalized GPEs and we found some complex dynamics on the vortices in the spinor $F=1$ BEC within an Ioffe-Pritchard magnetic trap. But we have not found the coherent dynamics of spinor $F=1$ condensates: two atoms with spin components -1 and $+1$ can coherently and reversibly scatter into final states containing two atoms with spin component 0 and vice versa, which have been observed in the experiments [31]. We will study such phenomena through direct simulation by using the TSSP method in future.

Recently in ^{87}Rb and ^{23}Na , condensates in the spinor $F=2$ states have been achieved [61, 115]. More recently, in Chromium, condensates in the spinor $F=3$ have been achieved at Stuttgart University [112]. The equations for describing the

dynamics of spinor $F=2$ and $F=3$ BEC are five and seven coupled nonlinear GPEs respectively. We believe that our GFDN and TSSP method can be easily extended to study the stationary states and dynamics respectively for both spinor $F=2$ and spinor $F=3$ BEC at extremely low temperature.

Despite that our newly proposed TSSP method is an efficient way to obtain the numerical solutions of the single GPE or coupled GPEs or generalized GPEs with periodic boundary conditions, it cannot be used to find the solutions of the single GPE or coupled GPEs or generalized GPEs with non-periodic boundary conditions. We may design more sophisticated time-splitting spectral method based on the Hermit or Laguerre functions or other orthogonal functions to solve the GPE or coupled GPEs or generalized GPEs with non-periodic boundary conditions in the future.

Our study is restricted to BEC at extremely low temperature, further work can be extended to BEC at low temperature. We plan to design more advanced numerical methods for the GPE coupled with the quantum Boltzmann equation or the Valsov equation or the two-fluid models, which are proposed to describe the nontrivial physics of the BEC at low temperature [72].

Bibliography

- [1] J. R. Abo-Shaeer, C. Raman, J. M. Vogels, and W. Ketterle, Observation of vortex lattices in Bose-Einstein condensates, *Science*, **292**, 476 (2001).
- [2] S. K. Adhikari, Numerical study of the coupled time-dependent Gross-Pitaevskii equation: Application to Bose-Einstein condensation, *Phys. Rev. E*, **63**, 056704 (2001).
- [3] S. K. Adhikari and P. Muruganandam, Effect of an impulsive force on vortices in a rotating Bose-Einstein condensate, *Phys. Rev. A*, **301**, 333-339 (2002).
- [4] A. Aftalion and Q. Du, Vortices in a rotating Bose-Einstein condensate: Critical angular velocities and energy diagrams in the Thomas-Fermi regime, *Phys. Rev. A*, **64**, 063603 (2001).
- [5] A. Aftalion and T. Riviere, Vortex energy and vortex bending for a rotating Bose-Einstein condensate, *Phys. Rev. A*, **64**, 043611 (2001).
- [6] A. Aftalion and I. Danaïla, Three-dimensional vortex configurations in a rotating Bose Einstein condensate, *Phys. Rev. A*, **68**, 023603 (2003).

-
- [7] M. H. Anderson, J. R. Ensher, M. R. Matthews, C. E. Wieman, and E. A. Cornell, Observation of Bose-Einstein Condensation in a Dilute Atomic Vapor, *Science*, **269**, 198 (1995).
- [8] W. Bao and Q. Du, Computing the ground state solution of Bose-Einstein condensates by a normalized gradient flow, *SIAM J. Sci. Comput.*, **25**, 1674-1697 (2004).
- [9] W. Bao, D. Jaksch, and P.A. Markowich, Numerical solution of the Gross-Pitaevskii Equation for Bose-Einstein condensation, *J. Comput. Phys.*, **187**, 318-342 (2003).
- [10] W. Bao and W. Tang, Ground state solution of trapped interacting Bose-Einstein condensate by directly minimizing the energy functional, *J. Comput. Phys.*, **187**, 230-254(2003).
- [11] W. Bao and Y. Zhang, Dynamics of the ground state and central vortex states in Bose-Einstein condensation, *Math. Mod. Meth. Appl. Sci.* , **15**, 1863-1896 (2005).
- [12] W. Bao and H. Wang, An efficient and spectrally accurate numerical method for computing dynamics of rotating Bose-Einstein condensates, *J. Comput. Phys.*, to appear.
- [13] W. Bao, H. Wang, and P. A. Markowich, Ground state, symmetric and central vortex state in rotating Bose-Einstein condensate, *Comm. Math. Sci.*, **3**, 57-88 (2005).
- [14] W. Bao, Shi Jin, and P.A. Markowich, On time-splitting spectral approximations for the Schrödinger equation in the semiclassical regime, *J. Comput. Phys.* **175**, 487 (2002).

-
- [15] W. Bao, Shi Jin, and P.A. Markowich, Numerical study of time-splitting spectral discretizations of nonlinear Schrödinger equations in the semi-classical regimes, *SIAM J. Sci. Comput.*, **25**, 27-64 (2003).
- [16] W. Bao, Ground states and dynamics of multi-component Bose-Einstein condensates, *SIAM Multiscale Modeling and Simulation*, **2**, 210-236 (2004).
- [17] W. Bao and J. Shen, A Fourth-order time-splitting Laguerre-Hermite pseudo-spectral method for Bose-Einstein condensates, *SIAM J. Sci. Comput.*, **26**, 2010-2028 (2005).
- [18] W. Bao, D. Jaksch, and P.A. Markowich, Three dimensional simulation of Jet formation in collapsing Condensates, *J. Phys. B: At. Mol. Opt. Phys.*, **37**, 329-343 (2004).
- [19] W. Bao, Q. Du, and Y. Zhang, Dynamics of rotating Bose-Einstein condensates and their efficient and accurate numerical computation, *SIAM J. Appl. Math.*, **66**, 758-786 (2006).
- [20] W. Bao, P. A. Markowich, C. Schmeiser, and R. M. Weishaupl, On the Gross-Pitaevskii equation with strongly anisotropic confinement: formal asymptotics and numerical Experiments, *Math. Mod. Meth. Appl. Sci.*, **15**, 767-782, (2005).
- [21] R. A. Battye, N. R. Cooper, and P. M. Sutcliffe, Stable skyrmions in two-Component Bose-Einstein condensates, *Phys. Rev. Lett.*, **88**, 080401 (2002).
- [22] C. Besse, A relaxation scheme for the nonlinear Schrodinger equation, *SIAM J. Numer. Anal.*, **42**, 934-952 (2004).
- [23] C. C. Bradley, C. A. Sackett, and R. G. Hulet, Evidence of Bose-Einstein Condensation in an Atomic Gas with Attractive Interactions, *Phys. Rev. Lett.*, **75**, 1687 (1995).
- [24] E. N. Bulgakov and A. F. Sadreev, Vortex phase diagram of F=1 spinor Bose-Einstein condensates, *Phys. Rev. Lett.*, **90**, 200401 (2003).

-
- [25] Y. Castin and R. Dum, Bose-Einstein condensates with vortices in rotating traps, *Eur. Phys. J. D*, **7**, 399-412 (1999).
- [26] B. M. Caradoc-Davis, R. J. Ballagh, and P. B. Blakie, Three-dimensional vortex dynamics in Bose-Einstein condensates, *Phys. Rev. A*, **62**, 011602 (2000).
- [27] B. M. Caradoc-Davis, R. J. Ballagh, and P. B. Blakie, Coherent Dynamics of Vortex Formation in Trapped Bose-Einstein Condensates, *Phys. Rev. Lett.*, **83**, 895 (1999).
- [28] M. M. Cerimele, M.L. Chiofalo, F. Pistella, S. Succi, and M.P. Tosi, Numerical solution of the Gross-Pitaevskii equation using an explicit finite-difference scheme: An application to trapped Bose-Einstein condensates, *Phys. Rev. E*, **62**, 1382-1389 (2000).
- [29] M. M. Cerimele, F. Pistella and S. Succi, Particle-inspired scheme for the Gross-Pitaevskii equation: An application to Bose-Einstein condensation, *Comput. Phys. Comm.*, **129**, 82-90 (2000).
- [30] S. M. Chang, W. W. Lin, and S. F., Shieh, Gauss-Seidel-type methods for energy states of a multi-component Bose-Einstein condensate, *J. Comput. Physics*, **202**, 367-390 (2005).
- [31] M. Chang, Q. Qin, W. Zhang, L. You, and M. S. Chapman, Coherent spinor dynamics in a spin-1 Bose condensate, [cond-mat/0509341](https://arxiv.org/abs/cond-mat/0509341).
- [32] F. Chevy, K. W. Madison, V. Bretin and J. Dalibard, Formation of quantized vortices in a gaseous Bose-Einstein condensate, *Proceedings of Trapped particles and fundamental physics Workshop (Les Houches 2001)*. Editor : S. Atutov, K. Kalabrese, L. Moi.
- [33] M. L. Chiofalo, S. Succi and M.P. Tosi, Ground state of trapped interacting Bose-Einstein condensates by an explicit imaginary-time algorithm, *Phys. Rev. E*, **62**, 7438 (2000).

-
- [34] Y. Choi, J. Javanainen, I. Koltracht, M. Kotrun, P. J. McKenna, and N. Savytska, A fast algorithm for the solution of the time-independent Gross-Pitaevskii equation, *J. Comput. Phys.*, **190**, 1-23 (2003).
- [35] S. T. Chui, V. N. Ryzhov and E. E. Tareyeva, Vortex states in binary mixture of Bose-Einstein condensates, *cond-mat/0006348*.
- [36] P. G. Ciarlet and J. L. Lions, *Handbook of Numerical analysis, Volume I*, North-Holland, 203-461 (1990).
- [37] I. Coddington, P. C. Haljan, P. Engels, V. Schweikhard, S. Tung, and E. A. Cornell, Experimental studies of equilibrium vortex properties in a Bose-condensed gas, *Phys. Rev. A*, **70**, 063607 (2004).
- [38] M. Cozzini and S. Stringari, Macroscopic dynamics of a Bose-Einstein condensate containing a vortex lattice, *Phys. Rev. A*, **67**, 041602 (2003)
- [39] F. Dalfovo and S. Giorgini, Theory of Bose-Einstein condensation in trapped gases, *Rev. Mod. Phys.*, **71**, 463 (1999).
- [40] K. B. Davis, M. O. Mewes, M. R. Andrews, N. J. van Druten, D. S. Durfee, D. M. Kurn, and W. Ketterle, Bose-Einstein Condensation in a gas of Sodium atoms, *Phys. Rev. Lett.*, **75**, 3969 (1995).
- [41] R. J. Donnelly, *Quantized vortices in Helium II*, Cambridge University Press, Oxford, 1991.
- [42] K. Doi and Y. Natsume, Simulations of dynamics for wavepackets made by two-component Bose-Einstein condensates in Alkali-atom gases, *Physica B*, **329**, 49-50 (2003).
- [43] C. M. Dion and E. Cancès, Spectral method for the time-dependent Gross-Pitaevskii equation with a harmonic trap, *Phys. Rev. E*, **67**, 046706 (2003)

-
- [44] P. Engels, I. Coddington, P. C. Haljan, and E. A. Cornell, Nonequilibrium effects of anisotropic compression applied to vortex lattices in Bose-Einstein condensates, *Phys. Rev. Lett.*, **89**, 100403 (2002).
- [45] P. Engels, I. Coddington, V. Schweikhard and E. A. Cornell, Observation of Long-Lived Vortex Aggregates in Rapidly Rotating Bose-Einstein Condensates, *Phys. Rev. Lett.*, **90**, 170405 (2003)
- [46] J. R. Ensher, D. S. Jin, M. R. Matthews, C. E. Wieman, and E. A. Cornell, Bose-Einstein Condensation in a Dilute Gas: Measurement of Energy and Ground-State Occupation, *Phys. Rev. Lett.*, **77**, 4984 (1996).
- [47] B. D. Esry and C. H. Greene, Spontaneous spatial symmetry breaking in two-component Bose-Einstein condensates, *Phys. Rev. A*, **59**, 1457-1460 (1999).
- [48] D. L. Feder, C. W. Clark, and B. I. Schneider, Nucleation of vortex arrays in rotating anisotropic Bose-Einstein condensates, *Phys. Rev. A*, **61**, 011601 (1999).
- [49] D. L. Feder, C. W. Clark and B. I. Schneider, Vortex stability of interacting Bose-Einstein condensates confined in anisotropic harmonic traps, *Phys. Rev. Lett.*, **82**, 4956 (1999).
- [50] A. L. Fetter and A. A. Svidzinsky, Vortices in a trapped dilute Bose-Einstein condensate, *J. Phys. Condens. Matter*, **13**, R135-194 (2001).
- [51] A. L. Fetter, B. Jackson, and S. Stringari, Rapid rotation of a Bose-Einstein condensate in a harmonic plus quartic trap, cond-mat/0407119.
- [52] A. L. Fetter, Bose-Einstein condensates in dilute trapped atomic gases, *J. Low Temp. Phys.*, **129**, 263-321 (2002).
- [53] G. Fairweather and M. Khebchareon, Numerical methods for Schrodinger-type problems, in: A.H. Siddiqi and M. Kořvara (editors.), *Trends in industrial*

- and applied mathematics, Kluwer Academic Publishers, Netherlands, 2002, pp. 219-250.
- [54] J. J. García-Ripoll and V. M. Pérez-García, Nucleation of bended vortices in Bose-Einstein condensates in elongated traps, cond-mat/0006368.
- [55] J. J. García-Ripoll and V. M. Pérez-García, Stability of vortices in inhomogeneous Bose Einstein condensates subject to rotation: A three dimensional analysis, Phys. Rev. A, **60**, 4864-4874(1999).
- [56] J. J. García-Ripoll and V. M. Pérez-García, Optimizing schrodinger functionals using sobolev gradients: application to quantum mechanics and nonlinear optics, SIAM J. Sci. Comput., **23**, 1316-1334 (2001).
- [57] J. J. García-Ripoll and V. M. Pérez-García, Vortex nucleation and hysteresis phenomena in rotating Bose-Einstein condensate, Phys. Rev. A, **63**, 041603 (2001).
- [58] J. J. García-Ripoll and V. M. Pérez-García, Stable and unstable vortices in multicomponent Bose-Einstein Condensates, Phys. Rev. Lett., **81**, 4264 (2000).
- [59] J. J. García-Ripoll and V. M. Pérez-García, Split vortices in optically coupled Bose-Einstein condensates, Phys. Rev. A, **66**, 021602 (2002).
- [60] E. V. Goldstein and P. Meystre, Phase conjugation of multicomponent Bose-Einstein condensates, Phys. Rev. A, **59**, 1509 (1999).
- [61] A. Görlitz, T. L. Gustavson, A. E. Leanhardt, E. Löw, A. P. Chikkatur, S. Gupta, S. Inouye, D. E. Pritchard, and W. Ketterle, Sodium Bose-Einstein condensates in the F=2 state in a large-volume optical trap, Phys. Rev. Lett., **90**, 090401 (2003).
- [62] A. Griffin, D. Snoke, and S. Stringaro (Eds.), Bose-Einstein condensation, Cambridge University Press, New York, 1995.

-
- [63] D. S. Hall, M. R. Matthews, J. R. Ensher, C. E. Wieman, and E. A. Cornell, Dynamics of component separation in a binary mixture of Bose-Einstein condensates, *Phys. Rev. Lett.*, **81**, 1539-1542 (1998).
- [64] T. L. Ho and V. B. Shenoy, Binary mixtures of Bose Condensates of Alkali atoms, *Phys. Rev. Lett.*, **77**, 3276 (1996).
- [65] T. L. Ho, Spinor Bose Condensates in Optical Traps, *Phys. Rev. Lett.*, **81**, 742 (1998).
- [66] W. J. Huang and S. C. Gou, Ground state energy of the F=1 spinor Bose-Einstein condensates, *Phys. Rev. A*, **59**, 4908 (1999).
- [67] J. Ieda, T. Miyakawa, and M. Wadati, Exact Analysis of Soliton Dynamics in Spinor Bose-Einstein Condensates, *Phys. Rev. Lett.*, **93**, 194102 (2004).
- [68] T. Isoshima, K. Machida, and T. Ohmi, Spin-domain formation in spinor Bose-Einstein condensation, *Phys. Rev. A*, **60**, 4857 (1999).
- [69] T. Isoshima, M. Nakahara, T. Ohmi, and K. Machida, Creation of a persistent current and vortex in a Bose-Einstein condensate of alkali-metal atoms, *Phys. Rev. A*, **61**, 063610 (2000).
- [70] B. Jackson, J. F. McCann, and C. S. Adams, Vortex formation in dilute inhomogeneous Bose-Einstein Condensates, *Phys. Rev. Lett.*, **80**, 3903 (1998).
- [71] B. Jackson, J. F. McCann, and C. S. Adams, Vortex line and ring dynamics in trapped Bose-Einstein condensates, *Phys. Rev. A*, **61**, 013604 (1999).
- [72] B. Jackson and E. Zaremba, Finite-temperature simulations of the scissors mode in Bose-Einstein condensed gases, *Phys. Rev. Lett.*, **87**, 100404 (2001).
- [73] K. Kasamatsu and M. Tsubota, Nonlinear dynamics for vortex formation in a rotating Bose-Einstein condensate, *Phys. Rev. A*, **67**, 033610 (2003).

-
- [74] K. Kasamatsu, M. Tsubota and M. Ueda, Vortex phase diagram in rotating two-component Bose-Einstein condensates, *Phys. Rev. Lett.*, **91**, 150406 (2003).
- [75] K. Kasamatsu, M. Tsubota, and M. Ueda, Vortex states of two-component Bose-Einstein condensates with and without internal Josephson coupling, *J. Low Temper. Phys.*, **124**, 719 (2004).
- [76] K. Kasamatsu, M. Tsubota, and M. Ueda, Structure of vortex lattices in rotating two-component Bose-Einstein condensates, *Physica B*, 329-333 (2003).
- [77] K. Kasamatsu, M. Tsubota, and M. Ueda, Vortices in multicomponent Bose-Einstein condensates, *Int. J. Mod. Phys. B*, **19**, 1835 (2005).
- [78] K. Kasamatsu, M. Tsubota, and M. Ueda, Vortex molecules in coherently coupled two-component Bose-Einstein condensates, *Phys. Rev. Lett.*, **93**, 250406 (2004).
- [79] T. Kita, T. Mizushima, and K. Machida, Spinor Bose-Einstein Condensates with Many Vortices, *Phys. Rev. A*, **66**, 061601 (2002).
- [80] M. C. Lai and C. Y. Huang, a simple Dufort-Frankel type scheme for the Gross-Pitaevskii equation of Bose-Einstein condensates on different geometries, *Numer. Methods for PDEs*, **20**, 624-638 (2004).
- [81] L. Landau and E. Lifschitz, *Quantum Mechanics: non-relativistic theory*, Pergamon Press, New York, 1977.
- [82] A.E. Leanhardt, Y. Shin, D. Kielpinski, D.E. Pritchard and W. Ketterle, Coreless vortex formation in a spinor Bose-Einstein condensate, *Phys. Rev. Lett.*, **90**, 140403 (2003).
- [83] E. H. Lieb, R. Seiringer and J. Yngvason, Bosons in a Trap: A Rigorous Derivation of the Gross-Pitaevskii Energy Functional, *Phys. Rev. A*, **61**, 3602 (2000).

-
- [84] C. Y. Lin, E. J. V. de Passos, and D. S. Lee, Time-dependent variational analysis of Josephson oscillations in a two-component Bose-Einstein condensate, *Phys. Rev. A*, **62**, 055603 (2000).
- [85] C. Lobo, A. Sinatra, and Y. Castin, Vortex lattice formation in Bose-Einstein condensates, *Phys. Rev. Lett.*, **92**, 020403 (2004).
- [86] E. Lundh, C.J. Pethick, and H. Smith, Vortices in Bose-Einstein-condensated atomic clouds, *Phys. Rev. A*, **58**, 4816-4823 (1998).
- [87] K. W. Madison, F. Chevy, W. Wohlleben, and J. Dalibard, Vortex formation in a stirred Bose-Einstein Condensate, *Phys. Rev. Lett.*, **84**, 806 (2000).
- [88] K. W. Madison, F. Chevy, W. Wohlleben and J. Dalibard, *J. Mod. Opt.*, **47**, 2725 (2000).
- [89] J. P. Martikainen, Dynamics and excitations of Bose-Einstein condensates, Academic dissertation, University of Helsinki, 2001.
- [90] J. P. Martikainen, A. Collin, and K.-A. Suominen, Coreless vortex ground state of the rotating spinor condensate, *Phys. Rev. A*, **66**, 053604 (2002).
- [91] M. R. Matthews, B. P. Anderson, P. C. Haljan, D. S. Hall, C. E. Wieman, and E. A. Cornell, Vortices in a Bose-Einstein Condensate, *Phys. Rev. Lett.*, **83**, 2498 (1999).
- [92] H. J. Miesner, D. M. Stamper-Kurn, J. Stenger, S. Inouye, A. P. Chikkatur, and W. Ketterle, Observation of metastable states in spinor Bose-Einstein condensates, *Phys. Rev. Lett.*, **82**, 2228 (1999).
- [93] A. Minguzzi, S. Succi, F. Toschi, M. P. Tosi, P. Vignolo, Numerical methods for atomic quantum gases with applications to Bose-Einstein condensates and to ultracold fermions, *Phys. Rep.*, **395**, 223-355 (2004).

-
- [94] T. Mizushima, N. Kobayashi and K. Machida, Coreless and singular vortex lattices in rotating spinor Bose-Einstein condensates, *Phys. Rev. A*, **70**, 043613 (2004).
- [95] T. Mizushima, K. Machida, and T. Kita, Axisymmetric versus nonaxisymmetric vortices in spinor Bose Einstein condensates, *Phys. Rev. A*, **66**, 053610 (2002)
- [96] M. Modugno, L. Pricoupenko, and Y. Castin, Bose-Einstein condensates with a bent vortex in rotating traps, *Eur. Phys. J. D*, **22**, 235-257 (2003).
- [97] M. Modugno, F. Dalfovo, C. Fort, P. Maddaloni, and F. Minardi, Dynamics of two colliding Bose-Einstein condensates in an elongated magnetostatic trap, *Phy. Rev. A*, **62**, 063607 (2000).
- [98] E. J. Mueller and T.-L. Ho, Two-component Bose-Einstein condensates with a large number of vortices, *Phys. Rev. Lett.*, **88**, 180403 (2002).
- [99] J. Mur-Petit, M. Guilleumas, A. Polls, A. Sanpera, M. Lewenstein, K. Bongs, and K. Sengstock, Dynamics of $F = 1$ spinor condensates at finite temperatures, *cond-mat/0507521*.
- [100] P. Muruganandam and S. K. Adhikari, Bose-Einstein condensation dynamics in three dimensions by pseudospectral and finite-difference methods, *J. Phys. B: At. Mol. Opt. Phys.*, **36**, 2501-2513 (2003).
- [101] T. Ohmi and K. Machida, Bose-Einstein Condensation with Internal Degrees of Freedom in Alkali Atom Gases, *J. Phys. Soc. Jpn.*, **67**, 1822 (1998).
- [102] V. M. Pérez-García and X. Y. Liu, Numerical methods for the simulation of trapped nonlinear Schrödinger systems, *Appl. Math. Comput.*, **144** 215-235 (2003).

-
- [103] V. M. Pérez-García and J. J. García-Ripoll, Two-mode theory of vortex stability in multicomponent Bose-Einstein condensates, *Phys. Rev. A*, **62**, 033601 (2000).
- [104] L. Pitaevskii and S. Stringari, *Bose-Einstein condensation*, Clarendon Press, New York, 2003.
- [105] H. Pu and N.P. Bigelow, Properties of two-species Bose Condensates, *Phys. Rev. Lett.*, **80**, 1130 (1998).
- [106] H. Pu, C. K. Law, S. Raghavan, J. H. Eberly, and N. P. Bigelow, Spin-mixing dynamics of a spinor Bose-Einstein condensate, *Phys. Rev. A*, **60**, 1463 (1999).
- [107] H. Pu, S. Raghavan and N. P. Bigelow, Creation of topological states in spinor condensates, *Phys. Rev. A*, **63**, 063603 (2001).
- [108] C. Raman, J. R. Abo-Shaeer, J. M. Vogels, K. Xu and W. Ketterle, Vortex nucleation in a stirred Bose-Einstein Condensate, *Phys. Rev. Lett.*, **87**, 210402 (2001).
- [109] J. W. Reijnders, F. J. M. Van Lankvelt, and K. Schoutens, Rotating spin-1 bosons in the lowest Landau level, *Phys. Rev. A*, **69**, 023612 (2004).
- [110] F. Riboli and M. Modugno, Topology of the ground state of two interacting Bose-Einstein condensates, *Phys. Rev. A*, **65**, 063614 (2002).
- [111] G. L. Salmond, C. A. Holmes, and G. J. Milburn, Dynamics of a strongly driven two-component Bose-Einstein condensate, *Phys. Rev. A*, **65**, 033623, (2002).
- [112] L. Santos and T. Pfau, Spin 3 Chromium Bose Einstein Condensates, [arXiv:cond-mat/0510634](https://arxiv.org/abs/cond-mat/0510634).
- [113] C. M. Savage and J. Ruostekoski, Dirac monopoles and dipoles in ferromagnetic spinor Bose-Einstein condensates, *Phys. Rev. A*, **68**, 043604 (2003)

-
- [114] H. Schmaljohann, M. Erhard, J. Kronjager, K. Sengstock, and K. Bongs, Dynamics and thermodynamics in spinor quantum gases, cond-mat/0406485.
- [115] H. Schmaljohann, M. Erhard, J. Kronjager, M. Kottke, S. van Staa, L. Cacciapuoti, J. J. Arlt, K. Bongs, and K. Sengstock, Dynamics of F=2 Spinor Bose-Einstein Condensates, Phys. Rev. Lett., **92**, 040402 (2004).
- [116] B. I. Schneider and D.L. Feder, Numerical approach to the ground and excited states of a Bose-Einstein condensated gas confined in a completely anisotropic trap, Phys. Rev. A, **59**, 2232 (1999).
- [117] V. Schweikhard, I. Coddington, P. Engels, S. Tung, and E. A. Cornell, Vortex-lattice dynamics in rotating spinor Bose-Einstein condensates, Phys. Rev. Lett. **93**, 210403 (2004).
- [118] R. Seiringer, Gross-Pitaevskii theory of the rotating Bose gas, Commun. Math. Phys., **229**, 491-509 (2002).
- [119] R. Seiringer, Ground state asymptotics of a dilute rotating Gas, J. Phys. A: Math. Gen., **36**, 9755-9778 (2003).
- [120] V. S. Shchesnovich and S. B. Cavalcanti, Rayleigh functional for nonlinear systems, arxiv:nlin.PS/0411033.
- [121] L. Simon, Asymptotics for a class of nonlinear evolution equations with applications to geometric problems, Anna. of Math., **118**, 525-571 (1983).
- [122] T. P. Simula, A. A. Penckwitt, and R. J. Ballagh, Giant vortex lattice deformation in rapidly rotating Bose-Einstein condensates, Phys. Rev. Lett., **92**, 060401 (2004).
- [123] S. Sinha and Y. Castin, Dynamic instability of a rotating Bose-Einstein condensate, Phys. Rev. Lett., **87**, 190402 (2001).

-
- [124] A. Sinatra, P. O. Fedichev, Y. Castin, J. Dalibard, and G. V. Shlyapnikov, Dynamics of two interacting Bose-Einstein condensates, *Phys. Rev. Lett.*, **82**, 251 (1999).
- [125] J. Stenger, S. Inouye, D. M. Stamper-Kurn, H. J. Miesner, A. P. Chikkatur, and W. Ketterle, Spin domains in ground-state Bose-Einstein condensates, *Nature (London)*, **396**, 345 (1998).
- [126] G. Strang, On the construction and comparison of difference schemes, *SIAM J. Numer. Anal.*, **5**, 505-517 (1968).
- [127] A. A. Svidzinsky and A. L. Fetter, Dynamics of a vortex in a trapped Bose-Einstein condensate, *Phys. Rev. A*, **62**, 063617 (2000).
- [128] Y. Tian and M. Qin, Explicit symplectic schemes for investigating the evolution of vortices in a rotating Bose-Einstein Condensate, *Comput. Phys. Comm.*, **155**, 132-143 (2003).
- [129] M. Trippenbach, K. Góral, K. Rzażewski, B. Malomed, and Y. B. Band, Structure of binary Bose-Einstein condensates, *J. Phys. B: At. Mol. Opt. Phys.*, **33** 4017-4031 (2000).
- [130] M. Tsubota, K. Kasamatsu, and M. Ueda, Vortex lattice formation in a rotating Bose-Einstein condensate, *Phys. Rev. A*, **65**, 023608 (2002).
- [131] V. Vekslerchik and V. M. Pérez-García, Exact solution of the two-mode model of multicomponent Bose-Einstein condensates, *DCDS-B*, **3**, 179-192 (2003).
- [132] H. Wang, Numerical studies on the split-step finite difference method for nonlinear Schrödinger equations, *Appl. Math. Comput.*, **170**, 17-35 (2005).
- [133] H. Wang, A time-splitting spectral method for coupled Gross-Pitaevskii equations with applications to the dynamics of rotating two-component Bose-Einstein condensates, preprint.

-
- [134] J. E. Williams and M. J. Holland, Preparing topological states of a Bose-Einstein condensate, *Nature*, **401**, 568-571 (1999).
- [135] J. E. Williams, The preparation of topological modes in a strongly-coupled two-component Bose-Einstein Condensate, Ph.D thesis, University of Colorado, 1999.
- [136] S. Yi, O. E. M ustecapholu, C. P. Sun and L. You, Single-mode approximation in a spinor-1 atomic condensate, *Phys. Rev. A*, **66**, 011601(R) (2002).
- [137] W. Zhang, S. Yi and L. You, Mean field ground state of a spin-1 condensate in a magnetic field, *New J. Phys.*, **5**, 77-89 (2003).
- [138] W. Zhang and L. You, An effective quasi-one-dimensional description of a spin-1 atomic condensate, *Phys. Rev. A*, **71**, 025603 (2005).
- [139] P. Zhang, C. K. Chan, X. G. Li, Q. K. Xue and X. G. Zhao, Dynamics of the spin-2 Bose condensate driven by external magnetic fields, *Phys. Rev. A*, **66**, 043606 (2002)
- [140] Y. Zhang and W. Bao, Analytical solutions for the center of mass and a leap-frog pseudospectral approximation for dynamics in rotating Bose-Einstein condensates, preprint.
- [141] A. H. Zhou, An analysis of finite-dimensional approximations for the ground state solution of Bose-Einstein condensates, *Nonlinearity*, **17**, 541-550 (2004).

Publications

[1] W. Bao, H. Wang and P. A. Markowich, Ground, symmetric and central vortex states in rotating Bose-Einstein condensates, *Communications in Mathematical Science*, Vol. 3, No. 1, pp. 57-88, (2005).

[2] H. Wang, Numerical studies on the split-step finite difference method for nonlinear Schrodinger equations, *Applied Mathematics and Computation*, Vol. 170, No 1, pp. 17-35 (2005).

[3] W. Bao and H. Wang, An efficient and spectrally accurate numerical method for computing dynamics of rotating Bose-Einstein condensates, *Journal of Computational Physics*, to appear.

[4] H. Wang, A time-splitting spectral method for coupled Gross-Pitaevskii equations with applications to the dynamics of rotating two-component Bose-Einstein condensates, *Journal of Computational and Applied Mathematics*, to appear.

[5] H. Wang, Ground, symmetric and central vortex states in rotating vortex states in rotating two-component Bose-Einstein condensates, submitted.

[6] H. Wang, A time-splitting spectral method for computing the dynamics of spinor $F=1$ Bose-Einstein condensates, submitted.

Name: Hanquan Wang
Degree: Doctor of Philosophy
Department: Mathematics
Thesis Title: Quantized vortex states and dynamics
in Bose-Einstein condensates

Abstract

In this thesis, we analytically and numerically study quantized vortex states as well as their dynamics in rotating Bose-Einstein condensate at extremely low temperature.

We present an efficient method–gradient flow with discrete normalization to find the stationary solutions of the Gross-Pitaevskii equation and coupled Gross-Pitaevskii equations. We give a mathematical justification for the correctness of the method. Based on these solutions, we obtain the equilibrium properties such as quantized vortex states of trapped Bose-Einstein condensated gases under rotation at extremely low temperature.

We also present a new, efficient and spectrally accurate method–time-splitting spectral method—to numerically solve the Gross-Pitaevskii equation, coupled Gross-Pitaevskii equations and generalized Gross-Pitaevskii equations. Based on the time-dependent solutions of these equations, we numerically obtain the dynamics of quantized vortex states in rotating one-component Bose-Einstein condensate, two-component Bose-Einstein condensates and spinor Bose-Einstein condensates at extremely low temperature.

Keywords Bose-Einstein condensate, Gross-Pitaevskii equation, time-splitting spectral method, Gradient flow with discrete normalization.

**QUANTIZED VORTEX STATES
AND DYNAMICS IN
BOSE-EINSTEIN CONDENSATES**

HANQUAN WANG

NATIONAL UNIVERSITY OF SINGAPORE

2006

Quantized Vortex States and Dynamics in Bose-Einstein condensates Hanquan Wang 2006

Quantized Vortex States and Dynamics in Bose-Einstein condensates Hanquan Wang 2006